Technische Universität München
Fakultät für Medizin

Characterization of subtype-specific combinatorial treatment-induced adaptive immune responses and vascular remodeling in pancreatic ductal adenocarcinoma

Jeannine Sophie Heetmeyer

Vollständiger Abdruck der von der Fakultät für Medizin der Technischen Universität München zur Erlangung des akademischen Grades einer

Doktorin der Medizin (Dr. med.)

genehmigten Dissertation.

Vorsitz: apl. Prof. Dr. Stefan Thorban

Prüfer*innen der Dissertation:

1. Prof. Dr. Dieter Saur
2. apl. Prof. Dr. Achim Krüger

Die Dissertation wurde am 15.06.2022 bei der Technischen Universität München eingereicht und durch die Fakultät für Medizin am 16.05.2023 angenommen.

Parts of the work included in this thesis have been published in:

Falcomatà, C., Bärthel, S., Widholz, S. A., Schneeweis, C., Montero, J. J., Toska, A., Mir, J., Kaltenbacher, T., **Heetmeyer, J.**, Swietlik, J. J., Cheng J. Y., Teodorescu, B., Reichert, O., Schmitt, C., Grabichler, K., Coluccio, A., Boniolo, F., Veltkamp, C., Zukowska, M., Vargas, A. A., Paik, W. H., Jesinghaus, M., Steiger, K., Maresch, R., Öllinger, R., Ammon, T., Baranov, O., Robles, M. S., Rechenberger, J., Kuster, B., Meissner, F., Reichert, M., Flossdorf, M., Rad, R., Schmidt-Supprian, M., Schneider, G., Saur, D. (2022): Selective multi-kinase inhibition sensitizes mesenchymal pancreatic cancer to immune checkpoint blockade by remodeling the tumor microenvironment. Nature Cancer. Volume 3 Issue 3, March 2022, Pages 318–336. Epub 2022 Jan 31. https://doi.org/10.1038/s43018-021-00326-1.

Für Jonas

Table of contents

Abstract

Pancreatic ductal adenocarcinoma (PDAC) is the most common malignant neoplasm of the pancreas and one of the most aggressive human cancers. In contrast to the decline in overall cancer death rates, rising mortality rates have been observed in pancreatic cancer. Despite the development of new surgical techniques and intensification of chemotherapeutic regimens, prognosis of PDAC patients has improved only marginally in the past decades. In search of new therapeutic approaches, particular focus should be given to the generally immunosuppressive tumor microenvironment of PDAC, which is considered as one of the main reasons for the failure of immunotherapy in this cancer entity. Besides, PDAC is a highly heterogenous disease and can display a variety of molecular and morphological features. Genomic and transcriptomic profiling analyses and their correlation to histopathological characteristics have helped to identify distinct PDAC subtypes, two of which have been described most consistently across different studies. While the “classical” subtype is characterized by an epithelial-like gene expression pattern and gland-forming, differentiated tumor cells, “mesenchymal” PDAC present as non-gland forming, undifferentiated tumors with a quasi-mesenchymal gene expression profile, particularly poor prognosis, profound resistance to chemotherapy and high expression levels of mutant KRAS. Mutations in the *KRAS* gene are found in the majority of PDAC patients, leading to constitutive activation of the RAS-MEK-ERK signaling pathway, which is located downstream of receptor tyrosine kinases, and thereby to growth factor-independent proliferation of cells. This oncogenic cascade potentially represents a therapeutic target, but previous *in vitro* and *in vivo* studies in our group found the mesenchymal PDAC subtype to be highly resistant to the MEK inhibitor trametinib. However, a strong synergism was detected with the multikinase inhibitor nintedanib via high-throughput combination drug screening performed on human and murine PDAC cell lines. The combination of trametinib and nintedanib not only induced apoptosis of mesenchymal PDAC cells *in vitro*, but also led to a remarkable response *in vivo*, as evidenced by significantly reduced tumor volumes and improved survival particularly in mesenchymal PDAC-bearing mice.

In this study, adaptive immune responses and vascular remodeling induced by the combinatorial treatment with trametinib and nintedanib were characterized and compared to baseline lymphocytic infiltration and tumor vasculature morphology in genetically engineered and orthotopic transplantation mouse models of classical and mesenchymal PDAC. Multiplex immunofluorescence revealed an immunologically “cold” tumor microenvironment marked by a lack of cytotoxic T cells particularly in the mesenchymal subtype. Besides leading to an overall increase in lymphocytic infiltration, the combinatorial treatment was able to induce

subtype-specific adaptive immune responses, characterized by an improved recruitment of cytotoxic T cells into the tumor core and a relative reduction of immunosuppressive T cell subpopulations specifically in mesenchymal PDAC. In this subtype, features of vascular remodeling including architectural changes, vascular maturation and endothelial cell activation were observed upon combinatorial treatment, possibly facilitating intratumoral recruitment of anti-tumorigenic adaptive immune cell populations. Compared to the equivalent immunocompetent PDAC mouse model, T cell-deficient mesenchymal PDAC-bearing *CD3ε-KO* mice demonstrated higher tumor volumes and a shortened survival benefit, indicating a significant contribution of the observed T cell-mediated anti-tumor immunity to treatment efficacy *in vivo*. In conclusion, our findings suggest that a combination therapy consisting of trametinib and nintedanib immunologically “warms up” the tumor microenvironment of mesenchymal PDAC, thereby representing a promising therapeutic approach, especially in combination with immunotherapy, for this highly aggressive PDAC subtype.

Zusammenfassung

Das duktale Adenokarzinom des Pankreas (PDAC) ist die häufigste maligne Neoplasie der Bauchspeicheldrüse und gehört zu den aggressivsten beim Menschen vorkommenden Tumoren. Im Gegensatz zur rückläufigen allgemeinen Krebssterblichkeit wurden in den vergangenen Jahren steigende Mortalitätsraten bei PDAC verzeichnet und trotz Optimierung operativer Verfahren und Einführung intensivierter Chemotherapie-Regime hat sich die Prognose der betroffenen Patienten kaum verbessert. Auf der Suche nach neuen therapeutischen Ansätzen ist von großer Bedeutung, dass PDAC im Allgemeinen durch eine immunsuppressive Tumor-Mikroumgebung gekennzeichnet ist, welche einen möglichen Grund für das Versagen moderner Immuntherapien darstellt. Darüber hinaus ist PDAC kein einheitlicher Tumor, sondern weist eine bedeutende molekulare und morphologische Heterogenität auf. Anhand von genomischen und transkriptomischen Analysen sowie deren Korrelation mit histopathologischen Merkmalen konnten verschiedene Subtypen des PDAC identifiziert werden. Dabei wird insbesondere zwischen einem „klassischen“ Subtyp mit vorwiegend epithelialem Genexpressionsmuster und drüsenbildenden, differenzierten Tumorzellen sowie einem „quasi-mesenchymalen“ Subtyp mit einem Mesenchym-ähnlichen Expressionsprofil und atypisch angeordneten, undifferenzierten Tumorzellen unterschieden, wobei letzter mit einer besonders schlechten Prognose, einer ausgeprägten Chemotherapie-Resistenz und einem hohen Expressionslevel von mutiertem KRAS assoziiert ist. Mutationen im *KRAS*-Gen finden sich bei der Mehrzahl der PDAC-Patienten. Sie führen zu einer konstitutiven Aktivierung des an Rezeptor-Tyrosinkinasen angegliederten RAS-MEK-ERK-Signalwegs und somit einer wachstumsfaktorunabhängigen Proliferation der Zellen. In Vorarbeiten wurde daher die Effektivität des MEK-Inhibitors Trametinib *in vitro* und im Mausmodell untersucht, jedoch wies insbesondere das mesenchymale PDAC eine ausgeprägte Resistenz gegenüber dem Wirkstoff auf. Bei diesem Subtyp ergab ein an humanen und murinen PDAC-Zelllinien durchgeführtes Hochdurchsatzscreening dafür eine synergistische Wirkung von Trametinib mit dem Multikinase-Inhibitor Nintedanib. Die Kombination der beiden Wirkstoffe führte nicht nur zur Induktion von Apoptose in mesenchymalen Tumorzellen *in vitro*, sondern auch zu einem bemerkenswerten Ansprechen *in vivo*, mit reduzierten Tumorvolumina und einem signifikant längeren Überleben der behandelten Mäuse.

In dieser Arbeit wurden die durch die neuartige Kombinationstherapie induzierten adaptiven Immunantworten und vaskulären Veränderungen in Mausmodellen des klassischen und mesenchymalen PDAC-Subtyps untersucht und mit der Baseline-Lymphozyteninfiltration und -Tumorvaskularisation verglichen. Mittels Multiplex-Immunfluoreszenz konnte gezeigt werden,

dass insbesondere das mesenchymale PDAC durch eine immunologisch „kalte“ Tumor-Mikroumgebung mit sehr geringem Vorkommen cytotoxischer T-Zellen charakterisiert ist. Unter Kombinationstherapie mit Trametinib und Nintedanib konnten neben einer insgesamt verstärkten Lymphozyteninfiltration Subtyp-spezifische adaptive Immunantworten nachgewiesen werden, wobei nur beim mesenchymalen PDAC eine verbesserte Rekrutierung cytotoxischer T-Zellen ins Tumorinnere und ein relativer Rückgang immunsuppressiver T-Zell-Subpopulationen beobachtet wurden. Zudem kam es in Tumoren des mesenchymalen Subtyps durch die Kombinationstherapie zu einem vaskulären Remodeling mit Veränderungen der Gefäßarchitektur, Gefäßreifung und Endothelzellaktivierung, wodurch die intratumorale Rekrutierung antitumorigen wirksamer Immunzellpopulationen begünstigt werden könnte. Anhand T-Zell-defizienter *CD3ε-KO* Mäuse konnte bestätigt werden, dass die beobachtete T-Zell-vermittelte Immunantwort beim mesenchymalen PDAC von entscheidender Bedeutung für das Therapieansprechen *in vivo* ist, da der durch die Kombinationsbehandlung erzielte Überlebensvorteil mit Rückgang des Tumorwachstums im Vergleich zum immunkompetenten Mausmodell signifikant geringer war. Die Ergebnisse dieser Arbeit zeigen, dass eine aus Trametinib und Nintedanib bestehende Kombinationstherapie zu grundlegenden Veränderungen der Tumor-Mikroumgebung speziell des mesenchymalen PDAC im Sinne eines immunologischen „Aufwärmens“ führt und somit allein oder auch in Kombination mit einer zusätzlichen Immuntherapie eine vielversprechende therapeutische Option bei diesem besonders aggressiven PDAC-Subtyp darstellt.

List of figures

List of tables

List of abbreviations

°C	degree Celsius
ADEX	aberrantly differentiated endocrine exocrine
AFN	atipamezole, flumazenil, naloxone
BSA	bovine serum albumin
CAF	cancer-associated fibroblast
CAM	cell adhesion molecule
CD	cluster of differentiation
CK	cytokeratin
COSMIC	Catalogue of Somatic Mutations In Cancer
CTLA-4	cytotoxic T-lymphocyte-associated protein 4
CXCL	chemokine (C-X-C motif) ligand
DAPI	4′,6-diamidino-2-phenylindole
DMEM	Dulbecco's modified eagle medium
DMSO	dimethyl sulfoxide
DNA	deoxyribonucleic acid
ECG	electrocardiogram
ECM	extracellular matrix
EDTA	ethylenediaminetetraacetic acid
EGF(R)	epidermal growth factor (receptor)
EMA	European Medicines Agency
ERK	extracellular signal-regulated kinases
FBS	fetal bovine serum
FDA	U.S. Food and Drug Administration
FGF(R)	fibroblast growth factor (receptor)
FOLFIRINOX	folinic acid, fluorouracil, irinotecan, oxaliplatin
FOXP3	forkhead box protein P3
GAP	GTPase-activating protein

GDP	guanosine diphosphate
GEF	guanine nucleotide exchange factor
GEMM	genetically engineered mouse model
GTP	guanosine triphosphate
H&E	hematoxylin and eosin
hPDAC	human pancreatic ductal adenocarcinoma
IACUC	Institutional Animal Care and Use Committee
IFN-γ	interferon gamma
IL	interleukin
KO	knockout
KRAS	Kirsten rat sarcoma virus
LSL	lox-Stop-lox
MEK	mitogen-activated protein kinase kinase
MMF	midazolam, medetomidine and fentanyl
mPDAC	murine pancreatic ductal adenocarcinoma
MRI	magnetic resonance imaging
NK	natural killer
NSCLC	non-small cell lung cancer
PanIN	pancreatic intraepithelial neoplasia
PBS	phosphate buffered saline
PD-1	programmed cell death 1
PDAC	pancreatic ductal adenocarcinoma
PDGF(R)	platelet-derived growth factor
Pdx1	pancreatic and duodenal homeobox 1
PFA	paraformaldehyde
PI3K	phosphatidylinositol 3-kinase
PPT	primary pancreatic tumor
Ptf1a	pancreas transcription factor 1 subunit alpha

RAF	rapidly accelerated fibrosarcoma
RAS	rat sarcoma virus
RNA	ribonucleic acid
ROI	region of interest
RRID	Research Resource Identifier
RT	room temperature
RTK	receptor tyrosine kinase
S1PR1	sphingosine 1-phosphate receptor-1
SD	standard deviation
SEER	Surveillance, Epidemiology, and End Results
SOS	son of sevenless
T/N	trametinib + nintedanib
TGF-β	transforming growth factor
Th1	type 1 helper T cell
Th2	type 2 helper T cell
TIGIT	T cell immunoreceptor with Ig and ITIM domains
TIL	tumor infiltrating lymphocytes
TLS	tertiary lymphoid structure
TME	tumor microenvironment
TNF-α	tumor necrosis factor alpha
TP53/Trp53	transformation related protein 53
UV	ultraviolet
VEGF(R)	vascular endothelial growth factor (receptor)
WT	wild type
α-SMA	alpha-smooth muscle actin

Abbreviations and units according to the International System of Units (SI) are not included.

1 Introduction

1.1 Pancreatic ductal adenocarcinoma (PDAC)

Pancreatic ductal adenocarcinoma (PDAC) arises in exocrine pancreatic glands and constitutes the most common malignant pancreatic neoplasm, accounting for more than 90% of all pancreatic cancers (Kleeff et al., 2016). With 62,210 newly diagnosed cases and 49,830 deaths in the United States as estimated for 2022 by the American Cancer Society, pancreatic cancer represents a great burden on patients and healthcare systems (Siegel et al., 2022). The five-year relative survival rate for all stages combined is 11%, having improved slowly from the 6% reported in 2012 (Siegel et al., 2012; 2022). However, while earlier diagnosis and improved treatment options have caused overall cancer death rates to decline since 1991, rising mortality rates have been observed in pancreatic cancer, thereby becoming the third most frequent cause of cancer-related death in countries of the Global North (Siegel et al., 2022; Ferlay et al., 2016). In Germany, about 50% of patients are diagnosed in a metastatic stage of disease with a five-year relative survival of only 2% (Robert Koch-Institut, 2021) and pancreatic cancer is projected to surpass colorectal cancer regarding cancer-related deaths by 2030 (Quante et al., 2016).

While the majority of PDAC is sporadic, 3% of all cases arise in patients with hereditary cancer syndromes in which a causative germline mutation can be identified (Llach et al., 2020). Another 7% of cases are considered familial, with two or more affected first-degree relatives, but no association to a specific gene (Llach et al., 2020). Even for individuals with only one affected first-degree relative, an 80% increased risk of developing PDAC has been found (Permuth-Wey & Egan, 2009). Besides genetic susceptibility and age, a number of modifiable risk factors have been associated with the development of pancreatic cancer, with cigarette smoking considered to be the most important one (Bosetti et al., 2012; Lynch et al., 2009). Excessive alcohol consumption (Wang et al., 2016; Tramacere et al., 2010), chronic pancreatitis (Raimondi et al., 2010), obesity and insulin resistance (Calle et al., 2003; Rahn et al., 2018; Huxley et al., 2005) are additional risk factors implicated in pathoetiology of the disease.

One of the main challenges in diagnosis of pancreatic cancer is the long asymptomatic disease progression before the onset of mostly unspecific symptoms such as weight loss and abdominal pain (De La Cruz et al., 2014). Furthermore, biomarkers with sufficient positive predictive value are not available and common imaging modalities fail to reliably detect tumors at early disease stages (Kleeff et al., 2016). Consequently, regional or distant metastases are present at diagnosis in 82% of cases (SEER Stat Fact Sheets: Pancreatic Cancer, 2021), contributing to the high mortality rates.

To date, surgical resection remains the only potential cure, but only 10 – 20% of patients present with resectable tumors (Mizrahi et al., 2020; Kleeff et al., 2016). In combination with adjuvant chemotherapy, five-year survival rates only improve to around 20% in patients with total macroscopic resection of the tumor (Neoptolemos et al., 2004; Oettle et al., 2013). Similar outcomes have been shown for secondary resections after neoadjuvant radiochemotherapy in patients with primarily irresectable tumors (Roeder, 2016). In PDAC patients with disseminated disease, systemic chemotherapy with gemcitabine alone constituted the standard therapy for nearly two decades, despite minimal therapeutic effect (Manji et al., 2017; Burris et al., 1997). Both gemcitabine plus nab-paclitaxel and the polychemotherapeutic FOLFIRINOX regimen have shown to improve prognosis, with however poor median survival times of 8.5 and 11.1 months, respectively, and significant associated toxicity of FOLFIRINOX in particular (Conroy et al., 2011; Von Hoff et al., 2013). In urgent need of improved treatment strategies, a comprehensive investigation of PDAC based on appropriate models recapitulating molecular and biological characteristics of the disease is required.

1.2 Molecular PDAC subtypes

PDAC is a highly heterogenous disease, displaying a wide spectrum of molecular and morphological features with potential therapeutic implication (Orth et al., 2019). Large scale genomic analyses including whole-genome sequencing have revealed the complexity of the mutational landscape and evolutionary routes in PDAC (Cancer Genome Atlas Research Network, 2017; Notta et al., 2016; Witkiewicz et al., 2015; Biankin et al., 2012; Jones et al., 2008).

Genomic and transcriptomic profiling studies have identified distinct subtypes of PDAC reflecting both tumor cell- and stroma-specific features (Bailey et al., 2016b; Moffitt et al., 2015; Collisson et al., 2011). Considerable overlap exists for two main subtypes, including a “classical” subtype characterized by an epithelial-like gene expression pattern and a “basal-like”, quasi-mesenchymal subtype with a particularly poor prognosis and profound resistance to chemotherapy (Aung et al., 2018; Moffitt et al., 2015; Chan-Seng-Yue et al., 2020; Dijk et al., 2020). Additionally, an aberrantly differentiated endocrine exocrine (ADEX) subtype with upregulated transcriptional networks related to exocrine and endocrine differentiation, as well as an immunogenic subtype enriched in different immune cell subpopulations characterized by enhancement of immune evasion pathways have been described (Bailey et al., 2016b). Recently, histopathological characteristics were shown to correlate with the expression profile-based classification, with enrichment of classical gene expression signatures in gland-forming, differentiated tumors and quasi-mesenchymal features in non-gland forming, undifferentiated tumors (Kalimuthu et al., 2020). Clinical application of expression signature-based subtyping

of PDAC patients is subject to ongoing clinical trials (Schreyer et al., 2021), thus representing a first step towards implementation of personalized treatment strategies by exploiting individual therapeutic vulnerabilities.

Another approach to PDAC classification based on metabolic profiling revealed existence of three distinct metabolic subtypes, of which the lipogenic and glycolytic subtypes were associated with classical and quasi-mesenchymal gene expression signatures, respectively (Daemen et al., 2015). In contrast, tyrosine phosphorylation profiles identified via immunoaffinity-coupled high-resolution mass spectrometry did not correspond to expression-defined subtypes but provided a complementary subclassification of PDAC with potential therapeutic benefit by identifying a receptor tyrosine kinase-enriched subtype with increased sensitivity to the EGFR inhibitor erlotinib (Humphrey et al., 2016).

In the subtyping approaches described above, genomic and transcriptomic analyses were mostly performed on tissue samples from surgically resectable tumors, representing only a minority of PDAC patients (Rawla et al., 2019). The lack of samples from advanced and metastatic tumors causes underrepresentation of particularly aggressive subtypes including undifferentiated PDAC (Iacobuzio-Donahue et al., 2009; Morohoshi et al., 1983). Additionally, the high stromal content impedes identification of tumor cell-specific expression signatures. To overcome these limitations, primary cell lines derived from metastatic murine PDAC have been characterized via integrative genomic, transcriptomic and phenotypical analyses, revealing correlation of epithelial and mesenchymal gene expression signatures with cellular morphology and histopathological differentiation, consistent with previously described expression signature-based PDAC subtypes (Mueller et al., 2018).

1.3 The tumor microenvironment (TME) of PDAC

PDAC harbors a complex tumor microenvironment (TME) comprising a diversity of non-neoplastic cell populations including cancer-associated fibroblasts (CAFs), immune cells and endothelial cells as well as acellular components such as the extracellular matrix (ECM), cytokines and growth factors (Hosein et al., 2020; Biankin & Maitra, 2015; Moffitt et al., 2015). The extensive desmoplastic stroma constituting up to 80% of the tumor mass is considered to derive from proliferation of CAFs and concomitant remodeling of the ECM (Neesse et al., 2019; Dougan, 2017). While this desmoplastic reaction is primarily thought to contribute to the biological aggressiveness of PDAC (Ho et al., 2020; Carvalho et al., 2021), other studies also suggest a tumor-restraining function of stromal components (Rhim et al., 2014; Özdemir et al., 2014).

On the other hand, the immune microenvironment in PDAC is typically characterized by the predominance of immunosuppressive cells such as myeloid-derived suppressor cells, M2-polarized tumor associated macrophages and regulatory T cells which create a biological niche fostering tumor growth (Vonderheide & Bayne, 2013; Zhao et al., 2009; Di Caro et al., 2016; Hu et al., 2016). Upon stratification of PDAC patients based on TME-related gene expression signatures, upregulation of genes related to macrophages and CAFs in the “activated” stroma subtype was found to be associated with a particularly poor prognosis (Moffitt et al., 2015). However, effective T cell-mediated anti-tumor immune responses correlating with increased survival have also been observed in some PDAC patients (Carstens et al., 2017; Ino et al., 2013; Fukunaga et al., 2004).

Little is known about the intratumoral crosstalk between immune cells and other components of the TME in PDAC such as the tumor vasculature (Ho et al., 2020; Liu et al., 2019; Schneider et al., 2017). Further characterization of intra- and intertumoral stromal heterogeneity within different molecular subtypes of PDAC is thus required to gain a deeper understanding which could be exploited to generate novel therapeutic interventions.

1.3.1 Tumor infiltrating lymphocytes (TIL) in PDAC

Adaptive immune responses are an essential part of the immunological heterogeneity in PDAC, with different populations of tumor infiltrating lymphocytes (TIL) being involved. As one subfamily of TIL, T cells can either support or impede tumor formation by taking on distinct effector phenotypes (Group Young Researchers In Inflammatory Carcinogenesis et al., 2021; Huber et al., 2020).

The subpopulation of $CD8^+$ cytotoxic T cells conveys an effective anti-tumor immune response via release of cytotoxic granules containing perforin and granzymes, secretion of cytokines including TNF-α and IFN-γ, and Fas ligand-mediated activation of the caspase cascade (Raskov et al., 2021). In PDAC, an increased accumulation of $CD8^+$ cytotoxic T cells in close proximity to the tumor epithelium has been found to correlate with improved outcomes (Balli et al., 2017; Carstens et al., 2017). However, these infiltrates are restricted to the stromal compartment in most tumors and often display signs of $CD8^+$ T cell dysfunction (Stromnes et al., 2017; Bailey et al., 2016a). This state of functional exhaustion is characterized by a decreased production of cytotoxic molecules and cytokines with consequent loss of effector capacity and by the upregulation of inhibitory checkpoint receptors such programmed cell death 1 (PD-1), cytotoxic T-lymphocyte-associated protein 4 (CTLA-4) and T cell immunoreceptor with Ig and ITIM domains (TIGIT) (Saka et al., 2020; McLane et al., 2019). Despite representing a promising target for immunotherapy, inhibition of immune checkpoint receptors has so far failed to improve outcomes in PDAC patients (Brahmer et al., 2012; Royal

et al., 2010; O'Reilly et al., 2019), presumably due to the low baseline T cell infiltration in most tumors (Morrison et al., 2018). Novel therapeutic strategies aiming to modify both abundance and spatial localization of $CD8^+$ cytotoxic T cells could therefore enable effective responses to immunotherapy.

$CD4^+$ helper T cells constitute a heterogenous T cell subpopulation with an ambivalent role in PDAC (Group Young Researchers In Inflammatory Carcinogenesis et al., 2021). Upon antigenic stimulation, naïve CD4 T cell precursors are activated, followed by cytokine-dependent differentiation into specific subsets of effector cells, including Th1, Th2 and regulatory T cells (Sallusto & Lanzavecchia, 2009). In PDAC, the TME promotes a Th2-dominated $CD4^+$ helper T cell infiltration associated with reduced survival (De Monte et al., 2011; Tassi et al., 2008). The pro-tumorigenic property of Th2 cells derives from their ability to secrete specific interleukins such as IL-4 and IL-13, resulting in M2-polarization of macrophages, fibrotic ECM remodeling and inhibition of Th1 differentiation (Sica et al., 2006; Wynn, 2004; Mittrücker et al., 2014). In contrast, shifting the balance towards Th1 potentially enhances anti-tumor immunity, as Th1 cells recruit and activate $CD8^+$ cytotoxic T cells via secretion of IFN-γ and IL-2 (Foucher et al., 2018; Liao et al., 2013). However, IFN-γ also induces upregulation of inhibitory checkpoint molecules (Chen et al., 2019), suggesting a more complex role of Th1-mediated immunity in PDAC.

In order to maintain homeostasis and prevent autoimmunity, the subpopulation of regulatory T cells acts to suppress immune responses via multiple mechanisms, including secretion of inhibitory cytokines such as IL-10 and TGF-β, metabolic disruption inducing apoptosis in the target cell and modulation of antigen-presenting cells (Vignali et al., 2008). The concomitant effect of limited anti-tumor immunity is highly relevant in PDAC, as the number of tumor-infiltrating regulatory T cells was found to increase upon tumor progression and to correlate with a poor prognosis (Hiraoka et al., 2006; Tang et al., 2014; Ikemoto et al., 2006). Conversely, tumor infiltration characterized by a relative paucity of regulatory T cells in combination with increased fractions of $CD8^+$ cytotoxic T cells, total $CD4^+$ T cells and M1-polarized macrophages was associated with longer survival of PDAC patients (Ino et al., 2013). Even so, regulatory T cells can also adopt a tumor-restraining role by promoting TGF-β-dependent differentiation of myofibroblastic CAFs (Chellappa et al., 2016; Rhim et al., 2014), albeit of to date unknown clinical significance in PDAC.

In addition to the complex role of T cells, the function of B cells in PDAC remains controversial. Upon antigen-triggered activation and differentiation into antibody-producing plasma cells, B cells become the key cells of humoral immunity, but they also exert additional functions, including secretion of cytokines and modulation of T cell and innate immune responses (Tsou et al., 2016). Different functional phenotypes have further been described for mature B cells,

with both promoting and inhibiting roles in tumor immunity (Largeot et al., 2019). Notably, IL-35-secreting regulatory B cells have been found to directly stimulate tumor cell proliferation in a mouse model of PDAC (Pylayeva-Gupta et al., 2016), a phenotype also known to inhibit T cell mediated immunity (Gunderson et al., 2016; Largeot et al., 2019). However, analyses on human samples suggest a more complex picture, as long-term survivors of PDAC demonstrated a higher density of B cell aggregates at the invasive tumor margins (Brunner et al., 2020). In this regard, the ability of B cells to form tertiary lymphoid structures (TLS) together with T cells and dendritic cells at sites of long-lasting inflammation, including tumors, appears to be essential (Trüb & Zippelius, 2021). In contrast to individual infiltrating B cells, only a high density of B cells within TLS was found to correlate with an increased $CD8^+$ cytotoxic T cell infiltration and longer survival of patients (Castino et al., 2016). In mice, induction of TLS formation improved response to chemotherapy (Delvecchio et al., 2021), highlighting the significance of B cells and their interactions with other components of the TME in development of improved treatment strategies.

Compared to other cancer entities, PDAC is generally characterized as an immunologically "cold" tumor, with low T cell-mediated anti-tumor immunity and resistance to immunotherapy (Upadhrasta & Zheng, 2019; Morrison et al., 2018; Thorsson et al., 2018). In consideration of the adaptive immune cell heterogeneity described above, combined genomic and phenotypic PDAC subtyping approaches based on TIL abundance have been proposed, including stratification into "immune escape", "immune exhausted" and "immune rich" subtypes (Wartenberg et al., 2018). Superior outcomes in patients with "immune rich" tumors (Wartenberg et al., 2018; Sadozai et al., 2021) suggest that reshaping the TME into an immunologically "hot" anti-tumorigenic niche could contribute essentially to the success of personalized treatment strategies in PDAC.

1.3.2 Tumor vasculature in PDAC

As a hallmark of cancer, tumor cells induce the formation of a new vascular network, ensuring both oxygen and nutrient supply and facilitating metastasis (Hanahan & Weinberg, 2011; Lugano et al., 2020). One important mechanism of this neovascularization is the process of angiogenesis by which new capillaries develop from preexisting vessels (Carmeliet & Jain, 2011). Besides during embryogenesis, physiological angiogenesis also occurs in adult repair processes such as wound healing and is highly regulated by pro- and anti-angiogenic factors (Papetti & Herman, 2002). Tumors escape these regulation mechanisms by independently producing pro-angiogenic growth factors and signaling molecules such as vascular endothelial growth factor (VEGF) stimulating endothelial cell proliferation and migration (Hida et al., 2018; Papetti & Herman, 2002).

In PDAC, high expression levels of VEGF, platelet-derived growth factor (PDGF), fibroblast growth factor (FGF) and their respective receptors were found to correlate with tumor progression and poor prognosis of patients (Fujimoto et al., 1998; Itakura et al., 1997; Wagner et al., 1998). However, despite promising results in pre-clinical studies (Bruns et al., 2002; Baker et al., 2002), anti-angiogenic agents have failed to significantly improve clinical outcomes so far (Annese et al., 2019; Kindler et al., 2011; O'Reilly et al., 2010).

Besides endothelial cells, perivascular cells constitute an important component of the macro- and microvasculature, with vascular smooth muscle cells enveloping larger arteries and veins, and pericytes covering microvessels (Yamazaki & Mukouyama, 2018). In later stages of angiogenesis, recruitment of pericytes limits proliferation and migration of endothelial cells and stabilizes the newly formed microvascular network (Bergers & Song, 2005; Sweeney & Foldes, 2018). In contrast to these physiological processes, tumor-induced angiogenesis leads to the development of a structurally and functionally abnormal vasculature, characterized by a lack of perivascular cells and increased permeability of the vessel wall (Lugano et al., 2020; Nagy et al., 2012; Nishida et al., 2006).

PDAC present a similarly immature tumor vasculature, further being impaired by the extensive desmoplastic stromal reaction causing high interstitial pressure (van der Zee et al., 2011; Rhim et al., 2014). The subsequently reduced perfusion further promotes hypoxia and acidosis in the TME, thus limiting immune cell infiltration and drug availability while simultaneously promoting tumor proliferation and metastasis (Jiang et al., 2020; Munn & Jain, 2019; Olive et al., 2009; Provenzano et al., 2012). Both high microvascular density and low coverage with perivascular cells resulting in increased vascular fragility have been linked to poorer prognosis of PDAC patients (Barău et al., 2013; Wang et al., 2013). These alterations of the tumor vasculature thus represent possible targets of therapies aiming at vascular normalization beyond anti-angiogenesis (Munn & Jain, 2019; Huang et al., 2013).

Furthermore, the reduced expression of cell adhesion molecules (CAMs), such as selectins, ICAM and VCAM, on endothelial cells of the tumor vasculature impairs the adhesion cascade necessary for leukocyte extravasation, thus representing an important immune escape mechanism in cancer (Harjunpää et al., 2019). Conversely, upregulation of CAMs has been associated with increased lymphocytic infiltration and improved outcomes in various cancer entities (Harjunpää et al., 2019; Mlecnik et al., 2010; Ogawa et al., 1998; Koyama et al., 1992). In mouse models of PDAC, senescence-induced vascular remodeling including upregulation of CAMs was accompanied by an increased cytotoxic T cell infiltration (Ruscetti et al., 2020). However, in tumor-derived endothelial cells from human PDAC samples, high expression levels of VCAM and L1CAM were found to directly promote infiltration of immunosuppressive regulatory T cells in a mouse model (Nummer et al., 2007) and enhance tumor cell adhesion

and transendothelial migration *in vitro* (Issa et al., 2009). Still, clinical and prognostic relevance of CAMs in PDAC remains unclear, highlighting the need of further investigations.

1.4 Oncogenic KRAS

The three *RAS* genes *HRAS*, *NRAS* and *KRAS* are the most common oncogenes in human cancer (The Cancer Genome Atlas). They encode four highly homogenous ~21 kDa proteins, with the KRAS isoforms KRAS4A and KRAS4B being derived from alternative splicing. RAS proteins belong to the class of small guanosine triphosphatases (GTPases) which respond to extracellular ligand-induced activation of receptor tyrosine kinases (RTKs) and other receptors on the cell surface and function as intracellular binary molecular switches, transitioning between an inactive guanosine diphosphate (GDP)-bound and an active GTP-bound state (Bourne et al., 1990; Lowy & Willumsen, 1993; Wittinghofer & Pai, 1991). This GDP/GTP cycling is regulated by guanine nucleotide exchange factors (GEFs), such as SOS, which promote formation of active RAS by facilitating the exchange from GDP to GTP, and by GTPase-activating proteins (GAPs) which trigger the intrinsic GTPase activity of RAS, thus accelerating GTP hydrolysis to GDP and consequent RAS inactivation (Vetter & Wittinghofer, 2001). Only in the active GTP-bound state, RAS is able to interact with diverse effector proteins of downstream signaling pathways, including RAF and PI3K (Simanshu et al., 2017).

Comprising 85% of all RAS mutations, KRAS is the most frequently mutated RAS gene in human cancer, with predominance in pancreatic, lung and colorectal cancer. Almost all *KRAS* mutations are activating point mutations affecting the residues glycine 12 (G12), G13 and glutamine 61 (Q61) in the KRAS protein, with G12 being the most frequently involved. Specific mutations dominate in different cancer entities: while most KRAS mutations in PDAC and colorectal carcinoma are G to aspartic acid substitutions ($Kras^{G12D}$), G to valine ($Kras^{G12V}$) and G to cysteine ($Kras^{G12C}$) exchanges are predominant in non-small cell lung cancer (NSCLC) (Catalogue of Somatic Mutations in Cancer (COSMIC) database v95). These point mutations all hinder interaction of GAPs with the KRAS protein, thus impairing its intrinsic GTPase activity. In a permanent GTP-bound state, KRAS functions independently of RTK activation, resulting in constitutive activation of multiple downstream signaling pathways involved in cell proliferation and survival (Pylayeva-Gupta et al., 2011; Hunter et al., 2015; Scheffzek et al., 1997).

Activating mutations in *KRAS* occur in > 90% of PDAC patients (Cancer Genome Atlas Research Network, 2017). An increased gene dosage and elevated expression levels of mutant $Kras^{G12D}$ have been identified as the main drivers of tumorigenesis and progression in both human and murine PDAC. In line with the molecular and morphological heterogeneity of PDAC, the mesenchymal, basal-like subtype was found to display the highest $Kras^{G12D}$

expression levels and a strong gene set enrichment for RAS downstream signaling pathways, correlating with increased metastatic potential and poor clinical outcomes (Mueller et al., 2018; Dijk et al., 2020; Chan-Seng-Yue et al., 2020).

The central role of mutant KRAS in PDAC and other cancer entities has prompted intense research on its suitability as a therapeutic target. While RAS was considered “undruggable” for a long time, clinical studies on allele-specific inhibitors of $Kras^{G12C}$ which covalently target the cysteine 12 residue via an inducible allosteric drug-binding pocket have yielded promising results particularly in treatment of NSCLC patients (Ostrem et al., 2013; Canon et al., 2019), for which the first direct $Kras^{G12C}$ inhibitor sotorasib has just received FDA and EMA approval. However, this approach is not suitable to inhibit $Kras^{G12D}$ as it lacks the reactive cysteine and exhibits different biochemical properties (Moore et al., 2020), thus rendering development of $Kras^{G12D}$-directed therapy more complex and therapeutic approaches targeting downstream effector molecules more attractive.

1.5 The RAF/MEK/ERK pathway

The main downstream signaling route of KRAS is the RAF/MEK/ERK pathway, also known as mitogen-activated protein kinase (MAPK) pathway. Following upstream signaling-induced GTP-loading, activated RAS induces dimerization and activation of RAF proteins which include the serine/threonine-specific protein kinases A-RAF, B-RAF and C-RAF. Activated RAF phosphorylates and thereby activates the dual specificity kinases MEK1 and MEK2 which can act as both tyrosine-specific and serine/threonine-specific protein kinases. Activated MEK1 and MEK2 in turn phosphorylate the MAP kinases ERK1 and ERK2 on threonine (T) and tyrosine (Y) residues within the conserved T202-E203-Y204 motif. Activated ERK1 and ERK2 can subsequently translocate into the nucleus to activate a multitude of downstream targets via their serine/threonine-specific kinase activity, thus regulating diverse cellular programs such as proliferation, differentiation, cell cycle progression, survival, apoptosis and gene expression (Mandal et al., 2016; Cargnello & Roux, 2011).

Given its essential role in pancreatic tumorigenesis (Collisson et al., 2012) and its association to the biological aggressiveness of the mesenchymal subtype (Mueller et al., 2018), the RAF/MEK/ERK pathway represents a highly relevant signaling axis in PDAC with several potentially druggable targets. Among those, MEK1/2 occupies a particularly interesting position regarding therapeutic inhibition, located downstream of both RAS- and RAF-related driver mutations, the latter occurring in most cases of malignant melanoma and, at lower frequency, in many other cancer entities (Davies et al., 2002). The potency of MEK inhibition further derives from the fact that MEK1 and MEK2 are the only activators of ERK1 and ERK2 and thus function as “gatekeeper” kinases bundling inputs from multiple upstream effector

molecules (Caunt et al., 2015). Trametinib was the first MEK inhibitor to be FDA/EMA approved for the treatment of B-RAF-mutant locally advanced or metastatic melanoma and NSCLC (Gilmartin et al., 2011; Planchard et al., 2017). While also demonstrating promising efficacy in KRAS-mutant NSCLC (Jänne et al., 2013; Blumenschein et al., 2015), single-agent MEK inhibition with or without chemotherapy failed to improve prognosis in molecularly unstratified PDAC patients (Bodoky et al., 2012; Infante et al., 2014). To limit MEK inhibitor bypass mechanisms contributing to therapy resistance, including unrestrained feedback activation of upstream RTK and upregulation of alternative downstream pathways such as PI3K (Collisson et al., 2012; Pettazzoni et al., 2015; Mirzoeva et al., 2013; Balmanno et al., 2009), preclinical studies on different KRAS-mutant cancer cell lines have addressed the development of combinatorial treatment regimens. In KRAS-mutant PDAC, promising results have been reported for combined inhibition of MEK and upstream RTK (Pettazzoni et al., 2015) or SHP2, a protein tyrosine phosphatase which links RTK signaling to the RAS/RAF/MEK/ERK pathway (Mainardi et al., 2018; Ruess et al., 2018). However, differences in therapy responses among distinct PDAC subtypes and the effects of such combinatorial drug treatments on the TME have not been explored yet. To account for the great tumor cell- and TME-related heterogeneity of the disease, systematic investigations of subtype-specific therapeutic vulnerabilities are thus required for the development of MEK inhibition-based combination therapies in KRAS-mutant PDAC.

1.6 A novel combinatorial treatment approach

Given the central role of mutant KRAS in tumorigenesis and evolution of human PDAC (hPDAC), genetically engineered mouse models (GEMMs) of PDAC such as *Pdx1-Cre;LSL-Kras$^{G12D/+}$* and *Ptf1a$^{Cre/+}$;LSL-Kras$^{G12D/+}$* (see Methods, p.22 and Figure 6 (A)) which are characterized by pancreas-specific conditional expression of oncogenic Kras^{G12D} are often employed to mimic molecular and morphological characteristics of hPDAC. These animals first develop pancreatic intraepithelial neoplasia (PanIN) lesions, which progress, analogously to hPDAC, from low-grade (PanIN 1A/B) to high-grade (PanIN 3) PDAC precursor lesions with increasing degrees of cytological and architectural atypia before further developing with long latency into invasive metastatic PDAC (Eser et al., 2014; Hingorani et al., 2003; Hruban et al., 2000). Initiated by mutant KRAS as oncogenic driver, this phenotypic progression is accompanied by somatic molecular alterations in most cases, notably by the loss of tumor suppressors such as p16^{INK4A}, p19^{ARF} and p53 (Bardeesy & DePinho, 2002). To accelerate PanIN formation and promote progression into invasive and metastatic PDAC, GEMMs with conditional expression of both *Kras^{G12D}* and the gain of function *Trp53^{R172H}* allele (*Pdx1-*

Cre;LSL-Kras$^{G12D/+}$;LSL-Trp53$^{R172H/+}$) have been generated (Hingorani et al., 2005; Olive et al., 2004).

Using *Kras^{G12D}*-driven models as described above and other GEMMs of PDAC, our group generated a large morphologically and molecularly characterized resource of tissue and primary cell lines from murine PDAC (mPDAC) reflecting the multifaceted heterogeneity of hPDAC, including characteristics of classical and mesenchymal subtypes (Mueller et al., 2018). The significance of an increased gene dosage and high expression levels of mutant Kras^{G12D} in PDAC, identified as the main drivers of mesenchymal tumor differentiation and biological aggressiveness of the disease (Chan-Seng-Yue et al., 2020; Mueller et al., 2018), supported the rationale to comprehensively explore the potential of RAF/MEK/ERK pathway inhibition as a treatment strategy for PDAC. To this end, primary Kras^{G12D}-driven mPDAC from the cell culture resource described above and established hPDAC cell lines of the classical and mesenchymal subtype were screened with the MEK inhibitor trametinib. Strikingly, while a strong cytostatic effect of the treatment was observed in classical PDAC cell lines, mesenchymal cell lines were highly resistant to trametinib, a feature which correlated with their Kras^{G12D} expression levels. Furthermore, trametinib did not induce cell death *in vitro* or tumor regression *in vivo* as observed in other cancer entities (Blumenschein et al., 2015; Caunt et al., 2015) in either subtype.

To identify candidates for a synergistic combinatorial treatment, classical and mesenchymal mPDAC and hPDAC cell lines were subsequently screened with 418 drugs under preclinical and clinical investigation in combination with trametinib. A strong synergism particularly in cell lines of the mesenchymal subtype was observed with nintedanib, a multikinase inhibitor with known anti-angiogenic and anti-fibrotic properties mainly mediated via inhibition of VEGFR1/2/3, FGFR1/2/3 and PDGFRα/β signaling (Hilberg et al., 2008), accounting for its efficacy in treatment of idiopathic pulmonary fibrosis (Richeldi et al., 2014; Ackermann et al., 2017) and its experimental clinical use in various cancer entities (Manzo et al., 2016; Ray-Coquard et al., 2020; Scagliotti et al., 2019). In combination with docetaxel chemotherapy, nintedanib is FDA/EMA approved as a second-line treatment of patients with locally advanced, metastatic or locally recurrent adenocarcinoma of the lung, a histologic subtype of NSCLC (Reck et al., 2014; Hanna et al., 2016). While no clinical studies have yet explored its effect on PDAC, nintedanib has been shown to inhibit proliferation of murine and human tumor cells and to enhance response to gemcitabine chemotherapy in murine xenograft models of PDAC (Awasthi et al., 2015), supporting its potential as part of a combinatorial treatment approach.

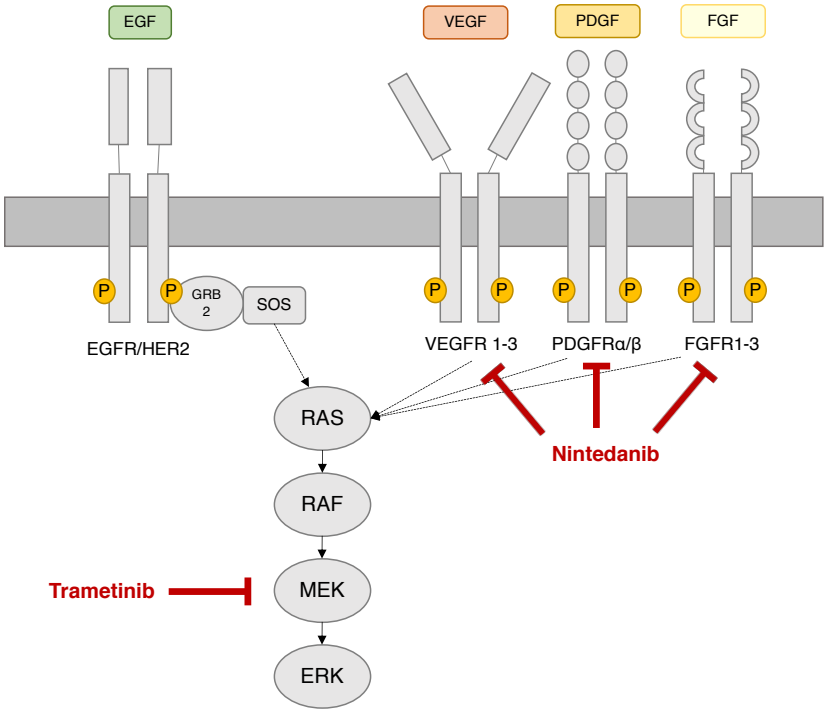

Figure 1: Schematic representation of the combinatorial treatment strategy

Of our mPDAC and hPDAC cell culture resource, cell lines of the mesenchymal subtype were particularly sensitive to the combinatorial treatment. Synergism was also observed for most classical cell lines, but in 3 of 10 hPDAC and 5 of 21 mPDAC cell lines of the classical subtype, the combination of trametinib and nintedanib had antagonistic effects instead. This antagonism could be reversed and turned into synergism by inducing *Kras*^{G12D} overexpression in classical mPDAC cells which thereby gained morphological and gene expression-related features of mesenchymal PDAC, highlighting the impact of mutant KRAS levels on therapy response. Analysis of caspase activity further revealed that neither trametinib nor nintedanib alone, but only the combination of both induced cell death, with the strongest effects observed in mesenchymal cell lines. To explore the potency of the trametinib/nintedanib combination (Figure 1) *in vivo*, classical and mesenchymal mPDAC cells of *Ptf1a*$^{Cre/+}$*;LSL-Kras*$^{G12D/+}$ background were orthotopically transplanted in immunocompetent syngeneic mice (see Figure 10(A)), revealing a remarkable response to the combinatorial treatment particularly in the mesenchymal subtype, as evidenced by significantly reduced tumor volumes and improved survival not only versus the control cohort, but also in comparison to treatment responses of the classical subtype. The combination of trametinib and nintedanib thus represents a potent treatment option specifically for the aggressive mesenchymal Kras^{G12D}-driven PDAC subtype (Falcomatà et al., 2022).

1.7 Objectives

To unravel mechanisms behind this remarkable therapy response, both tumor cell-intrinsic and TME-specific combinatorial treatment-induced changes had to be taken in consideration. Focusing on the TME, the aim of this project was to characterize adaptive immune responses and vascular remodeling induced by the combinatorial treatment with trametinib and nintedanib in comparison to baseline lymphocytic infiltration and tumor vasculature morphology in classical and mesenchymal PDAC subtypes. Therefore, multiplex immunofluorescence staining panels were established and optimized to assess baseline quantity and spatial distribution of tumor-infiltrating adaptive immune cells and their relation to the tumor vasculature in endogenous *Kras*^{G12D}-driven mPDAC of both classical and mesenchymal morphology. To evaluate the subtype-specific impact of the combinatorial drug treatment on the TME, treatment-induced adaptive immune responses and vascular remodeling were analyzed in immunocompetent orthotopic transplantation models of classical and mesenchymal mPDAC using various multiplex immunofluorescence staining panels. Additional orthotopic transplantation experiments based on T cell-deficient *CD3ε-KO* mice were then conducted to validate the contribution of the observed cytotoxic T cell-mediated anti-tumor immunity to therapy response in the mesenchymal subtype.

2 Materials and methods

2.1 Material

2.1.1 Technical equipment

$^{13}C/^{1}H$ Volume Resonator V-XQS-HQS-070	RAPID Biomedical GmbH, Rimpar
2CH Surface Coil Array receive only ^{1}H 300 MHz P-H02LE-070-01507001b	RAPID Biomedical GmbH, Rimpar
Animal holder for rats LHRXGS-00563-022	RAPID Biomedical GmbH, Rimpar
Autoclave Systec VX-75	Systec GmbH, Nürnberg
BD LSRFortessa™	BD Biosciences, Franklin Lakes, NJ, USA
BioSpec® 70/30 7 T MRI system with an HD 205/120 gradient coil	Bruker Corporation, Billerica, MA, USA
Birdcage resonator	RAPID Biomedical GmbH, Rimpar
Centrifuge Heraeus™ Multifuge X3 FR	Thermo Fisher Scientific, Inc., Waltham, MA, USA
Centrifuge Z 323 K	Hermle Labortechnik GmbH, Wehingen
CO_2 incubator HERAcell® 160i	Heraeus Holding GmbH, Hanau
CO_2 incubator HERAcell® 250i	Heraeus Holding GmbH, Hanau
Confocal Laser Scanning Microscope Leica TCS SP8	Leica Microsystems GmbH, Wetzlar
Cryotstat Leica CM3050S	Leica Microsystems GmbH, Wetzlar
Dewar carrying flask, type B	KGW-Isotherm, Karlsruhe
ECG trigger unit	RAPID Biomedical GmbH, Rimpar
GentleMACS™ octo dissociator with heaters	Miltenyi Biotec B.V. & Co. KG, Bergisch Gladbach
Glass ware, Schott Duran®	Schott AG, Mainz
Heated paraffin embedding module EG1150 H	Leica Microsystems GmbH, Wetzlar
HERAsafe® biological safety cabinet	Heraeus Holding GmbH, Hanau

Homogenizer SilentCrusher M with tool 6F	Heidolph Instruments GmbH & Co. KG, Schwabach
Incubator MELAG® 206	MELAG Medizintechnik GmbH & Co. KG, Berlin
Isoflurane Vaporizer Vapor® 2000	Drägerwerk AG & Co. KGaA, Lübeck
Isoflurane Vaporizer MSS 3	MSS International Ltd.,
Microcentrifuge 5427 R	Eppendorf AG, Hamburg
Microscope Axiovert A1	Carl Zeiss AG, Oberkochen
Microscope Camera Axiocam 503 mono	Carl Zeiss AG, Oberkochen
Microscope Camera Leica ICC50 W	Leica Microsystems GmbH, Wetzlar
Microscope Aperio VERSA 8 Digital Pathology Scanner	Leica Microsystems GmbH, Wetzlar
Microscope Leica DM500	Leica Microsystems GmbH, Wetzlar
Microscope Leica DM IL LED	Leica Microsystems GmbH, Wetzlar
Microtome Microm HM355S	Thermo Fisher Scientific, Inc., Waltham, MA, USA
Microwave	Ok., Imtron GmbH, Ingolstadt
Mini centrifuge LLG-uniCFUGE 2	Lab Logistics Group GmbH, Meckenheim
Multi-Axle-Rotating-Mixer RM5	Ingenieurbüro CAT M. Zipperer GmbH, Staufen
Neubauer Hemocytometer improved Assistent®	Glaswarenfabrik Karl Hecht GmbH & Co KG, Sondheim vor der Rhön
Paraffin tissue floating bath Microm SB80	Thermo Fisher Scientific, Inc., Waltham, MA, USA
Pipette Controller Pipetus®	Hirschmann Laborgeräte GmbH & Co. KG, Eberstadt
Pipette Controller Stripettor™ Ultra	Corning, Inc., NY, USA
Pipettes Reference®, Research®, Research Plus®	Eppendorf AG, Hamburg
Precision balance PCB 3500-2	Kern & Sohn GmbH, Balingen-Frommern
Surgical instruments	Thermo Fisher Scientific, Inc., Waltham, MA, USA
Two-channel flexible array coil	RAPID Biomedical GmbH, Rimpar
Vortex mixer Vortex-Genie 2	Scientific Industries, Inc., NY, USA
Water bath 1083	GFL Gesellschaft für Labortechnik mbH, Burgwedel

2.1.2 Disposables

Cell culture plasticware	Greiner Bio-One International GmbH, Kremsmünster, AT TPP Techno Plastic Products AG, Trasadingen, CH
Cell scrapers	TPP Techno Plastic Products AG, Trasadingen, CH
Cell strainers (70 µm mesh size)	Greiner Bio-One International GmbH, Kremsmünster, AT
Cell strainers CellTrics® (30 µm mesh size)	Sysmex K.K., Kobe, JP
Clips for skin	Thermo Fisher Scientific, Inc., Waltham, MA, USA
Conical tubes (15 and 50 ml)	Greiner Bio-One International GmbH, Kremsmünster, AT Sarstedt AG & Co. KG, Nümbrecht
Cover slips (Menzel-Gläser)	Thermo Fisher Scientific, Inc., Waltham, MA, USA
CryoPure tubes (1.6 ml)	Sarstedt AG & Co. KG, Nümbrecht
Disposable scalpels	Feather Safety Razor Co., Ltd., Osaka, Japan
GentleMACS™ C tubes for tissue dissociation	Miltenyi Biotec B.V. & Co. KG, Bergisch Gladbach
Glass slides Superfrost Plus™ (Menzel-Gläser)	Thermo Fisher Scientific, Inc., Waltham, MA, USA
Microtome blades S35 and C35 (also used for cryostat)	Feather Safety Razor Co., Ltd., Osaka, Japan
Microtome blades MB22 Premier	Thermo Fisher Scientific, Inc., Waltham, MA, USA
Parafilm® M	Merck KGaA, Darmstadt
Pasteur pipettes	Hirschmann Laborgeräte GmbH & Co. KG, Eberstadt
Petri dishes	Sarstedt AG & Co. KG, Nümbrecht
Pipette tips	Biozym Scientific GmbH, Hessisch Oldendorf Corning Inc., NY, USA Sarstedt AG & Co. KG, Nümbrecht
Reaction tubes (0.5, 1.5, 2 ml)	Eppendorf AG, Hamburg

Round-bottom polystyrene sample tubes for flow cytometry (5 ml)	Sarstedt AG & Co. KG, Nümbrecht
Serological Pipettes CELLSTAR® (2 ml, 5 ml, 10 ml, 25 ml, 50 ml)	Greiner Bio-One International GmbH, Kremsmünster, AT
Single-use needles Sterican®	B. Braun SE, Melsungen
Single-use syringes Omnifix®	B. Braun SE, Melsungen
Sutures ETHILON® 5-0	Ethicon, Inc., Raritan, NJ, USA
Tissue embedding cassette system	Medite Medical GmbH, Burgdorf

2.1.3 Reagents and enzymes

Dimethyl sulfoxide (DMSO)	Merck KGaA, Darmstadt
Dulbecco's phosphate buffered saline (PBS) powder	Biochrom GmbH, Berlin, Germany
Ethanol absolut	Otto Fischar GmbH & Co. KG, Saarbrücken
Ethanol 96%	Otto Fischar GmbH & Co. KG, Saarbrücken
Ethanol 80%	BrüggemannAlcohol Heilbronn GmbH, Heilbronn
Glycerol	Merck KGaA, Darmstadt
Methylcellulose	Merck KGaA, Darmstadt
Mouse tumor dissociation kit (RRID: SCR_020285)	Miltenyi Biotec B.V. & Co. KG, Bergisch Gladbach
O.C.T™ compound Tissue-Tek®	Sakura Finetek Germany GmbH, Staufen
Paraformaldehyde	Merck KGaA, Darmstadt
Type F Immersion Liquid n_e^{23} = 1.5180 v_e = 46	Leica Microsystems GmbH, Wetzlar
Zombie Aqua™ fixable viability kit	BioLegend, San Diego, CA, USA

2.1.4 Cell culture

2.1.4.1 Cell culture reagents

Dulbecco's modified eagle medium (DMEM) with L-glutamine, high glucose	Merck KGaA, Darmstadt

Dulbecco's phosphate buffered saline (PBS)	Merck KGaA, Darmstadt
Fetal bovine serum (FBS)	Biochrom GmbH, Berlin, Germany
Penicillin (10000 units/ml) / Streptomycin (10000 µg/ml) solution	Merck KGaA, Darmstadt
Trypan Blue solution	Merck KGaA, Darmstadt
Trypsin, 0.05% with 0.53 mM EDTA 4Na	Thermo Fisher Scientific, Inc., Waltham, MA, USA

2.1.4.2 Cell culture media

Cancer cell medium	DMEM 10% FBS 1% Penicillin/Streptomycin
Freezing medium	70% DMEM 20% FBS 10% DMSO

2.1.5 Drugs

GSK1120212 Trametinib (Selleck Chemicals, Houston, TX, USA)
BIBF 1120 Nintedanib (Selleck Chemicals, Houston, TX, USA)
Isoflurane CP® 1ml/ml (CP-Pharma Handelsgesellschaft mbH, Burgdorf)
Metacam® Meloxicam (Boehringer Ingelheim Pharma GmbH & Co. KG, Ingelheim am Rhein)
MMF (midazolam, medetomidine and fentanyl) and AFN (atipamezole, flumazenil, naloxone) (both prepared by the pharmacy of Klinikum rechts der Isar, TU Munich, Germany)

2.1.6 Staining reagents

Acetone	Otto Fischar GmbH & Co. KG, Saarbrücken
Bovine serum albumin, fraction V	SERVA Electrophoresis GmbH, Heidelberg
DAPI	Biotium
Eosine	Waldeck GmbH & Co KG, Münster
Hematoxylin	Carl Roth GmbH + Co. KG, Karlsruhe
Mounting medium Richard-Allan Scientific™	Thermo Fisher Scientific, Inc., Waltham, MA, USA

Normal donkey serum	Linaris Biologische Produkte GmbH, Dossenheim
Normal goat serum	Linaris Biologische Produkte GmbH, Dossenheim
Normal rabbit serum	Vector Laboratories, Inc., Burlingame, CA, USA
Normal rat serum	Thermo Fisher Scientific, Inc., Waltham, MA, USA
Roti® Histofix 4%	Carl Roth GmbH + Co. KG, Karlsruhe
Roti® Histol	Carl Roth GmbH + Co. KG, Karlsruhe
Sucrose	Merck KGaA, Darmstadt
TO-PRO™-3 (T3605)	Thermo Fisher Scientific, Inc., Waltham, MA, USA
Triton® X-100	Merck KGaA, Darmstadt
Vectashield® Antifade Mounting Medium	Vector Laboratories, Inc., Burlingame, CA, USA

2.1.7 Antibodies

2.1.7.1 Flow cytometry

Antibody name	**Dilution**	**Company**	**Cat. No.**	**RRID**
CD4 BUV805 (Clone GK1.5)	1:100	BD Biosciences	#564922	AB_2827960
CD3ε BUV395 (Clone 145-2C11)	1:20	BD	#563565	AB_2738278
CD8a BV785 (Clone 53-6.7)	1:100	Biolegend	#100749	AB_11218801
CD25 BV650 (Clone PC61)	1:50	Biolegend	#102037	AB_11125760
TCRγ/δ BV421 (Clone GL3)	1:50	Biolegend	#118119	AB_10896753
CD45 PerCP Cy5.5 (Clone I3/2.3)	1:100	Biolegend	#147705	AB_2563537
CD19 FITC (Clone 6D5)	1:100	Biolegend	#115505	AB_313640
CD62L PE (Clone MEL-14)	1:500	Biolegend	#104407	AB_313094
CD44 APC/Cyanine7 (Clone IM7)	1:30	Biolegend	#103027	AB_830784
EpCAM AF647 (Clone G8.8)	1:200	Biolegend	#118212	AB_1134101
CD11c BUV737 (Clone HL3)	1:30	BD Biosciences	#564986	AB_2739034
NK1.1 BUV395 (Clone PK136)	1:25	BD Biosciences	#564144	AB_2738618
Ly6C BV785 (Clone HK1.4)	1:200	Biolegend	#128041	AB_2565852
CD11b BV650 (Clone M1/70)	1:100	Biolegend	#101239	AB_11125575
F4/80 BV421/PB (Clone BM8)	1:30	Biolegend	#123131	AB_10901171

Siglec-F BB515 (Clone E50-2440)	1:100	BD Biosciences	#564514	AB_2738833
Ly6G PE (Clone 1A8)	1:200	Biolegend	#127607	AB_1186104
CD68 APC/Cyanine7 (Clone FA-11)	1:20	Biolegend	#137023	AB_2616812
TruStain FcX CD16/32 (Clone 93)	1:300	Biolegend	#101320	AB_1574975

Table 1: Antibodies used for flow cytometry

2.1.7.2 Multiplex immunofluorescence staining

2.1.7.2.1 Primary antibodies

Antibody name	**Dilution**	**Company**	**Cat. No.**	**RRID**
Rat anti-CD3 (Clone 17A2)	1:50	Biolegend	#100201	AB_312658
Rat anti-CD45R/B220		BD Biosciences	#553084	AB_394614
CD4 AF532 (Clone RM4-5)		Thermo Fisher Scientific	#58-0042-82	AB_11218891
CD8a AF488 (Clone 53-6.7)		Thermo Fisher Scientific	#53-0081-82	AB_469897
FOXP3 eFluor450 (FJK 16s)		Thermo Fisher Scientific	#48-5773-82	AB_1518812
Armenian hamster anti-CD31 (Clone 2H8)	1:400	Abcam	ab119341	AB_10900179
Rabbit anti-CK18 (polyclonal)	1:5000	Sigma-Aldrich (Merck KGaA)	#SAB4501665	AB_10746153
Chicken anti-Vimentin (polyclonal)	1:1000	Thermo Fisher Scientific	#PA1-16759	AB_2257294
Rabbit anti-alpha smooth muscle Actin (polyclonal)	1:100	Abcam	ab5694	AB_2223021
Rabbit anti-CD62P / P-Selectin (polyclonal)	1:200	LSBio (LifeSpan)	LS-B3578-50	AB_10629269

Table 2: Primary antibodies used for multiplex immunofluorescence staining

2.1.7.2.2 Secondary antibodies

Donkey anti-rat IgG AF488 (polyclonal)	1:200	Thermo Fisher Scientific	#A-21208	AB_2535794

Donkey anti-rat IgG AF594 (polyclonal)	1:200	Thermo Fisher Scientific	#A-21209	AB_2535795
Goat anti-rat IgG AF680 (polyclonal)		Thermo Fisher Scientific	#A-21096	AB_10561521
Goat anti-rabbit IgG AF480 (polyclonal)		Thermo Fisher Scientific	#A-11034	AB_2576217
Donkey anti-rabbit IgG AF480 (polyclonal)		Thermo Fisher Scientific	#A-21206	AB_2535792
Donkey anti-rabbit IgG AF680 (polyclonal)		Thermo Fisher Scientific	#A-27042	AB_2536103
Goat anti-chicken IgG AF680 (polyclonal)		Thermo Fisher Scientific	#A-32934	AB_2762846
Goat anti-Armenian hamster IgG Cy™3 (polyclonal)		Jackson Immuno Research Labs	#127-165-160	AB_2338989

Table 3: Secondary antibodies used for multiplex immunofluorescence staining

2.1.8 Software

Fiji ImageJ2 version 2.0.0 (National Institutes of Health, Bethesda, MD, USA)

FlowJo software version 10.6.2 (Becton, Dickinson & Company, Ashland, OR, USA)

GraphPad Prism version 8.4.2 (GraphPad Software, La Jolla, CA, USA)

Horos Viewer version 3.3.6 (Horos Project, sponsored by Nimble Co, LLC d/b/a Purview, Annapolis, MD USA)

Leica Aperio ImageScope (Leica Microsystems CMS GmbH, Wetzlar, Germany)

Leica Application Suite X (Leica Microsystems CMS GmbH, Wetzlar, Germany)

QPath version 0.3.1 (QuPath developers, The University of Edinburgh, United Kingdom)

2.2 Methods

2.2.1 Mouse experiments

All animal studies were conducted in compliance with European guidelines for the care and use of laboratory animals and were approved by the Institutional Animal Care and Use Committees (IACUCs) of the local authorities of the Technical University of Munich and the Regierung von Oberbayern. In all animal studies, a tumor size of 1.5 cm or a specific cumulative burden score permitted by the IACUCs and Regierung von Oberbayern, determined by signs of advanced disease including cachexia, hunched posture, paralysis,

severe behavioral abnormalities, ascites or jaundice, were not exceeded. Mice were kept in a suitable animal room with a light/dark cycle of 12 h / 12 h, a controlled temperature between 20 and 24°C and a relative air humidity of 55%.

2.2.1.1 The *Kras^{G12D}*-driven genetically engineered mouse model (GEMM)

The strains hereinafter referred to have a mixed C57Bl/6J;129S6/SvEv genetic background. As an endogenous tumor model and for the generation of primary mPDAC cell lines, a previously described conditional Cre-loxP system was used where *Pdx1-Cre* (Hingorani et al., 2003) or *Ptf1a$^{Cre/+}$* mice (Nakhai et al., 2007) expressing a pancreas-specific Cre recombinase under the control of Pdx1 or Ptf1a promoters were intercrossed with a strain carrying a mutated proto-oncogene silenced by a lox-Stop-lox (LSL) cassette. All endogenous tumor mice and cell lines described in this manuscript are based on the knock-in strain *LSL-Kras$^{G12D/+}$* (Jackson et al., 2001) generated in the laboratory of Prof. Dr. med. Dieter Saur. The point mutation G12D, characterized by a substitution of glycine by aspartic acid at position 12 in the GTPase KRAS, is frequently found in hPDAC (see introduction). Deletion of the LSL cassette via pancreas-specific upregulation of Cre leads to the expression of Kras^{G12D}, causing altered KRAS function with constitutive activation of the KRAS signaling pathway.

2.2.1.2 Primary PDAC cell lines for transplantation experiments

Two molecularly annotated primary mPDAC cell lines that had previously been generated in the laboratory of Prof. Dr. med. Dieter Saur were used for transplantation experiments. The cell lines were tested and confirmed to be mycoplasma-free. Details of each cell line can be found in Table 4. Tumor cells had been extracted from pancreatic tissue after dissection of endogenous tumor mice via incubation of minced tumor samples in cancer cell medium (DMEM, supplemented with 10% FBS and 1% penicillin / streptomycin) with 200 U/ml collagenase type II overnight at 37°C, centrifugation at 1000 rpm for 5 min at room temperature (RT) and resuspension of the pellet in cancer cell medium for further processing, cultivation and cryopreservation at -80°C.

ID	Origin	Recombinase	Oncogene	Morphology	Transcriptome
8661	Primary pancreatic tumor (PPT)	Ptf1a-Cre	*LSL-Kras$^{G12D/+}$*	epithelial	classical
9091	PPT	Ptf1a-Cre	*LSL-Kras$^{G12D/+}$*	mesenchymal	basal-like

Table 4: Primary mPDAC cell lines used for orthotopic transplantation experiments

2.2.1.3 Culturing of cancer cells for transplantation experiments

Cryopreserved cancer cells were thawed on ice, resuspended in cancer cell medium, and centrifuged at 1000 rpm for 5 min at RT. After removal of the supernatant, cells were resuspended in cancer cell medium and seeded in a cell culture flask. They were then cultivated in cancer cell medium at 37°C, 5% CO_2 and 100% humidity until a confluent monolayer was reached. For passaging, the medium was aspirated, cells were washed with PBS and trypsinized with 1 ml trypsin / EDTA for 2 – 10 min at 37°C. When cells were detaching from the culture flask, trypsinization was stopped by adding cancer cell medium. The cell suspension was homogenized and seeded in new cell culture flasks. Abundance of cells was assessed by loading a 1:1 dilution of the cell suspension and trypan blue onto a Neubauer hemocytometer for counting under the microscope. For use in transplantation experiments (see Figure 10(A) and Figure 15(A)), trypsinized cells were counted as described and diluted to a final concentration of 2500 cells in 25 µl DMEM without FBS or penicillin / streptomycin.

2.2.1.4 Orthotopic transplantation mouse model

For transplantation experiments, two- to five-month-old syngeneic immunocompetent C57Bl/6J mice and T cell-deficient CD3ε knockout (*CD3εKO*) mice (DeJarnette et al., 1998) were anaesthetized with an intraperitoneal injection of 50 µl of MMF (5 mg/kg midazolam, 500 µg/kg medetomidine and 50 µg/kg fentanyl). Protective eye lubricating ointment was applied, and fur was shaved in the left flank. For the surgery, mice were placed under a heating lamp and fixed in right lateral position. The surgical field was disinfected with 80% ethanol. A 5 mm left-flank incision of the skin was performed, followed by opening of the peritoneal cavity. The pancreas was located next to the spleen and extracorporealized by gentle pull. A suspension of 2500 mPDAC cells in 25 µl DMEM was injected into the tail of the pancreas using a glass syringe and 27-gauge needle. After replacement of the pancreas to its anatomic position, the peritoneum was sutured using 5/0-gauge coated vicryl sutures and the skin was clipped. To antagonize MMF anaesthesia and provide analgesia, 250 µl of AFN (750 µg/kg atipamezole, 500 µg/kg flumazenil, 1,2 mg/kg naloxone) and 150 µl of meloxicam (Metacam®) were administered via intraperitoneal (2/3) and subcutaneous (1/3) injection. Mice were then put in a warming chamber for 30 to 60 min until full recovery. Oral meloxicam was administered for 2 days post-surgery and wounds were inspected carefully.

2.2.1.5 Surveillance of tumor growth kinetics via magnetic resonance imaging (MRI)

In cooperation with AG Schilling, weekly magnetic resonance imaging (MRI) scans of the pancreas were performed. Mice were anaesthetized using an isoflurane vaporizer set to 5% for 2 min in an induction chamber. Lubricating eye ointment was applied and animals were

placed on an animal holder. For maintenance of the anaesthesia during image acquisition, 1,5% to 2% isoflurane, depending on sex, weight and health status of the mouse, were continuously administered with oxygen at 2 l/min via a mask. A Bruker BioSpec 70/30 7 T MRI scanner with a 205/120 HD gradient coil and a flexible two-channel surface coil array was used to scan 35 consecutive abdominal sections. A transaxially oriented T2-weighted fast spin-echo (FSE) scan (slice thickness = 1 mm, repetition time (TR) = 4000 ms, effective echo time (TE) = 48 ms, 4 averages, 12 echoes per excitation, 128x128 in-plane matrix, 32x32 mm^2 field of view, 0.25x0.25 mm^2 in-plane pixel size, total acquisition time = 2 min 40 s) was acquired in accordance with cardiac and respiratory cycles to minimize motion effects during imaging. For reconstruction of MRI volumetric measurements and quantification of tumor volumes, the open-source medical image viewer Horos was used.

2.2.1.6 *In vivo* treatment

When tumors grew to a size of ~100 mm^3 as evidenced by weekly MRI, mice were randomized to control and experimental cohorts. In the experimental cohort, the following combinatorial drug treatment was administered intragastrically via oral gavage: trametinib (3 mg/kg, 5 days a week) and nintedanib (50 mg/kg, 5 days a week) in a 1% methylcellulose suspension. Control animals received vehicle treatment. Details on experimental set ups are shown in the results section (see Figure 10(A) and Figure 15(A)). Mice were monitored daily for morbidity and clinical disease progression and weekly MRI screenings for assessment of tumor growth kinetics were continued. Mice were either sacrificed upon completion of the treatment (timepoint) or when reaching the human endpoint (survival).

2.2.1.7 Mouse dissection

Mice were euthanized with isoflurane / carbon dioxide, fixed, and disinfected with 80% ethanol. Midline laparotomy was performed and internal organs were dissected. The pancreas was weighed and measured. Samples of the pancreatic tumor were acquired as sterile as possible. For flow cytometry, a piece of tumor tissue was placed in a falcon with pre-cooled PBS on ice for immediate further processing. Another tumor sample was transferred into 4% PFA on ice for 4 h in preparation for cryo-conservation for immunofluorescence stainings. Small samples of tumor tissue were snap-frozen and stored at -80° for DNA, RNA and protein isolation. All other organs, including the remaining tumor, pancreas, spleen, liver, lung, heart, stomach, intestine and kidneys, were assessed for visible metastases and fixed in 4% PFA for histological analysis.

2.2.2 Histology and immunohistochemistry

2.2.2.1 Paraffin sections

After overnight fixation in 4% PFA, pancreatic tumors were embedded in paraffin. For histology and immunohistochemistry stainings, paraffin-embedded tumors were cut into 1 µm serial sections using a microtome and transferred onto slides which were stored at RT until further processing.

2.2.2.2 Hematoxylin and Eosin (H&E) staining

For deparaffinization, sections were incubated in Roti® Histol (2 x 5 min), followed by rehydration in a descending ethanol series (2 x 99%, 2 x 96% and 2 x 80% for 3 min each) and washing with distilled H_2O for 2 min. Sections were then placed into hematoxylin for 5 s and a subsequent bluing step was performed by bathing slides in running tap water for around 5 min. Afterwards slides were stained with eosin for 20 s. They were then washed in distilled H_2O, moved into an ascending ethanol series for dehydration (2 x 80%, 2 x 96% and 2 x 99% for 3 min each) and incubated in Roti® Histol (2 x 5 min) before they were covered with mounting medium.

2.2.2.3 Analysis of H&E stainings

Stained slides were photographed using the Leica Aperio VERSA 8 Digital Pathology Scanner and bright-field images were processed by Leica Aperio ImageScope and Fiji. Based on analysis of at least two sections per mouse, tumors were assigned a predominantly glandular (conventional or papillary) or non-glandular (mesenchymal) morphology according to the classification suggested by Kalimuthu et al. (2020). Grading of PDAC was also assessed on three tumor sections per mouse and verified by board-certified pathologist Prof. Dr. med. Moritz Jesinghaus (Universitätsklinikum Gießen und Marburg). The following grading system was used as recommended by the American Joint Committee on Cancer: G1, G2, G3 or G4 for well-differentiated, moderately differentiated, poorly differentiated and undifferentiated tumor cells, respectively.

2.2.3 Immunophenotyping via multi-color flow cytometry

For flow cytometry, a piece of tumor tissue obtained during mouse dissection was transferred into a Petri dish and thoroughly minced with a scalpel. The sample was then moved into a tube containing 2.35 ml of DMEM, 12.5 µl of enzyme A, 100 µl of enzyme D and 50 µl of enzyme R from a tumor dissociation kit and digestion was performed at 37°C for 40 min using a gentleMACS™ octo dissociator with heaters. All following washing, centrifuging and staining steps were carried out at 4°C. After centrifugation of the suspension at 1500 rpm for 5 min and

removal of the supernatant, the pellet was resuspended in 5 ml of cold PBS + 2% FCS and passed through a 70 µm cell strainer. Tube and mesh were washed with additional 5 ml of cold PBS + 2% FCS. Two more rounds of centrifugation at 1500 rpm for 5 min each, removal of supernatant and resuspension were completed by dissolution of the pellet in 200 µl of cold PBS and counting of the cells in a 1:1 dilution with trypan blue using a hemocytometer. A dilution of 2.000.000 cells in 300 µl of PBS was prepared and stained for 10 min with 1:500 Zombie Aqua to discriminate live and dead cells. To prevent unspecific Fc binding causing false positive staining, blocking with 1 µl of anti-mouse Fc receptor blocking solution (1:300) was performed for another 10 min. Afterwards 700 µl of cold PBS + 2% FCS were added and cells were divided into two separate tubes containing 1.000.000 each, for staining with a T and B cell panel and an innate immune cell panel, respectively. Details of the staining panels including antibody targets, conjugated dyes and concentrations can be found in Table 1, Table 5 and Table 6. Staining with 100 µl of the corresponding antibody master mix was performed after centrifugation at 1500 rpm for 5 min and removal of supernatant. After 30 min, the staining process was stopped by adding 1 ml of cold PBS + 2% FCS to each tube and samples were centrifuged at 1500 rpm for 5 min. After a washing step, pellets were resuspended in 200 µl of cold PBS and passed through a 30 µm cell strainer into a glass tube. Samples were analyzed with the BD LSRFortessa™, with up to 1.000.000 events recorded per panel. Analysis of flow cytometry data was performed using FlowJo software version 10.6.2. Gating strategies are shown in Figure 2.

Target	**Antigen**	**Fluorophore**	**Laser**
Helper T cells	CD4	BUV805	355 nm
T cells	CD3ε	BUV395	
Cytotoxic T cells	CD8	BV785	405 nm
Regulatory T cells	CD25	BV650	
γ/δ T cells	TCRγ/δ	BV421	
Leukocytes	CD45	PerCP Cy5.5	488 nm
B cells	CD19	FITC	
Naive central memory T cells	CD62L	PE	561 nm
Effector memory T cells	CD44	APC/Cyanine7	640 nm
Epithelial cells	EpCAM	AF647	

Table 5: Adaptive immune cell staining panel for flow cytometry experiments
Dead cells were identified with Zombie Aqua (excited by 405 nm laser; peak emission at 516 nm, similar to BV510).

Target	Antigen	Fluorophore	Laser
Dendritic cells	CD11c	BUV805	355 nm
NK cells	NK1.1	BUV395	
Classical inflammatory macrophages	Ly6C	BV785	405 nm
Myeloid cells	CD11b	BV650	
Macrophages	F4/80	BV421	
Leukocytes	CD45	PerCP Cy5.5	488 nm
Eosinophils	Siglec-F	FITC	
Neutrophils	Ly6G	PE	561 nm
Monocytes and macrophages	CD68	APC/Cyanine7	640 nm
Epithelial cells	EpCAM	AF647	

Table 6: Innate immune cell staining panel for flow cytometry experiments
Dead cells were identified with Zombie Aqua (excited by 405 nm laser; peak emission at 516 nm, similar to BV510).

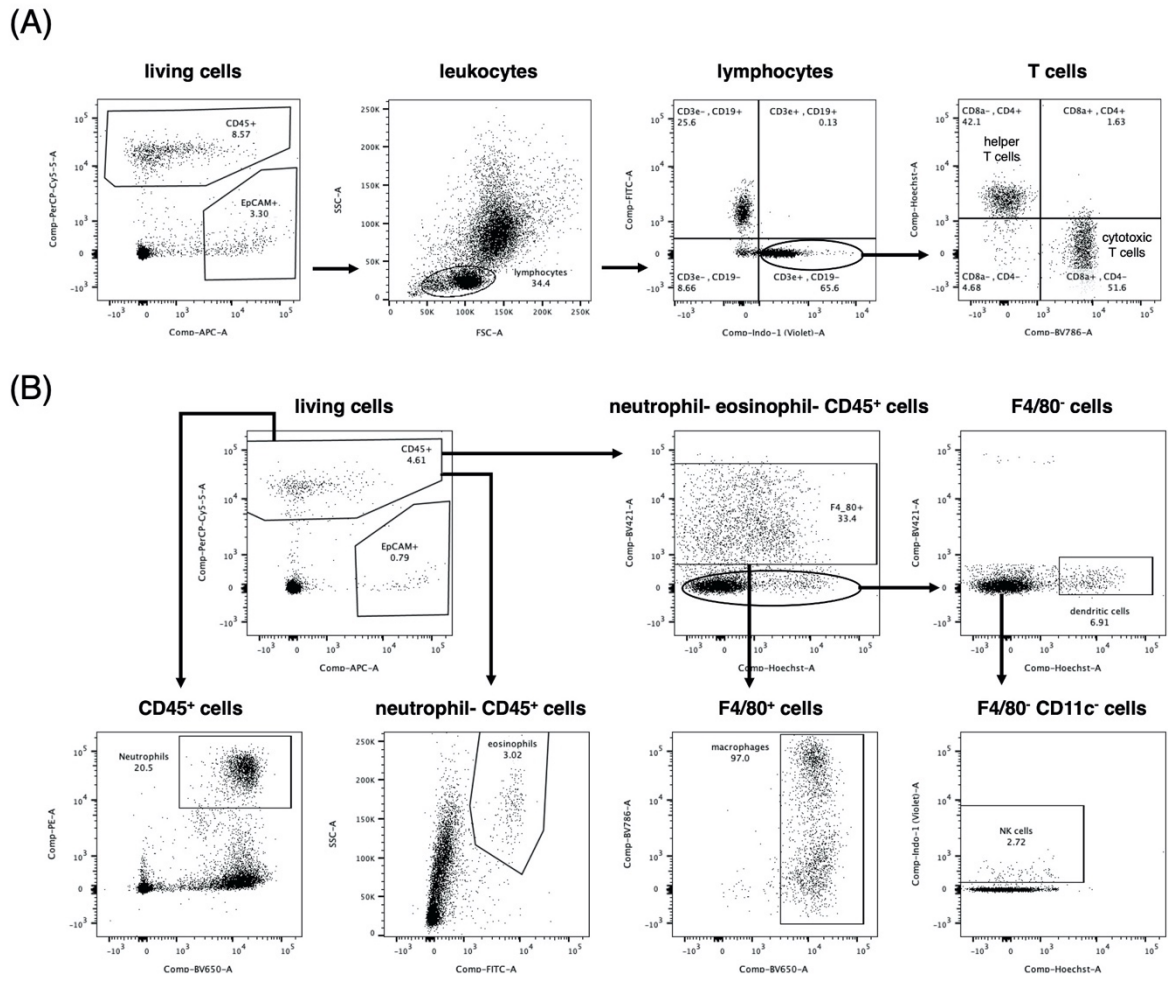

Figure 2: Gating strategies for flow cytometry analyses
(A) Gating strategy for the adaptive immune cell panel. (B) Gating strategy for the innate immune cell panel.

2.2.4 Immunophenotyping via multiplex immunofluorescence staining

2.2.4.1 Tissue preparation

PFA-fixed tumors were rinsed with PBS and transferred for cryoprotection into 15% sucrose in PBS at 4°C. Once the tissue had sunk, it was moved to 30% sucrose in PBS at 4°C. After allowing the tissue to sink overnight, excess liquid was removed. Samples were embedded in optimal cutting temperature (O.C.T) medium, frozen on dry ice and stored at -80°C. For immunofluorescence stainings, PFA-fixed O.C.T-embedded tumors were cut with a cryostat into 5 µm serial sections and transferred onto glass slides which were stored at -80°C.

2.2.4.2 Multiplex immunofluorescence staining

Slides were thawed on a hot plate for 1 min and air dried for 30 min, followed by fixation with acetone at 4°C for 6 min. After removal of excess acetone, slides were rehydrated in PBS for 10 min at RT. Tissues then underwent blocking with 10% donkey serum and 10% goat serum in PBS for 1 hour in a humid chamber at RT. The blocking solution was removed, and slides were incubated for 3 hours in a humid chamber at RT with the primary antibody, either diluted in 3% bovine serum albumin (BSA) in PBS or in 0,5% Triton in 0,5% BSA in PBS. Concentrations of primary antibodies can be found in Table 2. Slides were washed 3 x 5 min in PBS and incubated for 1 hour in a humid chamber at RT with a fluorescence-labelled secondary antibody diluted 1:200 in 3% BSA in PBS. Staining steps were repeated for each primary and secondary antibody. When two primary rabbit antibodies were used consecutively, a blocking step with 10% rabbit serum in PBS was performed between first secondary and second primary antibody. Nuclear staining was performed with DAPI (diluted 1:500) or TO-PRO-3 (diluted 1:10.000) for 10 min depending on the staining panel. After three more washing steps in PBS, slides were mounted using Vectashield® Antifade Mounting Medium and sealed with a glass cover slip. The stained tissue sections were kept at 4°C until imaging. Details on the immunofluorescence staining panels which were established and optimized in this project can be found in Figure 3, 4 and 5.

(A)

Antibody (Concentration)	Target	Fluorophore
Anti-CD3 (1:50)	T cells	AF488
Anti-CD45R/B220 (1:50)	B cells	AF594
Anti-CD31 (1:400)	Endothelial cells	Cy3
Anti-CK18 (1:5000)	Tumor cells	AF680
(1:500)	DNA (Nucleus)	DAPI

(B)

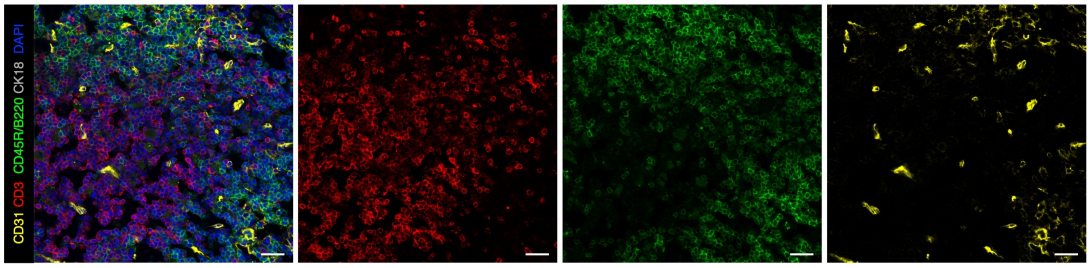

(C)

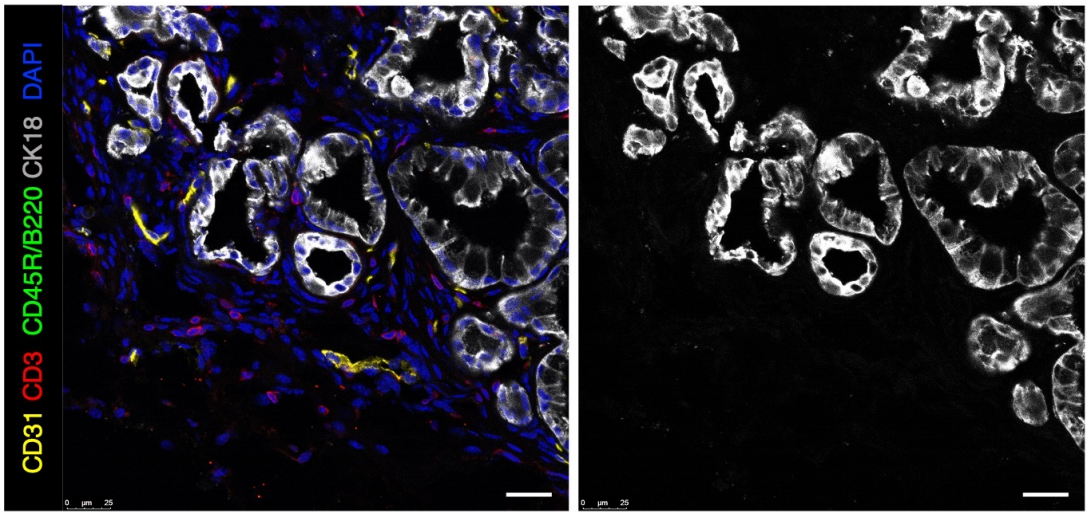

Figure 3: Optimization of a multiplex immunofluorescence staining panel detecting lymphocytes, blood vessels and tumor cells in endogenous mPDAC
(A) Overview of the lymphocyte staining panel. (B) Representative images of immunofluorescence stainings showing CD3⁺ T cells (red), CD45R/B220⁺ B cells (green) and CD31⁺ endothelial cells (yellow) in a section of a murine spleen used as a positive control for optimization of the lymphocyte staining panel. Scale bars 25 µm. (C) Representative images of immunofluorescence-stained tumor sections showing gland-forming CK18⁺ tumor cells (white) in classical endogenous *Kras*^{G12D}-driven mPDAC. Scale bars 25 µm.

(A)

Antibody (Concentration)	Target	Fluorophore
Anti-CD3 (1:50)	T cells	AF594
Anti-CD4 (1:50)	Helper T cells	AF532
Anti-CD8a (1:50)	Cytotoxic T cells	AF488
Anti-FOXP3 (1:50)	Regulatory T cells	eFluor 450
Anti-CK18 (1:5000)	Tumor cells	AF680
(1:10000)	DNA (Nucleus)	TO-PRO-3

(B)

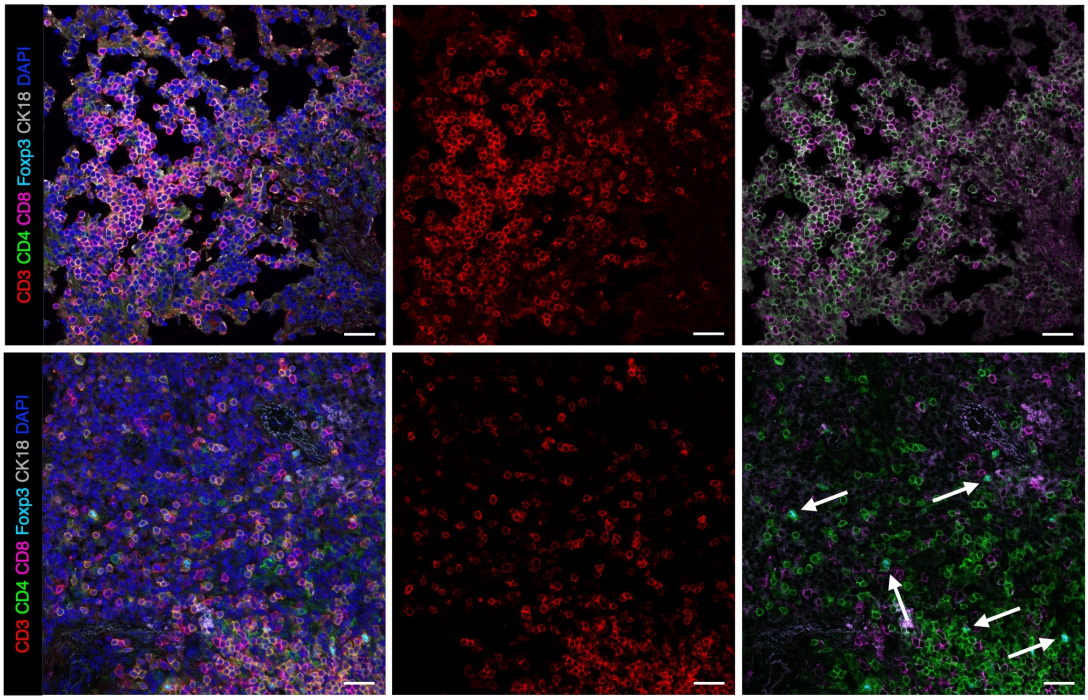

Figure 4: Optimization of a multiplex immunofluorescence staining panel detecting T cell subpopulations and tumor cells in endogenous mPDAC
(A) Overview of the T cell subpopulations staining panel. For representative images of stained tumor sections, see Figure 8. (B) Representative images of immunofluorescence stainings showing $CD8^+$ cytotoxic T cells (magenta), $CD4^+$ $FOXP3^-$ helper T cells (green) and $CD4^+$ $FOXP3^+$ regulatory T cells (green and cyan, marked with white arrows) as subpopulations of $CD3^+$ T cells (red) in two sections of a murine spleen used as a positive control for optimization of the T cell subpopulations staining panel. Scale bars 25 µm.

(A)

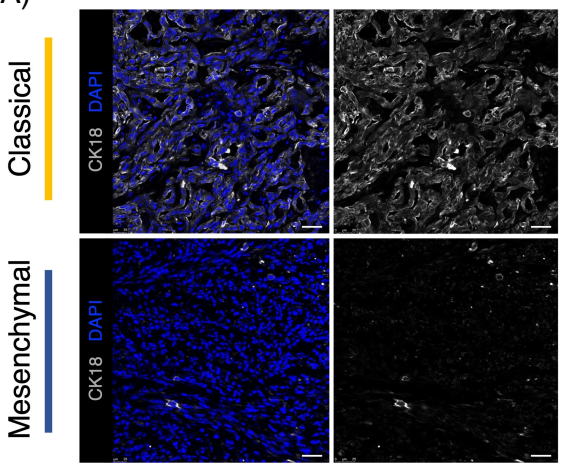

(B)

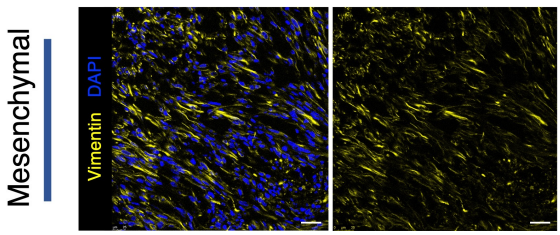

(C)

Antibody (Concentration)	Target	Fluorophore
Anti-CD3 (1:50)	T cells	AF488
Anti-CD45R/B220 (1:50)	B cells	AF594
Anti-CD31 (1:400)	Endothelial cells	Cy3
Anti-CK18 (1:5000) / Anti-Vimentin (1:1000)	Tumor cells classical / mesenchymal	AF680
(1:500)	DNA (Nucleus)	DAPI

(D)

Antibody (Concentration)	Target	Fluorophore
Anti-CD3 (1:50)	T cells	AF594
Anti-CD4 (1:50)	Helper T cells	AF532
Anti-CD8a (1:50)	Cytotoxic T cells	AF488
Anti-FOXP3 (1:50)	Regulatory T cells	eFluor 450
Anti-CK18 (1:5000) / Anti-Vimentin (1:1000)	Tumor cells classical / mesenchymal	AF680
(1:10000)	DNA (Nucleus)	TO-PRO-3

(E)

Antibody (Concentration)	Target	Fluorophore
Anti-CD31 (1:400)	Endothelial cells	Cy3
Anti-αSMA (1:100) Anti-P-selectin (1:200)	Vascular smooth-muscle cells, myofibroblasts Activated endothelial cells, Weibel-Palade bodies	AF488
Anti-CK18 (1:5000) / Anti-Vimentin (1:1000)	Tumor cells classical / mesenchymal	AF680
(1:500)	DNA (Nucleus)	DAPI

Figure 5: Modified multiplex immunofluorescence staining panels optimized for the use on tumors derived from orthotopic transplantation
(A), (B) Representative images of immunofluorescence stainings for CK18$^+$ PDAC cells (white) of sections from classical (left) and mesenchymal (right) tumors derived from orthotopic transplantation (A). In the mesenchymal subtype, CK18 expression was very weak. The mesenchymal marker vimentin (yellow) was therefore used for immunofluorescence staining of tumors derived from orthotopic transplantation of mesenchymal tumor cells (B). (C) Overview of the modified lymphocyte staining panel. For representative images, see Figure 10. (D) Overview of the modified T cell subpopulations staining panel. For representative images, see Figure 12. (E) Overview of the vascular staining panels. These multiplex immunofluorescence panels were established and optimized to assess combinatorial treatment-induced blood vessel maturation (α-SMA) and endothelial cell activation (P-selectin) in tumors derived from orthotopic transplantation of mPDAC cells. For representative images, see Figure 14.

2.2.4.3 Imaging and quantification

Acquisition of images was performed with a Leica TCS SP8 Confocal Laser Scanning Microscope with a 40x objective and 10x ocular. The laser settings are specified in Table 7. Leica Application Suite X and Fiji ImageJ2 were used to process and analyze images. Abundance of cells was assessed by counting DAPI- or TO-PRO-3-positive nuclei manually using the Fiji Cell Counter plugin. DAPI or TO-PRO-3 channels were then merged with antibody channels for quantification of specific antibody signals. DAPI$^+$ (or TO-PRO-3$^+$) cells with CD3 or CD45R/B220 membrane staining were counted for quantification of T and B cells, respectively. For quantification of CD8$^+$ cytotoxic T cells, only TO-PRO-3$^+$ cells with both CD3 and CD8 membrane staining were counted. Quantification of CD4$^+$ FOXP3$^-$ helper T cells was performed in a similar way, with only TO-PRO-3$^+$ cells with both CD3 and CD4 membrane staining and no nuclear FOXP3 signal being counted. For quantification of CD4$^+$ FOXP3$^+$ regulatory T cells, only TO-PRO-3$^+$ cells with CD3 and CD4 membrane staining and additional

nuclear FOXP3 staining were considered. Vessels with open lumina were quantified as fractions of all CD31$^+$ vessels. For quantification of α-SMA$^+$ and P-selectin$^+$ vessels, the numbers of all CD31$^+$ blood vessels and of those with surrounding α-SMA$^+$ pericytes respective luminal P-selectin expression were determined. For all quantifications, 10 random fields of view of 3 to 5 individual tumors per subtype and / or treatment condition were analyzed in a blinded manner.

Fluorophore		DAPI	AF488	Cy3	AF594	AF680
Laser	Peak excitation	359 (UV 405 laser)	499	552	590	681
	Peak emission	461	520	578	617	704
Detector		PMT	HyD			

Fluorophore		eFluor450	AF488	AF532	AF594	ToPro3	AF680
Laser	Peak excitation	405 (UV 405 laser)	499	534	590	642	681
	Peak emission	450	520	553	617	661	704
Detector		HyD				PMT	HyD

Table 7: Confocal settings for acquisition of fluorescent signals
The upper table shows the settings for multiplex immunofluorescence staining panels specified in Figure Figure 3(A), Figure 5(C) and Figure 5 (E), the lower table shows the settings for panels specified in Figure 4(A) and Figure 5 (D).

2.2.5 Statistical analysis

Data analysis and graphical representations were performed with the software GraphPad Prism. n = 3 – 24 mice were included in the control and experimental groups as noted in the corresponding figures. Results are displayed individually and as mean values ± SD. For statistical evaluation, a two-tailed Student's *t*-test with Welch's correction was employed. Resulting p values are indicated in the respective figures, with a cut off $p < 0.05$ used to define significance. Survival data of mice were compared using a Kaplan-Meier estimator and a log-rank Mantel-Cox test was performed for statical analysis.

3 Results

3.1 Characterization of adaptive immune cell infiltration and tumor vasculature in a *Kras^{G12D}*-driven GEMM of PDAC

3.1.1 Characterization of the endogenous *Kras^{G12D}*-driven mPDAC cohort

To investigate baseline adaptive immune cell infiltration in *Kras^{G12D}*-driven mPDAC, a cohort of 10 *Ptf1a$^{Cre/+}$;LSL-Kras$^{G12D/+}$* (KC) mice with conditional expression of the mutant *Kras^{G12D}* resulting in formation of invasive PDAC was analyzed (Figure 6(A)). For assessment of tumor histology, H&E staining of paraffin sections was performed, revealing great heterogeneity of PDAC morphology within the cohort. Based on the predominant morphological pattern as described by Kalimuthu et al. (2020) and pathological grading of tumor cells, individual tumors were assigned to two morphological subtypes: G1- and G2-graded PDAC with well-differentiated to moderately differentiated tumor cells demonstrating a conventional gland-forming or papillary pattern were allocated to the classical subtype (n = 5), while G3- and G4-graded PDAC with mostly non-gland forming, quasi-mesenchymal, poorly to undifferentiated tumor cells were included in the mesenchymal subtype (n = 5). As depicted by representative histopathological images of the tumors in Figure 6(B), classical tumors were further characterized by a high stromal content, while mesenchymal tumors showed sparse stroma and a high tumor cell density.

To correlate morphological subtypes with disease severity and prognosis, survival data of the animals were compared using Kaplan-Meier analysis (Figure 6(C)). Similar to findings in human PDAC (Bailey et al., 2016b), the mesenchymal subtype was associated with a more aggressive disease course as evidenced by shorter overall survival, with median survival times of 308 vs. 472 days for the mesenchymal and classical subtype, respectively. However, cohort sizes were relatively small and the difference between the two subtypes was not significant ($p = 0.14$).

3.1.2 Endogenous *Kras^{G12D}*-driven mPDAC display great intertumoral heterogeneity of adaptive immune cell infiltration

To characterize adaptive immune cell infiltration in the endogenous *Kras^{G12D}*-driven PDAC cohort described above, a multiplex immunofluorescence staining panel detecting lymphocytes, blood vessels and PDAC cells was established and optimized (see Figure 3). In Figure 6(D), representative images of immunofluorescence-stained tumor sections from classical and mesenchymal tumors are shown, illustrating differential T and B cell infiltration in the two subtypes. To quantify lymphocytes, at least 8 random fields of view at 400x magnification of n = 4 individual tumors per subtype were analyzed. Two tumors were excluded

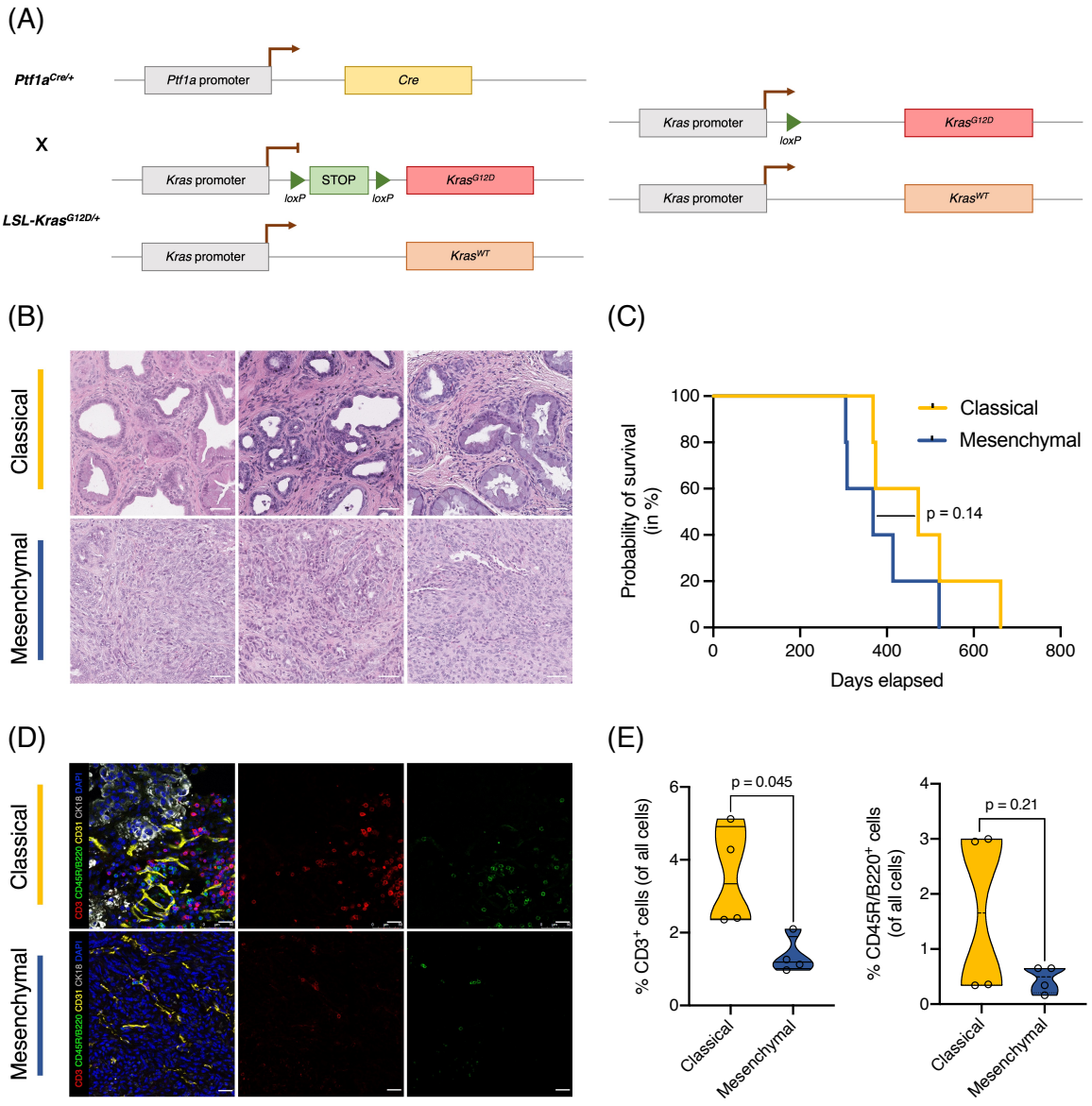

Figure 6: Endogenous *Kras*^{G12D}-driven mPDAC display great morphological and immunological heterogeneity with poor adaptive immune cell infiltration specifically in the aggressive mesenchymal subtype

(A) Schematic representation of the endogenous KC mPDAC model using the Cre-*loxP* recombinase system to enable pancreas-specific expression of oncogenic *Kras*^{G12D}. (B) Representative images of H&E stainings of tumor sections from KC tumor mice. Individual tumors were assigned to the classical or mesenchymal subtype. The classical subtype comprises PDAC presenting a conventional gland-forming or papillary pattern of well- to moderately differentiated tumor cells (G1/G2 grading), whereas PDAC with predominantly non-gland forming, poorly to undifferentiated tumor cells (G3/G4 grading) are included in the mesenchymal subtype. 3 different tumors of each condition are shown. Scale bars 50 µm. (C) Kaplan-Meier survival curves of the KC cohort. Animals were assigned to the classical and mesenchymal cohort based on morphological classification as described in (B) (n=5 for each cohort). P-value was calculated using the log-rank Mantel-Cox test. (D) Representative images of immunofluorescence stainings for CD3$^+$ T cells (red) and CD45R/B220$^+$ B cells (green) of sections from endogenous tumors of the classical (upper row) and mesenchymal (lower row) subtype. In this lymphocyte staining panel (see Figure 3), CD31 (yellow), CK18 (white) and DAPI (blue) were used to detect endothelial cells, PDAC cells and nuclei, respectively. Scale bars 25 µm. (E) Quantification of CD3$^+$ T cells (left graph) and CD45R/B220$^+$ B cells (right graph) from immunofluorescence stainings of endogenous tumors of the classical (yellow) and mesenchymal (blue) subtype as depicted in (D). Individual tumors are shown as single points in the graph (n=4 for each subtype). P-values in (E) were calculated using a two-tailed, unpaired Welch's t test.

from quantification due to mostly necrotic tissue or poor cryo-conservation of the samples resulting in unspecific immunofluorescence staining. Results are shown in Figure 6(E), revealing heterogeneity of lymphocytic infiltration among endogenous *Kras*^{G12D}-driven mPDAC. In comparison to classical tumors, a significantly lower number of infiltrating T cells was found in poorly differentiated tumors of the mesenchymal subtype ($p = 0.045$). B cell counts were uniformly low in tumors of the mesenchymal subtype, while being characterized by greater intertumoral variation in classical tumors ($p = 0.21$). When comparing both lymphocyte populations for each tumor, a significant correlation of T and B cell infiltration in KC tumors could be observed (Pearson's $r = 0.88$, $p = 0.0041$, data not shown). Overall, endogenous *Kras*^{G12D}-driven mPDAC of the mesenchymal subtype displayed particularly poor adaptive immune cell infiltration, while TIL were generally more abundant in classical tumors.

3.1.3 Adaptive immune cell infiltration also displays intratumoral heterogeneity, with higher densities of tumor-infiltrating T cells in stroma-rich regions irrespective of morphological PDAC subtypes

To gain insight into spatial distribution of lymphocytes within the tumor and their relation to tumor cells, stroma and vasculature, large scans of the stained tumor sections (multiplex immunofluorescence panel as shown in Figure 6(D)) consisting of multiple adjacent 400x magnification images were analyzed. In these scans covering large parts of whole tumor sections, lymphocyte clusters and individual TIL were identified as the two elementary patterns of adaptive immune cell infiltration in endogenous *Kras*^{G12D}-driven PDAC (Figure 7(A)-(C)).

In both classical and mesenchymal tumors, clusters of T and B cells were found in regions with high stromal content and low tumor cell density (Figure 7(A)). Lymphocyte clusters with differences in B cell abundance and level of internal organization could be observed (Figure 7(B)). Only in two tumors of the classical subtype, dense B cell clusters with a narrow zone of surrounding T cells resembling TLS were detected (Figure 7(B), left panel). Other types of lymphocyte clusters included mixed conglomerates of T and B cells lacking higher spatial organization (Figure 7(B), middle panel) as well as T cell clusters without any B cells (Figure 7(B), right panel). To compare occurrence of mixed lymphocyte clusters in tumors of the classical and mesenchymal subtype, the number of all clusters with ≥ 20 $CD3^+$ T cells and ≥ 2 $CD45R/B220^+$ B cells was determined for each tumor and divided by the area of the respective tumor section. Overall, the number of lymphocyte clusters per mm^2 tended to be higher in classical tumors (mean ± SD = 1.07 ± 0.56) than in the mesenchymal subtype (0.21 ± 0.27) (Figure 7(D)). However, intertumoral heterogeneity was relatively large, especially within the

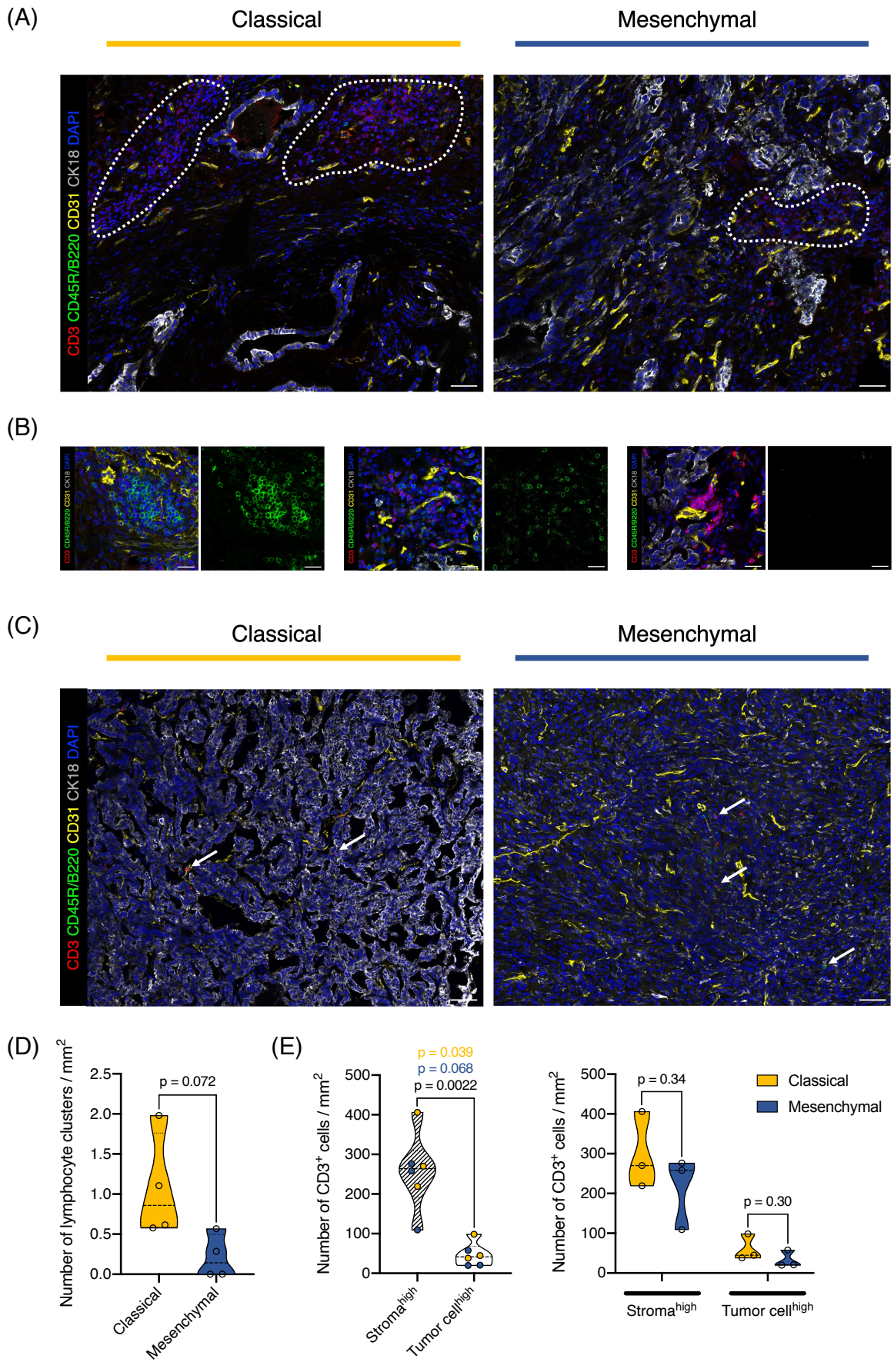

Figure 7: Patterns of adaptive immune cell infiltration differ between tumor regions with high stromal content and high tumor cell density in endogenous *Kras^{G12D}*-driven mPDAC

(A) Representative images of immunofluorescence stainings showing clusters of lymphocytes (marked with white dotted lines) in the stroma of endogenous tumors of the classical (left) and mesenchymal (right) subtype. The staining panel corresponds to the lymphocyte staining panel used in Figure 6(D). The images are details of large scans of the tumor sections composed of individual images acquired at 400x magnification. Scale bars 50 µm. (B) Representative images of immunofluorescence stainings showing different types of lymphocyte clusters as depicted in (A) at higher magnification. Lymphocyte clusters are categorized based on CD45R/B220$^+$ B cell (green) abundance and organization. Left: TLS-like cluster of B cells surrounded by few T cells. Middle: conglomerate of scattered T and B cells. Right: cluster of T cells with absence of B cells. Scale bars 25 µm. (C) Representative images of immunofluorescence stainings showing individual TIL (marked with white arrows) in stroma-poor regions of endogenous tumors of the classical (left) and mesenchymal (right) subtype. The staining panel corresponds to (A). The images are details of large scans of the tumor sections composed of individual images acquired at 400x magnification. Scale bars 50 µm. (D) Quantification of lymphocyte clusters from immunofluorescence stainings of endogenous tumors of the classical (yellow) and mesenchymal (blue) subtype as depicted in (A) and (B). Lymphocyte clusters were defined as clusters with ≥ 20 CD3$^+$ cells and ≥ 2 CD45R/B220$^+$ B cells. Individual tumors are shown as single points in the graph (n=4 for each subtype). (E) Quantification of CD3$^+$ T cells in regions with high (stroma^{high}, hatched) and low (tumor cell^{high}, white) stromal content from immunofluorescence stainings of endogenous tumors as depicted in (A) and (C). Results for all tumors, including individual tumors of the classical (yellow dots) and mesenchymal (blue dots) subtype, are shown in the left graph. P-values are calculated for all tumors irrespective of the subtype (black), only classical tumors (yellow) and only mesenchymal tumors (blue). In the right graph, results for stroma^{high} and tumor cell^{high} tumor regions are compared between classical (yellow) and mesenchymal (blue) tumors (n=3 for each subtype). P-values in (D) and (E) were calculated using a two-tailed, unpaired Welch's t test.

---

classical subtype, and the difference between classical and mesenchymal tumors was not significant ($p = 0.072$). Individual T and B cells were present in all tumors, constituting the second pattern of adaptive immune cell infiltration. Unlike lymphocyte clusters, individual TIL could also be detected in stroma-poor regions with high tumor cellularity (Figure 7 (C)).

To further assess intratumoral heterogeneity of T cell infiltration, two distinct regions of interest (ROI) were defined for each tumor scan, one comprising an area with high stromal content and low density of tumor cells (stroma^{high}) and one including a stroma-poor area with high tumor cell density (tumor cell^{high}). Tumor infiltrating T cells (clustered or individual) were then quantified separately for stroma^{high} and tumor cell^{high} areas by dividing absolute CD3$^+$ T cell counts by respective ROI area in mm^2. One classical and one mesenchymal tumor were excluded from the analysis as no tumor cell^{high} or stroma^{high} ROI of sufficient size, respectively, could be defined in the corresponding scan of the tumor section. As depicted in Figure 7(E) (left graph), the number of T cells per mm^2 was significantly higher in stroma^{high} than in tumor cell^{high} areas for all tumors analyzed ($p = 0.0022$). This was also observed when analyzing both subtypes individually, although the differences between stroma^{high} and tumor cell^{high} T cell counts appeared to be slightly more pronounced in the classical subtype. Results were statistically significant for classical ($p = 0.039$), but not for mesenchymal tumors ($p = 0.068$). Interestingly, T cell counts did not significantly differ between the classical and mesenchymal subtype when analyzing stroma^{high} and tumor cell^{high} ROI separately (Figure 7(E), right graph),

suggesting that the higher stromal content of classical tumors mainly contributed to the significantly stronger overall T cell infiltration as depicted in Figure 6(E).

To sum up, spatial distribution patterns of TIL were closely related to stromal content and tumor cellularity of endogenous *Kras*^{G12D}-driven mPDAC, with a relative abundance of lymphocyte clusters and tumor-infiltrating T cells in stroma-rich tumor regions irrespective of morphological PDAC subtypes, thus reflecting intratumoral heterogeneity of adaptive immune cell infiltration.

3.1.4 Mesenchymal PDAC are characterized by poor cytotoxic T cell infiltration and relative abundance of helper and regulatory T cells particularly within areas of high tumor cellularity

For a more comprehensive analysis of T cell-mediated immune responses in different morphological subtypes of endogenous *Kras*^{G12D}-driven PDAC, a second multiplex immunofluorescence panel detecting cytotoxic T cells, helper T cells, regulatory T cells and tumor cells was established and optimized (Figure 4). Representative images are shown in Figure 8 (A). For quantification of T cell subpopulations, 8-10 random fields of view at 400x magnification of n = 3 individual tumors of the classical subtype and n = 4 tumors of the mesenchymal subtype were analyzed. Three tumors were excluded from quantification due to mostly necrotic tissue or poor cryo-conservation of the sample resulting in unspecific immunofluorescence staining. As depicted in Figure 8(B) (left graph), CD8$^+$ cytotoxic T cell infiltration was significantly lower in tumors of the mesenchymal subtype than in classical tumors ($p = 0.015$). While infiltration of CD4$^+$ helper and regulatory T cells was also relatively low in tumors of the mesenchymal subtype, greater intertumoral variability was found for the classical subtype (Figure 8(B), middle). However, of these CD4$^+$ cells, the fraction of FOXP3$^+$ regulatory T cells was significantly higher in mesenchymal tumors ($p = 0.021$) (Figure 8(B), right), indicating a predominance of tumor-infiltrating T cells with an immunosuppressive phenotype in this PDAC subtype.

To gain additional information on fractions of T cell subpopulations, the proportion of CD8$^+$ and CD4$^+$ T cells among all CD3$^+$ T cells was determined and CD8$^+$:CD4$^+$ ratios were calculated for each tumor (Figure 8(C)). In tumors of the classical subtype, fractions of CD8$^+$ and CD4$^+$ were characterized by great intertumoral heterogeneity as evidenced by a mean CD8$^+$:CD4$^+$ ratio ± SD of 0.85 ± 0.66. In contrast, tumors of the mesenchymal subtype were characterized by very low fractions of CD8$^+$ (mean % of CD3$^+$ T cells ± SD = 22.5% ± 3.7%) and a relative abundance of CD4$^+$ T cells (mean % of CD3$^+$ T cells ± SD = 72.7% ± 5.7%), resulting in a mean CD8$^+$:CD4$^+$ ratio ± SD of 0.31 ± 0.07 highlighting the relative lack of cytotoxic T cells in mesenchymal PDAC.

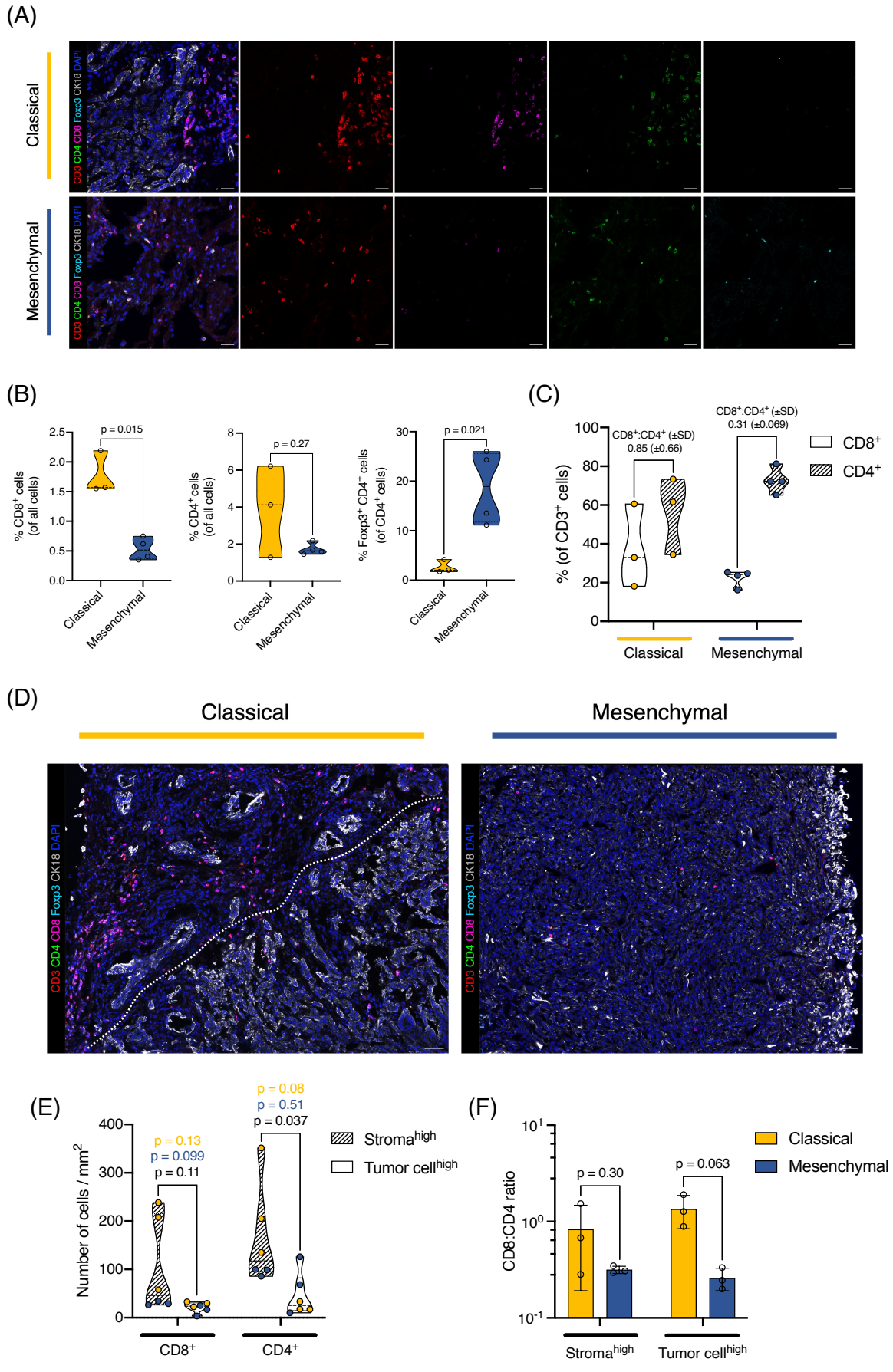

Figure 8: Analysis of T cell subsets reveals poor infiltration of CD8+ cytotoxic T cells specifically in the mesenchymal subtype of endogenous *Kras^{G12D}*-driven mPDAC

(A) Representative images of immunofluorescence stainings for $CD8^+$ cytotoxic T cells (magenta), $CD4^+$ $FOXP3^-$ helper T cells (green) and $CD4^+$ $FOXP3^+$ regulatory T cells (cyan) of sections from endogenous tumors of the classical (upper row) and mesenchymal (lower row) subtype. In this T cell subpopulations staining panel (see Figure 4), CD3 (red), CK18 (white) and TO-PRO-3 (blue) were used to detect T cells, PDAC cells, and nuclei, respectively. Scale bars, 25 µm. (B) Quantifications of $CD8^+$ cytotoxic T cells (left), $CD4^+$ helper and regulatory T cells (middle) and $CD4^+FOXP3^+$ regulatory T cells (right) from immunofluorescence stainings of sections from endogenous tumors of the classical and mesenchymal subtype as depicted in (A). Results for $CD8^+$ and $CD4^+$ T cells are displayed as fractions of all cells, while results for $CD4^+FOXP3^+$ regulatory T cells are shown as fractions of $CD4^+$ T cells. Individual tumors are shown as single points in the graphs (n=3 for the classical subtype and n=4 for the mesenchymal subtype). (C) $CD8^+$ cytotoxic T cells and $CD4^+$ helper and regulatory T cells from (B) displayed as fractions of all $CD3^+$ T cells. A $CD8^+$:$CD4^+$ ratio was calculated for each tumor and the mean ratio ± SD for the classical and mesenchymal subtype are indicated in the graph. (D) Representative images of immunofluorescence stainings showing intratumoral heterogeneity of $CD8^+$ cytotoxic T cell infiltration in an endogenous tumor of the classical subtype (left, border between $stroma^{high}$ and tumor $cell^{high}$ areas marked with a white dotted line) and weak $CD8^+$ cytotoxic T cell infiltration in a tumor $cell^{high}$ area of an endogenous tumor of the mesenchymal subtype (right). The staining panel corresponds to (A). The images are details of large scans of the tumor sections composed of individual images acquired at 400x magnification. Scale bars, 50 µm. (E) Quantification of $CD8^+$ and $CD4^+$ T cells in $stroma^{high}$ (hatched) and tumor $cell^{high}$ (white) regions from immunofluorescence stainings of endogenous tumors as depicted in (D). Individual tumors of the classical (yellow dots) and mesenchymal (blue dots) subtype are shown as single points (n=3 for each subtype). P-values are calculated for all tumors irrespective of the subtype (black), only classical tumors (yellow) and only mesenchymal tumors (blue). (F) Comparison of $CD8^+$:$CD4^+$ ratios from quantifications in (E) between tumors of the classical and mesenchymal subtype in $stroma^{high}$ and tumor $cell^{high}$ regions. Mean ratios ± SD are depicted for each subtype and individual tumors are shown as single points (n=3 for each subtype). P-values in (B), (C), (E) and (F) were calculated using a two-tailed, unpaired Welch's t test.

To investigate intratumoral heterogeneity of T cell subpopulations and their relation to stromal content and tumor cell density, large scans of the tumor sections stained with the multiplex immunofluorescence panel for T cell subpopulations (as shown in Figure 8(A)) were analyzed. Representative image sections of scans from a classical and mesenchymal tumor, respectively, are shown in Figure 8(D). In some classical tumors, not only heterogeneity of T cell infiltration but also co-existence of different morphological patterns could be observed (Figure 8(D), left). While $CD8^+$ cytotoxic T cells were clustering in areas with high stromal content and low density of gland forming tumor cells (left side of the white dotted line), only few $CD8^+$ cytotoxic T cells were found within areas of high tumor cell density characterized by a papillary pattern and low stromal content (right side of the white dotted line). Mesenchymal tumors mostly presented a relatively homogenous appearance with high tumor cell density and sparse infiltration of individual $CD8^+$ cytotoxic T cells (Figure 8(D), right).

To account for this intratumoral heterogeneity, $stroma^{high}$ and tumor $cell^{high}$ ROI were defined for each tumor scan analogously to Figure 7. Tumor infiltrating $CD8^+$ and $CD4^+$ T cells were then quantified separately for $stroma^{high}$ and tumor $cell^{high}$ areas by dividing absolute $CD8^+$ and $CD4^+$ T cell counts by respective ROI area in mm^2. One mesenchymal tumor was excluded from the analysis as no $stroma^{high}$ ROI of sufficient size could be defined in the corresponding

scan of the tumor section. Similar to total CD3$^+$ T cell counts (see Figure 7(D)), the number of CD8$^+$ and CD4$^+$ T cells per mm^2 was generally higher in stroma^{high} than in tumor cell^{high} regions when analyzing all tumors irrespective of morphological subtype (Figure 8(E)). While the difference was not significant for CD8$^+$ cytotoxic T cells ($p = 0.11$), statistical significance was seen for CD4$^+$ T cells ($p = 0.037$). However, when tumors of the classical and mesenchymal subtype were analyzed separately, higher CD4$^+$ T cell counts in stroma^{high} regions could only be observed in the classical subtype ($p = 0.08$), while there was no difference in CD4$^+$ T cell infiltration between stroma^{high} and tumor cell^{high} regions in mesenchymal tumors. The number of CD8$^+$ cytotoxic T cells per mm^2 tended to be higher in stroma^{high} regions in both classical and mesenchymal tumors, but results were not statistically significant ($p = 0.13$ and $p = 0.099$, respectively).

CD8$^+$:CD4$^+$ ratios were then calculated in stroma^{high} and tumor cell^{high} regions of each tumor and compared between the classical and mesenchymal subtype as depicted in Figure 8(F). In stroma^{high} regions, CD8$^+$:CD4$^+$ ratios did not differ significantly between classical and mesenchymal tumors. While the mean CD8$^+$:CD4$^+$ ratio ± SD was 0.32 ± 0.02 in stroma^{high} regions of the mesenchymal subtype, great intratumoral heterogeneity was found in the classical subtype (mean CD8$^+$:CD4$^+$ ratio ± SD = 0.83 ± 0.52), matching results shown in Figure 8(C). In contrast, CD8$^+$:CD4$^+$ ratios in tumor cell^{high} regions were lower in the mesenchymal subtype (mean ± SD = 0.26 ± 0.06) than in the classical subtype (mean ± SD = 1.35 ± 0.42), although statistical significance was not quite reached ($p = 0.063$).

Taken together, mesenchymal *Kras*^{G12D}-driven mPDAC displayed both an absolute and relative lack of CD8$^+$ cytotoxic T cells, especially of those infiltrating regions of high tumor cellularity which are abundant in tumors of this subtype.

3.1.5 Endogenous *Kras*^{G12D}-driven mPDAC display different morphologies of tumor vasculature and co-localization of blood vessels with tumor-infiltrating T cells

To investigate architectural and functional features of the tumor vasculature in endogenous *Kras*^{G12D}-driven mPDAC, the tumor sections stained with the multiplex immunofluorescence panel detecting lymphocytes, blood vessels and PDAC cells (Figure 6 and Figure 7) were analyzed again, focusing now on vascular morphology. Representative images of immunofluorescence-stained tumor sections from classical and mesenchymal tumors with CD31$^+$ blood vessels (yellow) are shown in Figure 9(A). In both subtypes, tumor blood vessels appeared to be very heterogeneous in nature, with differences in diameter, length, tortuosity and, in particular, visibility of vascular lumina. While some vessels appeared collapsed (white arrowheads), others were found to have a visible lumen (white arrows, Figure 9(A)).

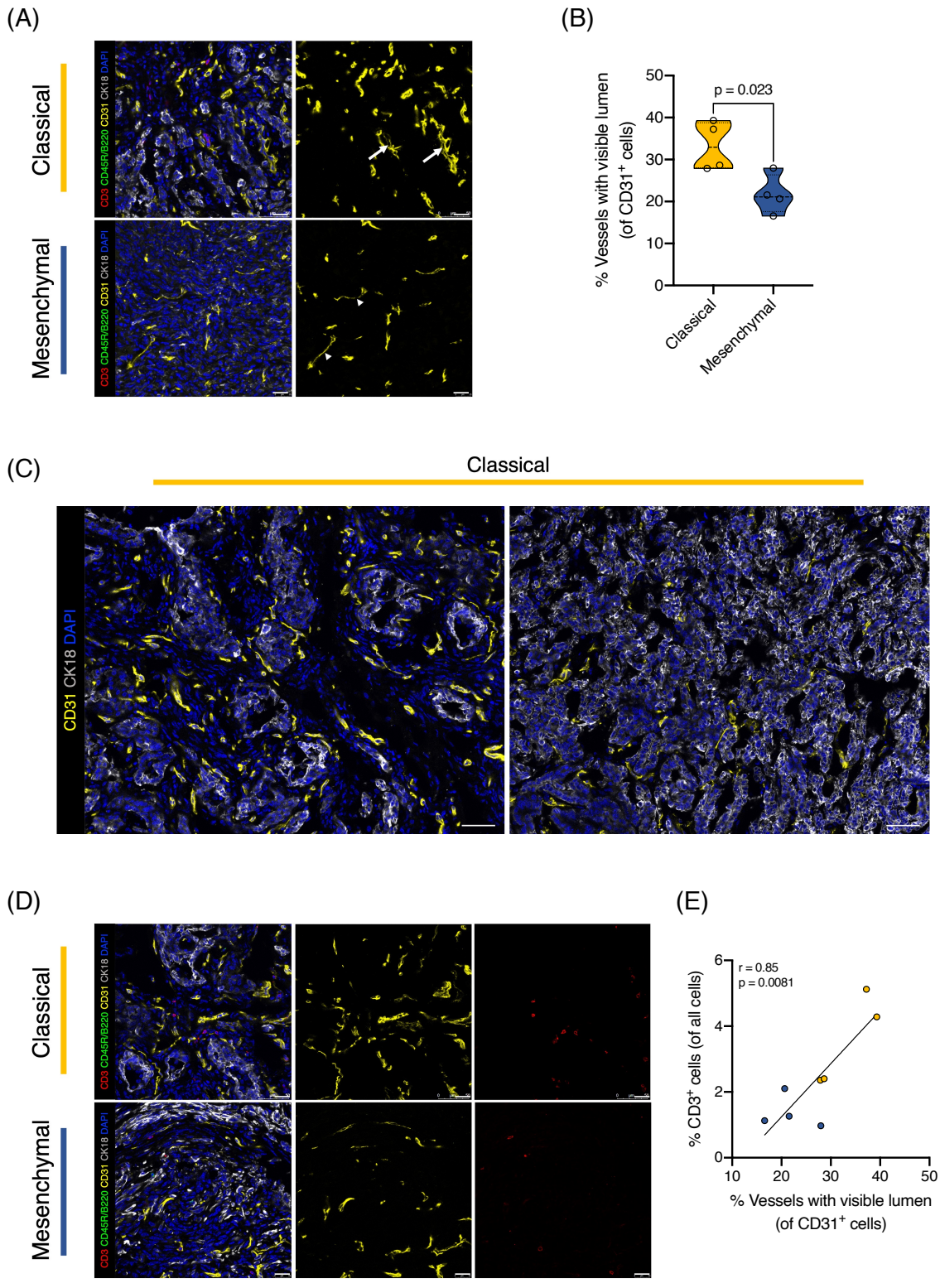

Figure 9: Patterns of tumor vasculature differ between the classical and mesenchymal subtype of endogenous *Kras*^{G12D}-driven mPDAC and blood vessels with visible lumen correlate with T cell infiltration

(A) Representative images of immunofluorescence stainings for CD31+ endothelial cells (yellow) of sections from endogenous tumors of the classical (upper row) and mesenchymal (lower row) subtype. The staining panel corresponds to the lymphocyte staining panel used in Figure 1(D). White arrows indicate vessels with visible lumen, white arrowheads indicate collapsed vessels. Scale bars 25 µm. (B) Quantification of CD31+ vessels with visible lumen from immunofluorescence stainings of sections from endogenous tumors of the classical and mesenchymal subtype as depicted in (A). Results are

shown as fractions of CD31+ cells. Individual tumors are shown as single points in the graph (n=4 for each subtype). P-value was calculated using a two-tailed, unpaired Welch's t test. (C) Representative images of immunofluorescence stainings showing intratumoral heterogeneity of tumor vasculature in two regions of an endogenous tumor of the classical subtype. The staining panel corresponds to (A). The image is a detail of a large scan composed of 54 individual images acquired at 400x magnification. Scale bars 50 µm. (D) Representative images of immunofluorescence stainings for CD31+ endothelial cells (yellow) and CD3+ T cells (red) of sections from endogenous tumors of the classical (upper row) and mesenchymal (lower row) subtype, highlighting co-localization of lymphocytes and vessels. The staining panel corresponds (A) and (C). Scale bars 25 µm. (E) Pearson's correlation analysis and simple linear regression of CD31+ vessels and CD3+ T cells as quantified in Figure 6(E) and Figure 9(B) for endogenous tumors of the classical (yellow) and mesenchymal (blue) subtype.

As compression of tumor vasculature and resulting hypoperfusion have been shown to contribute to a hypoxic TME and evasion of the immune system (Munn & Jain, 2019; Noman et al., 2015; Huang et al., 2012), subsequent analyses were focusing on blood vessels with visible lumen and their relation to TIL. To assess differences in vascular morphology between classical and mesenchymal tumors, CD31+ blood vessels with visible lumen were quantified for n = 4 individual tumors per subtype in the same fields of view which were analyzed in Figure 5(E). As depicted in Figure 9(B), tumors of the classical subtype showed a significantly higher fraction of blood vessels with visible lumen compared to tumors of the mesenchymal subtype ($p = 0.023$), with some intertumoral variability in both subtypes. However, patterns of tumor vasculature also displayed intratumoral heterogeneity, especially within one tumor of the classical subtype (Figure 9(C)). While a high density of blood vessels with visible lumen was observed in an area with stroma-surrounded conventional gland-forming tumor cells (left image), tumor vasculature was found to be sparse in an area characterized by a high density of papillary gland-forming tumor cells (right image).

Further analysis of the immunofluorescence-stained tumor sections indicated co-localization of tumor infiltrating T cells and tumor vasculature, with strong CD3+ T cell infiltration in relatively highly vascularized classical tumors and low T cell counts around mostly collapsed vessels in mesenchymal tumors (Figure 9(D)). Quantifications of CD3+ T cells (Figure 6(E)) and CD31+ blood vessels with visible lumen (Figure 9(B)) were used for correlation analysis. As depicted in Figure 9(E), the amount of CD31+ blood vessels with visible lumen significantly correlated with abundance of CD3+ T cells (Pearson's $r = 0.85$; $p = 0.0081$). Interestingly, the correlation appeared to be stronger in the classical subtype, while of the mesenchymal subtype, one tumor with a relatively high fraction of vessels with visible lumen showed the weakest T cell infiltration. Overall, endogenous *Kras*^{G12D}-driven mPDAC of the classical and mesenchymal subtype displayed different morphologies of tumor vasculature, with fewer blood vessels harboring open lumina in mesenchymal tumors, correlating with poor T cell infiltration.

3.2 Characterization of combinatorial treatment-induced adaptive immune responses and vascular remodeling in an orthotopic transplantation model of PDAC

3.2.1 The combinatorial treatment increases adaptive immune cell infiltration in tumors derived from orthotopic transplantation of *Kras^{G12D}*-driven mPDAC cells

To investigate adaptive immune responses induced by the trametinib plus nintedanib combination therapy shown to synergize *in vitro* and to prolong survival *in vivo* (see introduction, p.10), syngeneic orthotopic transplantation models of mPDAC were employed, with each one cell line derived from classical and mesenchymal KC mPDAC being transplanted as illustrated in Figure 10(A). Tumors from mice having either received one cycle of vehicle (control) or combinatorial trametinib plus nintedanib (T/N) treatment were analyzed histologically and via multiplex immunofluorescence staining as described in Figure 5. As depicted in Figure 10(B) showing representative images of the H&E-stained tumor sections, orthotopically transplanted classical and mesenchymal tumors from both control and T/N-treated animals recapitulated typical histological features of the classical and mesenchymal subtype of endogenous *Kras^{G12D}*-driven mPDAC, with gland-forming epithelial and non-gland forming mesenchymal tumor cells, respectively. However, while displaying little intertumoral heterogeneity within each morphological subtype, orthotopically transplanted tumors of both subtypes were characterized by relatively low stromal content and high tumor cellularity, contrasting with findings in endogenous *Kras^{G12D}*-driven mPDAC (see Figure 6(B)).

Immunofluorescence-stained sections of control and T/N-treated classical and mesenchymal tumors derived from orthotopic transplantation were then used to assess combinatorial treatment-induced changes in lymphocyte infiltration (Figure 10(C)). For quantification of lymphocytes, 10-12 random fields of view at 400x magnification of n = 4 individual tumors per subtype and treatment condition were analyzed. In both subtypes of control tumors derived from orthotopic transplantation, baseline B cell infiltration was very low compared to endogenous *Kras^{G12D}*-driven mPDAC (10-fold lower B cell counts in orthotopically transplanted tumors, $p = 0.059$; cf. Figure 6(E) and Figure 10(D)). Baseline T cell infiltration was lower in classical ($p = 0.017$), but not in mesenchymal tumors derived from orthotopic transplantation ($p = 0.62$) compared to endogenous *Kras^{G12D}*-driven tumors of the respective subtypes (cf. Figure 6(E) and Figure 10(D)). Furthermore, baseline T and B cell infiltrations did not correlate in orthotopically transplanted tumors (Pearson's $r = 0.35$, $p = 0.39$, data not shown).

Analysis of combinatorial treatment-induced changes in adaptive immune cell infiltration in orthotopically transplanted mPDAC revealed a significantly increased $CD3^+$ T cell infiltration ($p = 0.041$) in classical tumors upon combinatorial treatment (Figure 10(D), left), while the number

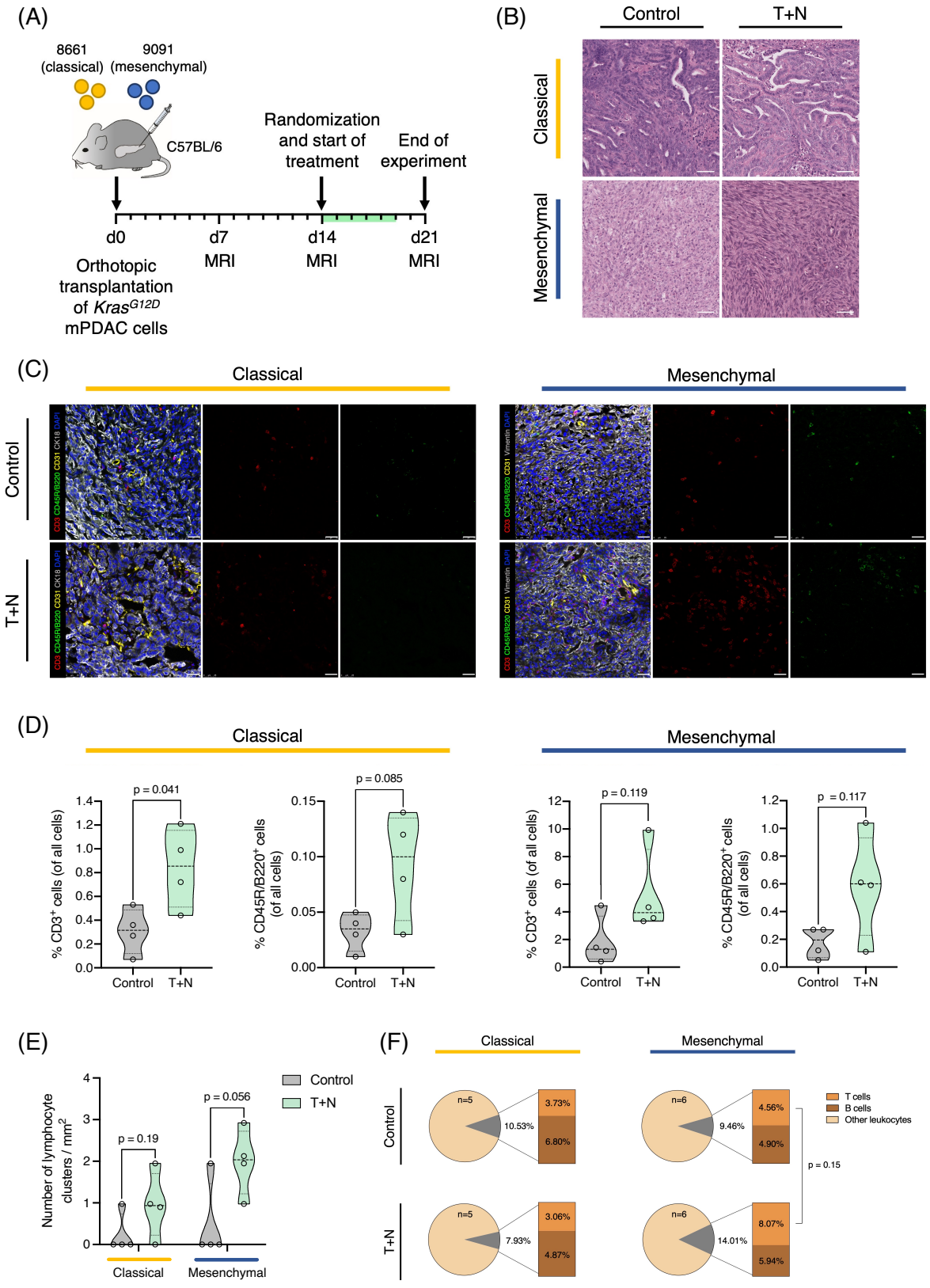

Figure 10: The combinatorial drug treatment increases adaptive immune cell infiltration in tumors derived from orthotopic transplantation of *Kras*^{G12D}-driven mPDAC cells
(A) Schematic representation of the experimental set up. Classical (cell line 8661) and mesenchymal (cell line 9091) mPDAC cells from KC mice were orthotopically transplanted into immunocompetent syngeneic C57BL/6 mice. The experimental cohort received one cycle of the combinatorial treatment with trametinib and nintedanib while the control group only received vehicle treatment (indicated by

green bar). All animals were sacrificed on day 21. This experiment was performed by Chiara Falcomatà and Stefanie Bärthel. (B) Representative images of H&E stainings of sections from vehicle and T/N-treated classical and mesenchymal tumors derived from orthotopic transplantation. Unlike endogenous *Kras*^{G12D}-driven mPDAC of the classical subtype, tumors derived from orthotopic transplantation of the classical mPDAC cell line 8661 predominantly present a papillary tumor morphology with low stromal content. 2 different tumors of each condition are shown. Scale bars 50 µm. (C) Representative images of immunofluorescence stainings for CD3$^+$ T cells (red) and CD45R/B220$^+$ B cells (green) of sections from vehicle and T/N-treated classical (left) and mesenchymal (right) tumors derived from orthotopic transplantation. In this modified lymphocyte staining panel (see Figure 5), CD31 (yellow) was used to detect endothelial cells. CK18 was used to detect epithelial PDAC cells in classical tumors while vimentin was used to detect mesenchymal PDAC cells in mesenchymal tumors (white). Nuclear staining was performed with DAPI (blue). Scale bars 25 µm. (D) Quantification of CD3$^+$ T cells and CD45R/B220$^+$ B cells from immunofluorescence stainings of classical (left) and mesenchymal (right) tumor sections as depicted in (C). Individual tumors are shown as single points in the graph (n=4 for each condition). (E) Quantification of lymphocyte clusters from immunofluorescence stainings of classical (left) and mesenchymal (right) tumor sections as depicted in (C). Lymphocyte clusters were defined as clusters with ≥ 10 CD3$^+$ cells and ≥ 1 CD45R/B220$^+$ B cells. Individual tumors are shown as single points in the graph (n=4 for each subtype). (F) Pie charts representing the fractions of adaptive immune cell populations among all leukocytes as analyzed by flow cytometry in tumor tissues from vehicle and T/N-treated C57BL/6 mice orthotopically transplanted with classical (left) and mesenchymal (right) tumor cells. The number of tumors per condition analyzed is indicated in the respective graphs. Flow cytometry data were acquired by Chiara Falcomatà and Stefanie Bärthel. P-values in (D), (E) and (F) were calculated using a two-tailed, unpaired Welch's t test.

---

of CD45R/B220$^+$ B cells also tended to increase in this subtype ($p = 0.085$). A similar trend towards an increase in T and B cell infiltration could be observed in T/N-treated mesenchymal tumors (Figure 10(D), right), although intertumoral variation was relatively big and results were not statistically significant ($p = 0.12$ for both T and B cells). No significant correlation of T and B cell infiltrations could be detected in T/N-treated orthotopically transplanted tumors (Pearson's $r = 0.54$, $p = 0.16$, data not shown).

Further analysis of lymphocytic infiltration patterns revealed existence of mixed lymphocyte clusters without higher spatial organization in some of the tumors, similar to those found in endogenous *Kras*^{G12D}-driven mPDAC (see Figure 7(B), middle). However, no TLS-like lymphocyte clusters (see Figure 7(B), left) were found, neither in control nor in T/N-treated tumors of both subtypes. Furthermore, as opposed to the higher density of lymphocyte clusters in classical endogenous tumors, the number of mixed lymphocyte clusters per mm^2 in orthotopically transplanted tumors was equally low in both the classical and mesenchymal subtype (Figure 10(E)). Upon combinatorial treatment, a clear trend towards an increased number of lymphocyte clusters was observed particularly in the mesenchymal subtype ($p = 0.056$), while the difference appeared to be less pronounced in classical tumors ($p = 0.19$).

Results from quantifications based on immunofluorescence stainings (Figure 10(D)) were then compared to proportions of T cells among intratumoral leukocytes determined via flow cytometry (Figure 10(F)), revealing a trend towards an increased fraction of T cells upon combinatorial treatment specifically in the mesenchymal subtype ($p = 0.15$).

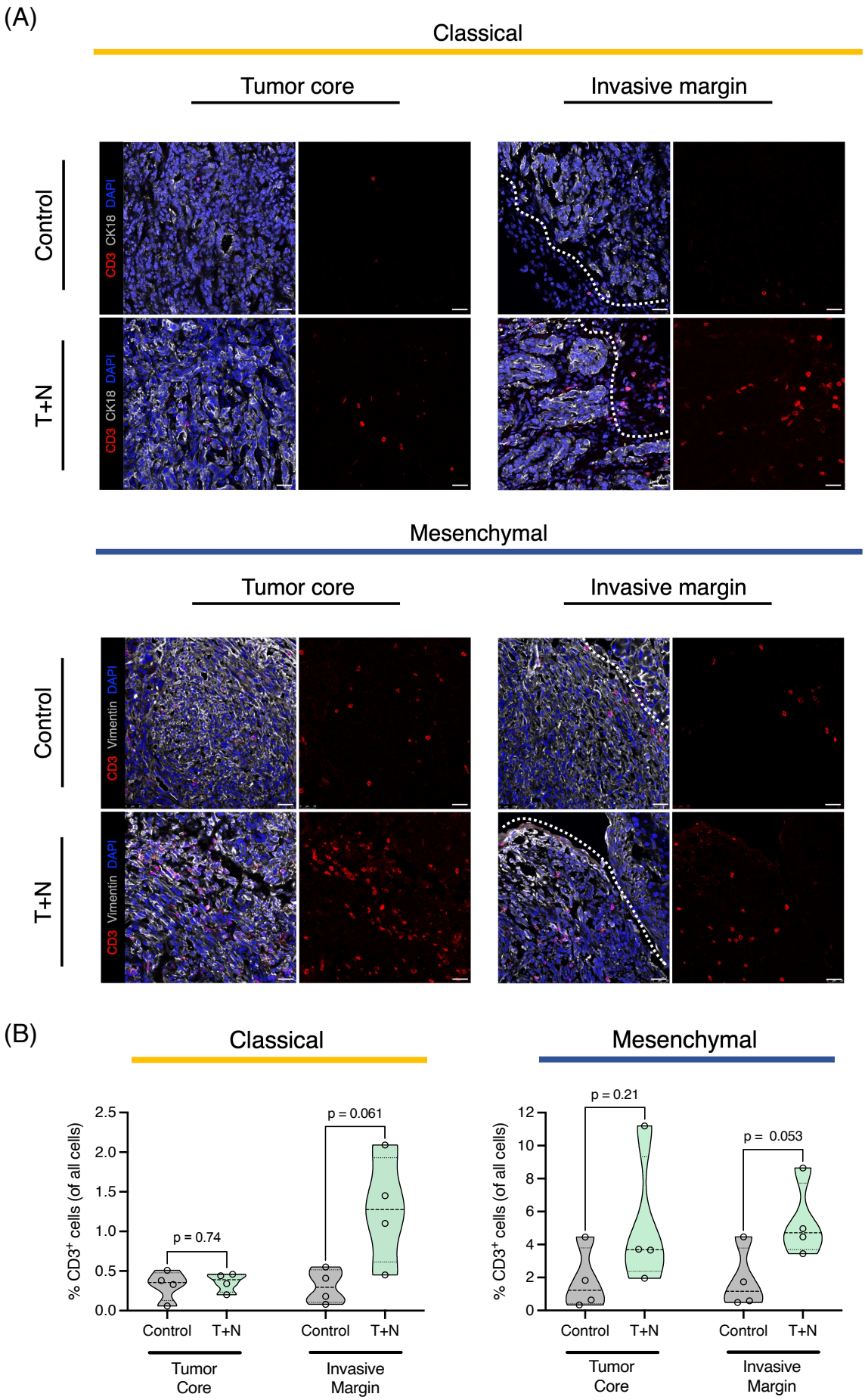
(A)
Classical
Tumor core
Invasive margin
Control
T+N
CD3 CK18 DAPI
Mesenchymal
Vimentin
(B)
% CD3+ cells (of all cells)
p = 0.74
p = 0.061
p = 0.21
p = 0.053
Control
T+N
Tumor Core
Invasive Margin

Figure 11: Combinatorial treatment-induced T cell recruitment is most pronounced at the invasive margins in tumors of the classical subtype, while tumors of the mesenchymal subtype also demonstrate increased T cell infiltration in the tumor core
(A) Representative images of immunofluorescence stainings for $CD3^+$ T cells (red) of sections from vehicle and T/N-treated tumors derived from orthotopic transplantation, illustrating differential T cell infiltration at the invasive margins and in the tumor core for tumors of the classical (upper panel) and mesenchymal (lower panel) subtype. Invasive margins are defined as regions of 400 µm width on each side of the border between the tumor cells and adjacent pancreatic tissue (marked with a white dotted line). CK18 was used to detect epithelial PDAC cells in classical tumors while vimentin was used to detect mesenchymal PDAC cells in mesenchymal tumors (white). Nuclear staining was performed with DAPI (blue). Scale bars 25 µm. (B) Quantification of $CD3^+$ T cells from immunofluorescence stainings of classical (left) and mesenchymal (right) tumor sections as depicted in (A). Individual tumors are shown as single points in the graph (n=4 for each condition). P-values in (B) were calculated using a two-tailed, unpaired Welch's t test.

3.2.2 Mesenchymal PDAC display an increased T cell infiltration into the tumor core upon combinatorial treatment

To analyze spatial distribution of tumor infiltrating T cells and changes upon combinatorial treatment, $CD3^+$ T cells were quantified in at least 5 images each from invasive margins (defined as a zone of 400 µm width on each side of the border between tumor cells and adjacent tissue) and tumor core of n = 4 classical and n = 4 mesenchymal tumors as shown in Figure 11(A). In orthotopically transplanted tumors of the classical subtype, a substantially increased T cell infiltration upon combinatorial treatment could only be observed at the invasive margins ($p = 0.061$), while mean T cell counts in the tumor core did not differ between control and T/N-treated tumors ($p = 0.74$) (Figure 11(B), left). In contrast, T cell infiltration tended to be stronger both at the invasive margins and in the tumor core of T/N-treated mesenchymal tumors, with p-values of 0.053 and 0.21, respectively (Figure 11(B), right), indicating a more efficient combinatorial treatment-induced T cell recruitment in this PDAC subtype.

3.2.3 The fraction of cytotoxic T cells increases specifically in the mesenchymal subtype upon combinatorial treatment

The effects of the combinatorial treatment on proportions of different tumor infiltrating T cell subpopulations were explored by additional multiplex immunofluorescence stainings of classical and mesenchymal tumors derived from orthotopic transplantation. Representative images are shown in Figure 12(A). To quantify fractions of T cell subpopulations, the number of $CD3^+CD8^+$ cytotoxic T cells, $CD3^+CD4^+FOXP3^-$ helper T cells and $CD3^+CD4^+FOXP3^+$ regulatory T cells, as well as the number of all $CD3^+$ T cells, was determined in 10-12 random fields of view at 400x magnification of n = 4 individual tumors per subtype and treatment condition. In classical tumors, the increase in T cell infiltration (Figure 10(D)) upon

combinatorial treatment was characterized by equally increased numbers of cytotoxic T cells, helper T cells and regulatory T cells, resulting in stable proportions of the respective T cell subpopulations among all T cells (Figure 12(B), left). In the mesenchymal subtype however, fractions of T cell subpopulations were altered by the combinatorial treatment (Figure 12(B), right). Notably, a trend towards an increased fraction of cytotoxic T cells could be observed in T/N-treated mesenchymal tumors ($p = 0.23$), while fractions of helper and regulatory T cells tended to decrease upon treatment ($p = 0.23$ and $p = 0.39$, respectively).

Based on these findings and with regard to the differential patterns of treatment-induced T cell infiltration in classical and mesenchymal tumors (Figure 11), images of invasive margins and cores of the tumors stained for T cell subpopulations (Figure 12(A)) were analyzed to assess intratumoral distribution of cytotoxic T cells. $CD3^+CD8^+$ cytotoxic and all $CD3^+$ T cells were quantified in at least 4 fields of view each from invasive margins and tumor core of $n = 4$ classical and $n = 4$ mesenchymal tumors. In the classical subtype, no clear trend could be detected for combinatorial treatment-induced changes in cytotoxic T cell fractions at the invasive margins or in the tumor core, as depicted in the left graph in Figure 12(C). In contrast, T/N-treated mesenchymal tumors demonstrated an increased proportion of cytotoxic T cells of up to 80% of all T cells in the tumor core and, to a lesser extent, at the invasive margins compared to control tumors of the mesenchymal subtype (Figure 12(C), right), but results were not statistically significant ($p = 0.19$ and $p = 0.28$, respectively). In summary, the combinatorial treatment led to an increased proportion of $CD8^+$ cytotoxic T cells among tumor infiltrating T cells both at the invasive margins and in the tumor core only in mesenchymal PDAC, whereas fractions of T cell subpopulations remained unchanged in tumors of the classical subtype.

Figure 12: The fraction of $CD8^+$ cytotoxic T cells increases upon combinatorial drug treatment specifically in tumors derived from orthotopic transplantation of mesenchymal mPDAC cells
(A) Representative images of immunofluorescence stainings for $CD8^+$ cytotoxic T cells (magenta), $CD4^+$ $FOXP3^-$ helper T cells (green) and $CD4^+$ $FOXP3^+$ regulatory T cells (cyan) of sections from vehicle and T/N-treated classical (upper panel) and mesenchymal (lower panel) tumors derived from orthotopic transplantation. In this modified T cell subpopulations staining panel (see Figure 5), CD3 (red) was used to detect T cells. CK18 (white) was used to detect epithelial PDAC cells in classical tumors while vimentin was used to detect mesenchymal PDAC cells in mesenchymal tumors. Nuclear staining was performed with TO-PRO-3 (blue). Scale bars 25 µm. (B) Quantification of $CD8^+$ cytotoxic T cells, $CD4^+$ $FOXP3^-$ helper T cells and $CD4^+FOXP3^+$ regulatory T cells from immunofluorescence stainings of classical (left) and mesenchymal (right) tumor sections as depicted in (A). Results are displayed as fractions of $CD3^+$ T cells. Individual tumors are shown as single points in the graph (n=4 for each condition). (C) Quantification of $CD8^+$ cytotoxic T cells as fractions of $CD3^+$ T cells at the invasive margins and in the tumor core, as defined in Figure 11(A) of vehicle and T/N-treated classical (left) and mesenchymal (right) tumors derived from orthotopic transplantation. Individual tumors are shown as single points in the graph (n=4 for each condition). P-values in (B) and (C) were calculated using a two-tailed, unpaired Welch's t test. **(Figure on next page)**

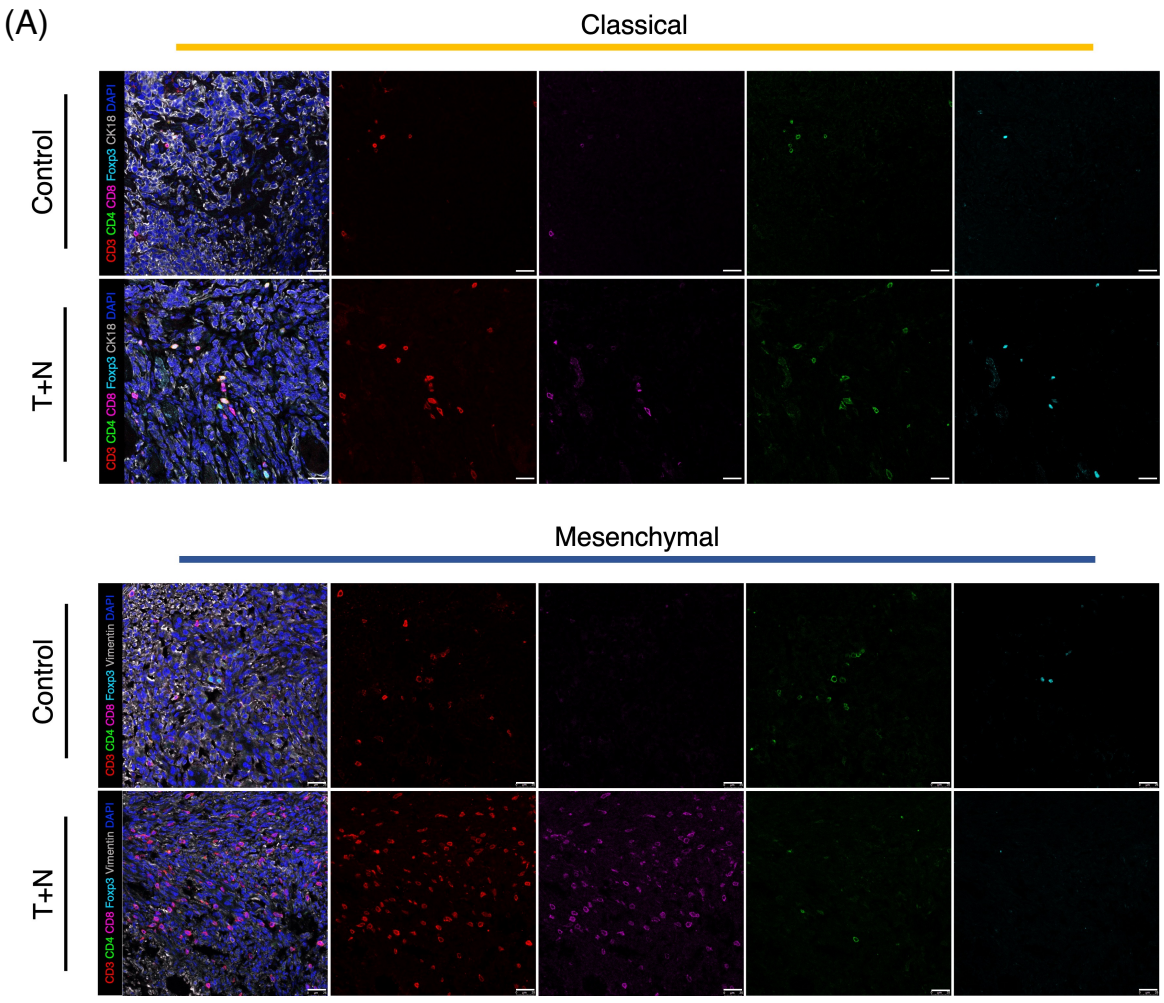
(A)
Classical
Control
T+N
CD3 CD4 CD8 Foxp3 CK18 DAPI
Mesenchymal
Control
T+N
CD3 CD4 CD8 Foxp3 Vimentin DAPI

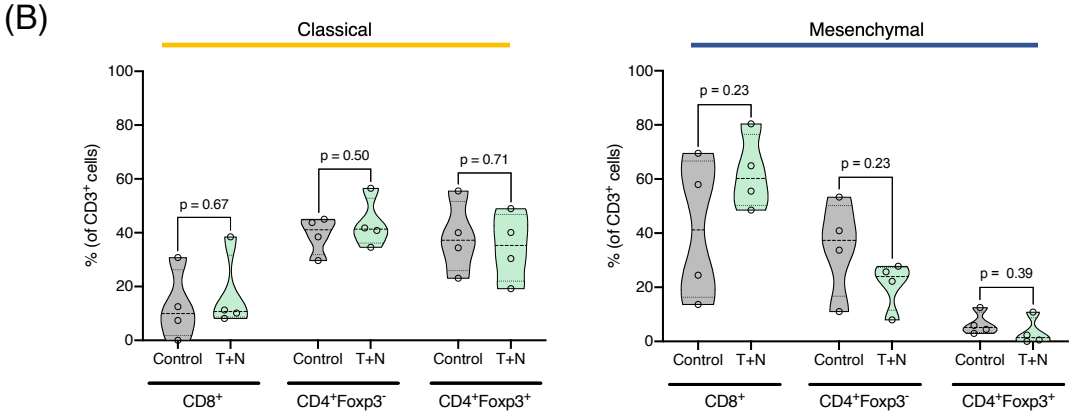
(B)
Classical
Mesenchymal
% (of CD3+ cells)
p = 0.67
p = 0.50
p = 0.71
p = 0.23
p = 0.23
p = 0.39
Control
T+N
CD8+
CD4+Foxp3-
CD4+Foxp3+

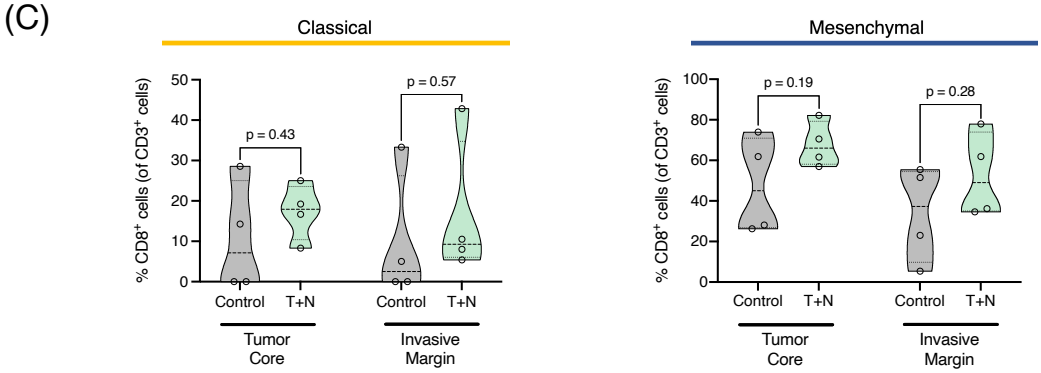
(C)
Classical
Mesenchymal
% CD8+ cells (of CD3+ cells)
p = 0.43
p = 0.57
p = 0.19
p = 0.28
Control
T+N
Tumor Core
Invasive Margin

3.2.4 Classical and mesenchymal PDAC display features of combinatorial treatment-induced vascular remodeling

Besides the combinatorial treatment-induced T cell recruitment, alterations of the tumor vasculature were noticed upon close inspection of T/N-treated tumor sections stained for lymphocytes and blood vessels as shown in Figure 10(C) and Figure 13(A). While most vessels in vehicle-treated tumors appeared to be collapsed, widening of vessels could be observed upon combinatorial treatment (Figure 13(B), white arrows). To compare these combinatorial treatment-induced changes in tumor vasculature morphology between classical and mesenchymal tumors derived from orthotopic transplantation, $CD31^+$ blood vessels with visible lumen were quantified for n = 4 individual tumors per subtype and treatment condition in the same fields of view which were analyzed in Figure 10(D). Strikingly, classical orthotopically transplanted tumors displayed a relatively sparse tumor vasculature (Figure 13(B)) with a significantly smaller proportion of blood vessels with visible lumen at baseline than endogenous tumors of the same subtype ($p = 0.0093$), while no difference between orthotopically transplanted tumors from the control group and endogenous tumors was observed for the mesenchymal subtype ($p = 0.76$; cf. Figure 9(B) and Figure 13(C)). Close inspection of classical endogenous mPDAC revealed a similarly sparse microvasculature in regions characterized by a papillary gland-forming pattern with relatively high tumor cellularity and low stromal content resembling morphology of classical orthotopically transplanted tumors (cf. Figure 9(C) and Figure 13(B)). As shown in Figure 13(C), the combinatorial treatment led to a substantially increased amount of $CD31^+$ blood vessels with visible lumen in mesenchymal tumors ($p = 0.051$). A similar trend was found for classical tumors ($p = 0.115$), indicating a modulatory effect of the combinatorial treatment on tumor vasculature in both subtypes.

Co-localization of T cells and blood vessels with visible lumen was observed in both control and T/N-treated orthotopically transplanted tumors of the classical and mesenchymal subtype (Figure 13(D)), matching findings in endogenous $Kras^{G12D}$-driven mPDAC (see Figure 9(D)). To investigate whether the combinatorial treatment affected co-localization, quantifications of $CD3^+$ T cells (Figure 10(D)) and $CD31^+$ blood vessels with visible lumen (Figure 13(C)) were used for correlation analysis. As depicted in Figure 13(E) (left), higher vessel densities were generally associated with stronger T cell infiltration in control tumors, although some intertumoral variation was present and correlation was not statistically significant (Pearson's $r = 0.71$; $p = 0.076$), as opposed to findings in endogenous tumors (see Figure 9(E)). Furthermore, classical and not mesenchymal tumors derived from orthotopic transplantation clustered at the lower end of the regression line as they displayed both very few blood vessels with open lumina (described above) and particularly poor T cell infiltration (see 3.2.1)

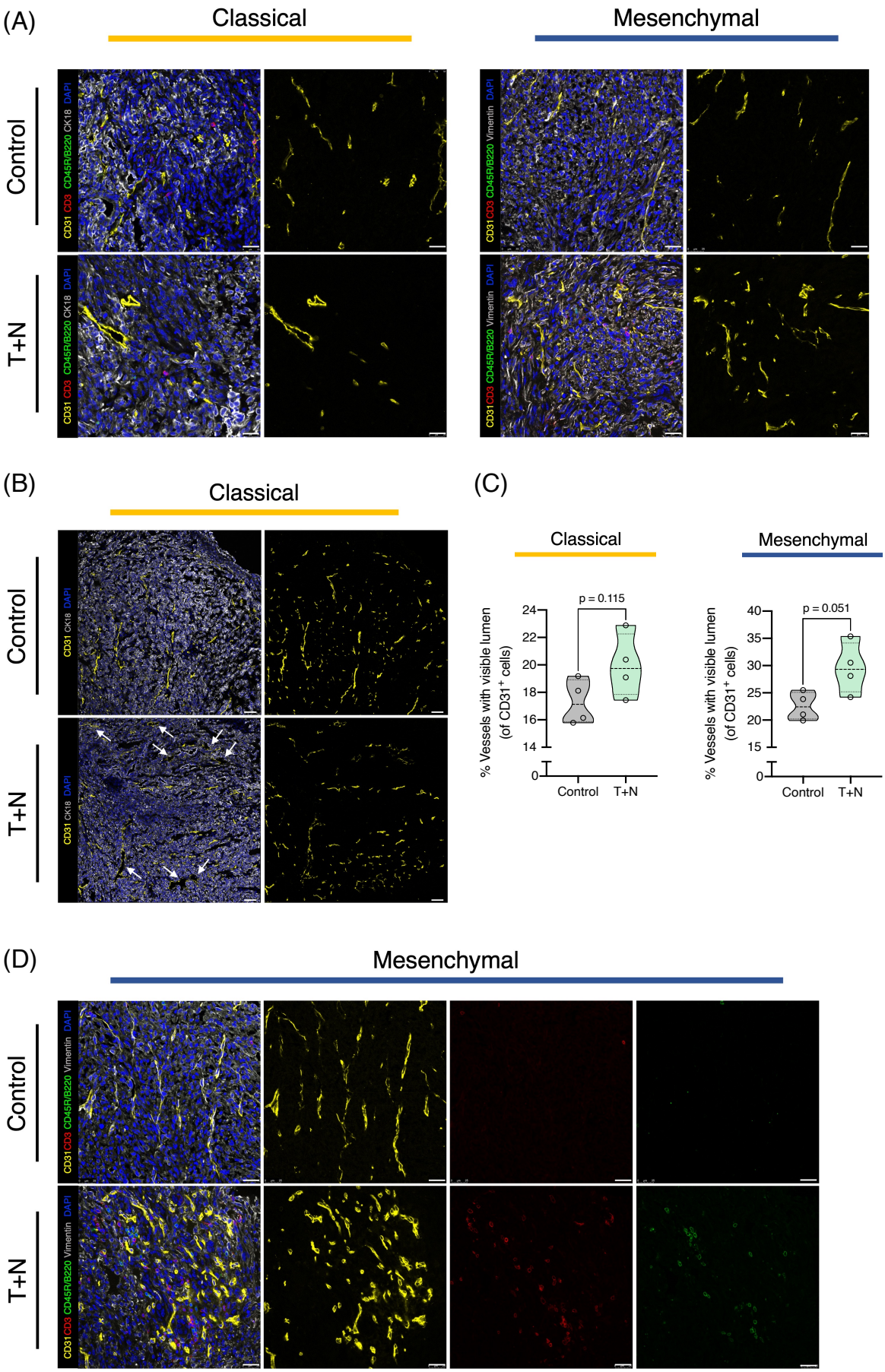
(A)
Classical
Mesenchymal
Control
T+N
CD31 CD3 CD45R/B220 CK18 DAPI
CD31 CD3 CD45R/B220 Vimentin DAPI
(B)
Classical
Control
T+N
CD31 CK18 DAPI
(C)
Classical
Mesenchymal
% Vessels with visible lumen (of CD31+ cells)
p = 0.115
p = 0.051
Control
T+N
(D)
Mesenchymal
Control
T+N
CD31 CD3 CD45R/B220 Vimentin DAPI

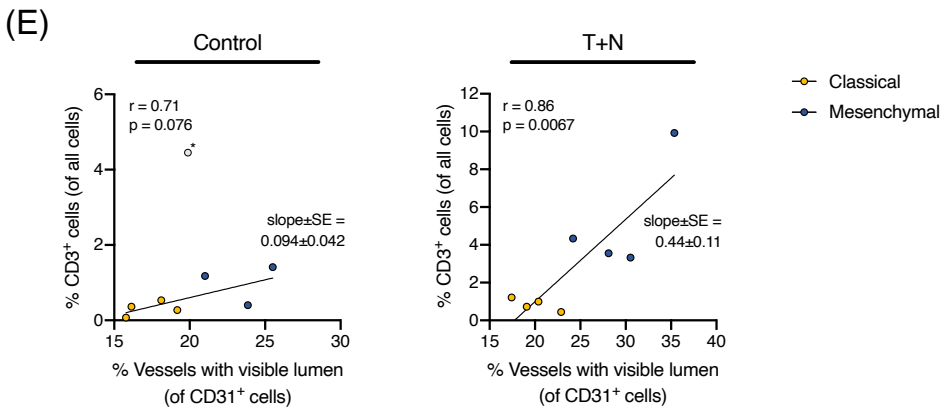

Figure 13: Morphology of tumor vasculature changes upon combinatorial treatment in both subtypes of tumors derived from orthotopic transplantation
(A) Representative images of immunofluorescence stainings for CD31+ endothelial cells (yellow) from vehicle and T/N-treated classical (left) and mesenchymal (right) tumors derived from orthotopic transplantation. The staining panel corresponds to the modified lymphocyte staining panel used in Figure 10(C). Scale bars 25 µm. (B) Representative images of immunofluorescence stainings for CD31+ endothelial cells (yellow) showing differences in tumor vasculature morphology between vehicle and T/N-treated classical tumors derived from orthotopic transplantation. Vessels with visible lumen are marked with white arrows. The staining panel corresponds to (A). Each image is composed of 3 x 3 individual images acquired at 400x magnification. Scale bars 50 µm. (C) Quantification of CD31+ vessels with visible lumen from immunofluorescence stainings of classical and mesenchymal tumor sections as depicted in (A). Results are shown as fractions of CD31+ cells. Individual tumors are shown as single points in the graph (n=4 for each condition). P-values were calculated using a two-tailed, unpaired Welch's t test. (D) Representative images of immunofluorescence stainings for CD31+ endothelial cells (yellow), CD3+ T cells (red) and CD45R/B220+ B cells (green) in the mesenchymal subtype, highlighting co-localization of adaptive immune cells and vessels specifically in T/N-treated tumors. The staining panel corresponds to (A). Scale bars 25 µm. (E) Pearson's correlation analysis and simple linear regression of CD31+ vessels and CD3+ T cells as quantified in Figure 10(D) and Figure 13(C) for control (left) and T/N-treated (right) orthotopically transplanted tumors of the classical (yellow) and mesenchymal (blue) subtype. One outlier was excluded from the analysis (marked with an asterisk).

---

compared to endogenous mPDAC of the classical subtype, whereas ratios were consistent in both models for mesenchymal tumors (cf. Figure 9(E) and Figure 13(E)).

In T/N-treated orthotopically transplanted tumors, the amount of CD31+ blood vessels with visible lumen strongly correlated with abundance of CD3+ T cells (Pearson's r = 0.86; p = 0.0067) (Figure 13(E), right). Interestingly, T/N-treated tumors showed a trend towards a stronger increase in T cell infiltration with higher vessel densities compared to the moderate increase in control tumors (slope of linear regression ± SE = 0.44 ± 0.11 vs. 0.094 ± 0.042, p = 0.064), suggesting involvement of additional factors besides vessel density in combinatorial-treatment induced T cell recruitment.

3.2.5 The combinatorial treatment induces vascular maturation and endothelial cell activation specifically in the mesenchymal subtype

To assess further effects of the combinatorial treatment on tumor vasculature, additional multiplex immunofluorescence staining panels were established and optimized, detecting α-SMA in vascular smooth muscle cells and pericytes as well as P-selectin expression on the surface of endothelial cells (Figure 5) as markers of vascular maturation and stability (Ribatti et al., 2011; Bergers & Song, 2005) and endothelial cell activation in the context of inflammation (Hunt & Jurd, 1998; Lorenzon et al., 1998), respectively. Representative images of immunofluorescence-stained tumor sections are shown in Figure 14(A) and (B). For quantification of α-SMA$^+$ vessels, the numbers of all CD31$^+$ blood vessels and those covered with α-SMA$^+$ pericytes were determined in at least 8 fields of view at 400x magnification of n = 3 – 5 tumors per subtype and treatment condition. The proportion of vessels with luminal expression of P-selectin on CD31$^+$ endothelial cells among all intratumoral blood vessels was quantified analogously. Upon combinatorial treatment, mesenchymal tumors showed a significantly increased proportion of α-SMA$^+$ vessels ($p = 0.034$), while no clear trend could be observed in the classical subtype (Figure 14(C)). For P-selectin expression, similarly divergent effects of the combinatorial treatment were noticed, with a significant increase in P-selectin$^+$ vasculature in mesenchymal tumors compared to no difference in classical tumors (Figure 14(D)), suggesting that the T/N combination therapy induces multiple phenotypes of vascular remodeling including vascular maturation and endothelial cell activation specifically in the mesenchymal subtype.

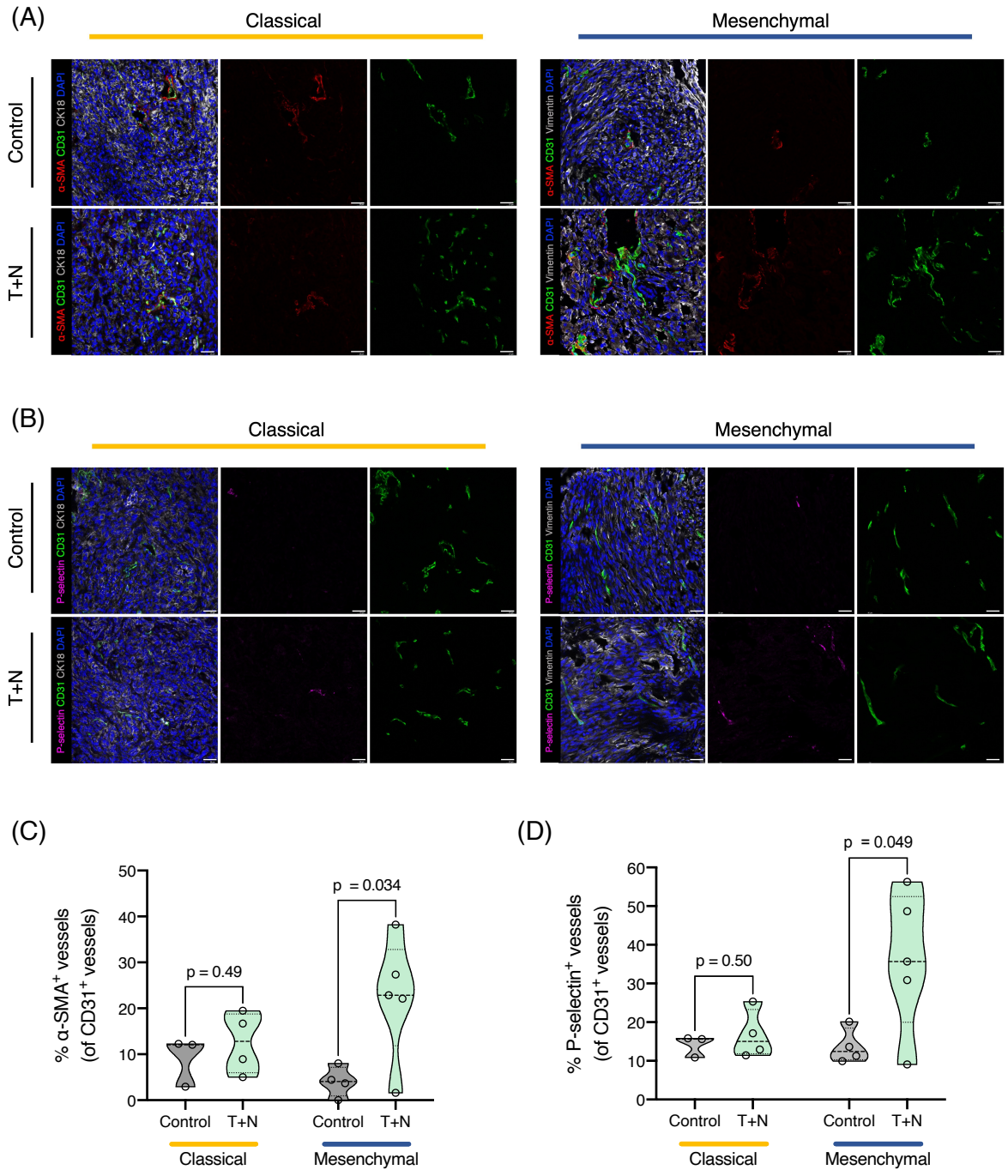

Figure 14: The combinatorial treatment induces vascular remodeling with vascular maturation and endothelial cell activation specifically in tumors derived from orthotopic transplantation of mesenchymal mPDAC cells

(A) Representative images of immunofluorescence stainings for α-SMA (red) and CD31 (green) of sections from vehicle and T/N-treated classical (left) and mesenchymal (right) tumors derived from orthotopic transplantation. In this staining panel (see Figure 5(E)), CK18 was used to detect epithelial PDAC cells in classical tumors while vimentin was used to detect mesenchymal PDAC cells in mesenchymal tumors. Nuclear staining was performed with DAPI. Scale bars 25 µm. (B) Representative images of immunofluorescence stainings for P-selectin (magenta) and CD31 (green) of sections from vehicle and T/N-treated classical (left) and mesenchymal (right) tumors derived from orthotopic transplantation. In this staining panel (see Figure 5(E)), CK18 / vimentin and DAPI were used as described in (A). Scale bars 25 µm. (C), (D) Quantification of α-SMA+ (C) and P-selectin+ (D) vessels from immunofluorescence stainings of classical (left) and mesenchymal (right) tumor sections as depicted in (A) and (B), respectively. Results are shown as fractions of CD31+ vessels. Individual

tumors are shown as single points in the graph (classical: control n=3 and T/N n=4; mesenchymal: control n=4 and T/N n=5). P-values in (C) and (D) were calculated using a two-tailed, unpaired Welch's t test.

3.3 The role of T cells in therapy response of mesenchymal PDAC

3.3.1 T cells significantly contribute to *in vivo* efficacy of the combinatorial treatment in mesenchymal PDAC

To investigate contribution of the combinatorial treatment-induced T cell-mediated anti-tumor immunity observed particularly in mesenchymal tumors (see Figure 10, Figure 11 and Figure 12) to therapy response, T cell-deficient *CD3ε-KO* mice were employed to conduct additional orthotopic transplantation experiments using the mesenchymal cell line derived from *Kras^{G12D}*-driven mPDAC (Figure 15(A)). Animals in control and treatment arms received weekly cycles of vehicle or combinatorial T/N treatment, respectively, and tumor growth was monitored via MRI. Analysis of survival data revealed that the combinatorial treatment still led to a significant increase in overall survival in *CD3ε-KO* mice ($p = 0.027$), with a median survival of 36 days compared to 31 days in the control cohort (Figure 15(B), right). However, in comparison to immunocompetent C57BL/6 mice for which a remarkable prolongation of survival by 20 days had been shown (Figure 15(B), left), only a shortened survival benefit of 5 days over the control cohort could be observed, indicating a substantially decreased therapy response in T cell-deficient mice. Interestingly, survival times of control C57BL/6 and *CD3ε-KO* tumor-bearing mice did also significantly differ, with a longer median survival in the *CD3ε-KO* cohort ($p < 0.0001$).

Additionally, tumor volumes as measured by weekly MRI scans were analyzed as another indicator of therapy response. Figure 15(C) shows representative axial MRI sections of vehicle and T/N-treated T cell-deficient *CD3ε-KO* mice orthotopically transplanted with mesenchymal tumor cells before and after the second cycle of combinatorial treatment. While the tumor volume rapidly increased in the control tumor (upper row), only a minor increase is detectable in the T/N-treated tumor (lower row). Accordingly, quantification of tumor volume changes in $n = 14$ control and $n = 15$ T/N-treated *CD3ε-KO* mice as depicted in Figure 15(D) revealed a significantly reduced tumor growth already after the first cycle of the combinatorial treatment compared to the control cohort ($p = 0.0016$), but no regression of tumors was observed. In contrast, nearly half of the tumors in immunocompetent C57BL/6 mice showed partial regression upon combinatorial treatment and reduction of tumor volumes was significantly stronger than in *CD3ε-KO* mice ($p = 0.0062$), suggesting that T cell deficiency indeed decreases efficacy of the T/N combination therapy.

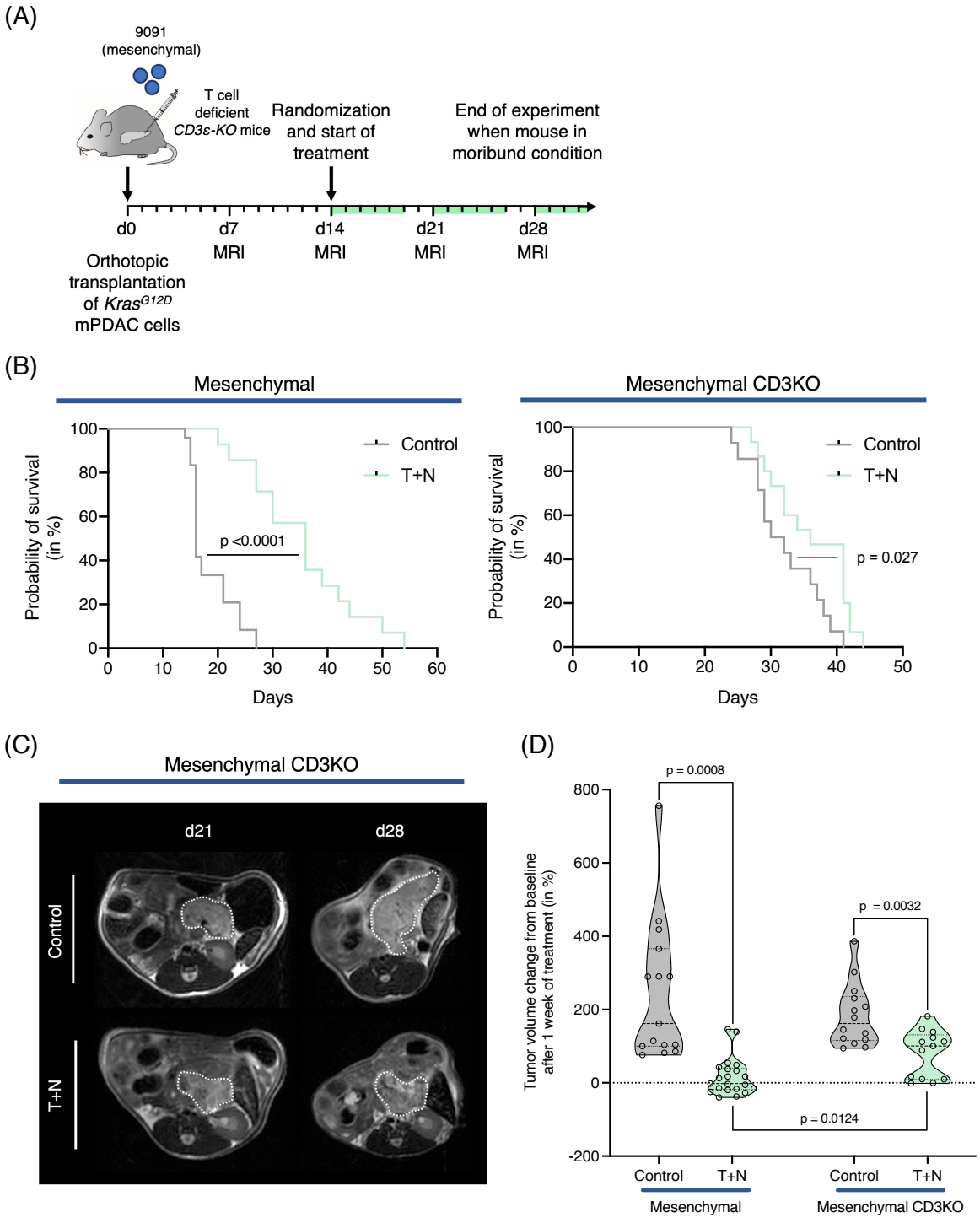

Figure 15: Response to combinatorial treatment is reduced in T cell-deficient *CD3ε-KO* mice orthotopically transplanted with mesenchymal mPDAC cells

(A) Schematic representation of the experimental set up. Mesenchymal mPDAC cells (cell line 9091) were orthotopically transplanted into T cell-deficient CDε-knockout (*CD3ε-KO*) mice. Animals in the experimental cohort received weekly treatment cycles with trametinib and nintedanib or vehicle (indicated by green bars) until they had to be sacrificed. (B) Kaplan-Meier survival curves of control (grey) and T/N-treated (green) C57BL/6 (left) and T cell-deficient *CD3ε-KO* mice (right) orthotopically transplanted with mesenchymal tumor cells (control *n*=24 and T/N *n*=14 for C57BL/6 mice; control *n*=14 and T/N *n*=15 for *CD3ε-KO* mice). P-value was calculated using the log-rank Mantel-Cox test. Survival data of C57BL/6 mice were collected by Chiara Falcomatà. (C) Representative MRI images of vehicle and T/N-treated T cell-deficient *CD3ε-KO* mice orthotopically transplanted with mesenchymal tumor cells before (d21) and after (d28) the second treatment cycle. Tumors are

encircled by a white dotted line. (D) Graph representing the changes in tumor volume in vehicle (grey) and T/N-treated (green) C57BL/6 (left) and T cell-deficient *CD3ε-KO* mice (right) orthotopically transplanted with mesenchymal tumor cells after 1 week of treatment. Individual tumors are shown as single points in the graph (control n=15 and T/N n=21 for C57BL/6 mice; control n=14 and T/N n=13 for *CD3ε-KO* mice). P-values in (D) were calculated using two-tailed, unpaired Welch's t tests and corrected for multiple comparisons using the Bonferroni-Šídák method. MRI data of C57BL/6 mice were collected by Chiara Falcomatà.

3.3.2 B cell infiltration increases upon combinatorial treatment, but displays an abnormal spatial distribution in mesenchymal PDAC from *CD3ε-KO* mice

To identify potential underlying mechanisms of the partial therapy response despite T cell deficiency (Figure 15), combinatorial treatment-induced immune responses in *CD3ε-KO* mice were characterized via flow cytometry and multiplex immunofluorescence staining for lymphocytes, blood vessels and tumor cells (see Figure 5(C)). As evidenced by Figure 16(A), flow cytometry analysis of mesenchymal tumors derived from orthotopic transplantation (see Figure 15(A)) confirmed absolute T cell deficiency of *CD3ε-KO* animals (right plot), while T cells were abundantly present in tumors from C57BL/6 mice (see Figure 10(A)) used as a positive control (left plot). Mesenchymal tumors in *CD3ε-KO* mice showed a strong increase in $CD19^+$ B cells upon combinatorial treatment ($p = 0.011$), with a fraction of up to 31% of all intratumoral leukocytes (mean ± SD = 17.84% ± 8.62% for T/N vs. 2.81% ± 0.95% for control tumors) (Figure 16(B)). Strikingly, while baseline fractions of B cells did not differ between immunocompetent C57BL/6 and T cell-deficient *CD3ε-KO* mice, the latter presented a significantly stronger increase in B cell abundance upon combinatorial treatment compared to C57BL/6 mice ($p = 0.030$; cf. Figure 10(F) and Figure 16 (B)).

Distribution of B cells within the tumors was assessed in immunofluorescence-stained tumor sections of control and T/N-treated *CD3ε-KO* mice as shown in Figure 16(C). While only few $CD45R/B220^+$ B cells were found scattered in control tumors, an increased number of B cells could be observed upon combinatorial treatment. However, as opposed to findings in C57BL/6 mice, foci of B cells were almost exclusively located within blood vessels (Figure 16(E)) and no clusters could be detected within the tumor tissue except for one small cluster of B cells in a T/N-treated tumor. For quantification of B cells, at least 10 fields of view at 400x magnification of $n = 5$ control and $n = 4$ T/N-treated tumors were analyzed, revealing a trend towards an increased total number of intratumoral B cells upon combinatorial treatment ($p = 0.069$) matching flow cytometry results (Figure 16(D), left).

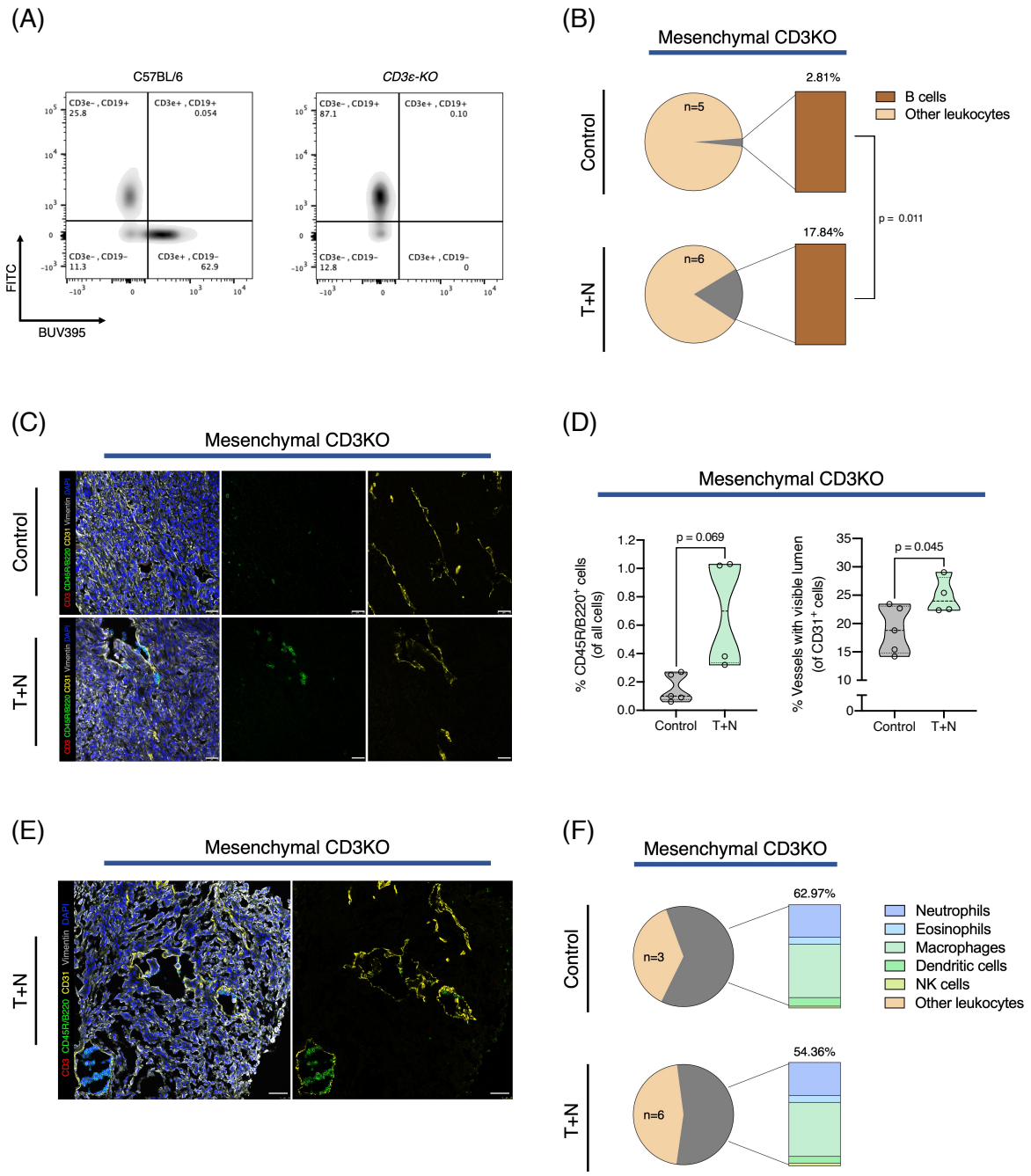

Figure 16: B cell abundance increases upon combinatorial treatment in T cell-deficient *CD3ε-KO* mice orthotopically transplanted with mesenchymal mPDAC cells, while fractions of innate immune cell populations remain stable

(A) Representative plots from flow cytometry analyses of immunodeficient *CD3ε-KO* and C57BL/6 mice, highlighting the lack of T cells in the *CD3ε-KO* animals. (B) Pie charts representing the fraction of adaptive immune cell populations in tumor tissues from vehicle and T/N-treated *CD3ε-KO* mice as analyzed by flow cytometry. The number of tumors per condition analyzed is indicated in the respective graphs. (C) Representative images of immunofluorescence stainings for CD45R/B220$^+$ B cells and CD31$^+$ endothelial cells in tumor sections from vehicle and T/N-treated *CD3ε-KO* mice. No CD3$^+$ T cells (red) can be detected. In this modified lymphocyte staining panel (see Figure 5), CD31 (yellow), Vimentin (white) and DAPI (blue) were used to detect endothelial cells, mesenchymal tumor cells and nuclei, respectively. Scale bars 25 µm. (D) Quantification of CD45R/B220$^+$ B cells and CD31$^+$ vessels with visible lumen from immunofluorescence stainings of tumor sections from vehicle and T/N-treated *CD3ε-KO* mice as depicted in (C). Results are shown as fractions of CD31$^+$ cells. Individual tumors are shown as single points in the graph (control n=5, T/N n=4). (E) Representative image of immunofluorescence stainings for CD45R/B220$^+$ and CD31$^+$ showing B cell distribution and

vessel morphology in T/N-treated *CD3ε-KO* mice. The staining panel corresponds to (A). Image is a tile scan composed of 3 x 3 individual images acquired at 400x magnification. Scale bars 50 µm. (F) (G) Pie charts representing the fraction of innate immune cell populations in tumor tissues from vehicle and T/N-treated *CD3ε-KO* mice as analyzed by flow cytometry. The number of tumors per condition analyzed is indicated in the respective graphs. P-values in (B), (D) and (F) were calculated using a two-tailed, unpaired Welch's t test.

Similar to findings in C57BL/6 mice (see Figure 13), morphological changes of tumor vasculature could also be observed in *CD3ε-KO* mice, with blood vessels harboring widely open lumina in T/N-treated mesenchymal tumors (Figure 16(C)). Quantification of $CD31^+$ blood vessels was performed on the same fields of view in which B cells were counted, showing a significantly increased proportion of vessels with visible lumen upon combinatorial treatment ($p = 0.045$), as depicted in Figure 16(D) (right). Interestingly, several large blood vessels with a diameter of > 100 µm and aggregation of intraluminal B cells were found in close proximity to each other in two T/N-treated tumors from *CD3ε-KO* mice (Figure 16(E)), a phenotype which had not been observed in tumors of C57BL/6 background.

3.3.3 The combinatorial treatment does not alter innate immune cell infiltration in mesenchymal PDAC of T cell-deficient *CD3ε-KO* mice

To evaluate potential effects of the combinatorial treatment on non-B cell mediated immune responses in mesenchymal tumor-bearing *CD3ε-KO* mice, fractions of innate immune cells were analyzed via flow cytometry. In line with the increased number of B cells (Figure 16(B)), total counts of neutrophils, eosinophils, macrophages, dendritic cells and natural killer (NK) cells tended to be reduced in T/N-treated tumors compared to the control cohort (mean ± SD = 62.97% ± 9.99% for T/N vs. 54.36% ± 9.90% for control tumors). However, proportions of individual innate immune cell subpopulations remained very stable upon combinatorial treatment (Figure 16(F)), indicating little effect of the T/N combination therapy on innate anti-tumor immunity in T cell-deficient mice.

4 Discussion and outlook

PDAC is a highly heterogenous disease regarding both tumor cell-intrinsic and TME-specific features. Different molecular and morphological subtyping approaches have consistently identified a mesenchymal PDAC subtype with a particularly poor clinical prognosis and profound resistance to currently available treatment options, including chemotherapy, targeted therapies and immunotherapy (Aung et al., 2018; Chan-Seng-Yue et al., 2020; Morrison et al., 2018). While other classifications have focused on immune-related gene expression signatures (Wartenberg et al., 2018; Li et al., 2021; Chen et al., 2022), specific features of the immune microenvironment and tumor vasculature have not been linked to histopathological or molecular PDAC subtypes, despite representing a promising approach to uncover subtype-specific therapeutic vulnerabilities. The results presented in this study suggest that the mesenchymal PDAC subtype harbors a particularly immunosuppressive TME characterized by a lack of cytotoxic T cells and a dysfunctional tumor vasculature and that a novel combination therapy of trametinib and nintedanib shown to synergize *in vitro* and to prolong survival *in vivo* is able to reprogram the TME in a subtype-specific manner by increasing not only overall adaptive immune cell infiltration, but also the fraction of tumor-infiltrating $CD8^+$ cytotoxic T cells in the tumor core specifically in mesenchymal PDAC. The combinatorial treatment further induces multiple phenotypes of vascular remodeling specifically in mesenchymal PDAC, including morphological changes, vascular maturation and endothelial cell activation, possibly facilitating T cell infiltration into the tumor core. The observed T cell-mediated anti-tumor immunity significantly contributes to treatment efficacy *in vivo* as evidenced by a shortened survival benefit and higher tumor volumes in T cell-deficient compared to immunocompetent mesenchymal PDAC-bearing mice. The combination therapy thus represents a promising approach for treating this particularly aggressive form of PDAC.

4.1 The “cold” TME of mesenchymal mPDAC

Analysis of our endogenous $Kras^{G12D}$-driven mPDAC cohort revealed a particularly poor overall adaptive immune cell infiltration characterized by a relative abundance of regulatory and helper T cells in tumors of mesenchymal morphology. In a recent study on samples from surgically resected hPDAC, a similar “immune escape” phenotype was found to correlate with increased clusters of undifferentiated cells detached from the primary tumor mass (Wartenberg et al., 2018). This phenomenon termed tumor budding is associated with epithelial-mesenchymal transition and increased biological aggressiveness in PDAC and other cancer entities (Karamitopoulou et al., 2013). Furthermore, expression signatures and clinical characteristics of the immune escape phenotype showed considerable overlap with the basal-like, quasi-

mesenchymal subtype previously described (Wartenberg et al., 2018; Bailey et al., 2016b; Collisson et al., 2011), matching immunophenotyping and histopathological findings in our mPDAC cohort.

Besides individual TIL, aggregates of B and T cells with different organizational levels were present in the endogenous *Kras*^{G12D}-driven mPDAC cohort, including few TLS-like lymphocyte clusters shown to be associated with a favorable prognosis in hPDAC (Castino et al., 2016; Hiraoka et al., 2015). Unfortunately, we could not confirm that these structures were mature TLS as our multiplex immunofluorescence staining panel did not include specific markers for high endothelial venules or follicular dendritic cells which are essential components of fully formed and active TLS (Dieu-Nosjean et al., 2014). However, we were able to detect a higher abundance of mixed T and B cell clusters in classical than in mesenchymal mPDAC. Recent studies on PDAC and other cancer entities have suggested that these unorganized aggregates are precursors of TLS ("early-stage" TLS) which undergo a process of stage-wise maturation (Delvecchio et al., 2021; Posch et al., 2018; Siliņa et al., 2018). The lack of such lymphocyte clusters in mesenchymal tumors of our mPDAC cohort may thus reflect the inability to form mature TLS which potentially enhance anti-tumor immune cell priming, contributing to the inefficient recruitment and activation of TIL in this PDAC subtype. While the prognostic value of TLS for outcomes in PDAC patients has been described before (see above), Gunderson and colleagues have recently found a similar correlation to improved survival for early-stage TLS which were further associated with an increased $CD8^+$ T cell infiltration and enrichment of memory B and memory $CD4^+$ cells (Gunderson et al., 2021). These findings suggest that the formation of an immunological memory might also be impaired in mesenchymal PDAC, indicating the need of further functional investigations.

The extensive desmoplastic stroma of PDAC is generally believed to promote an immunosuppressive TME (Ho et al., 2020; Carvalho et al., 2021). However, we could show that lymphocyte clusters and individual tumor-infiltrating T cells which potentially mediate anti-tumor immunity were mainly located in stroma-rich regions of endogenous *Kras*^{G12D}-driven mPDAC, irrespective of the morphological subtype. Similar observations were made in hPDAC, with high stromal and low intraepithelial adaptive immune cell counts (Wartenberg et al., 2018), thus supporting the suitability of our mPDAC cohort to reflect spatial distribution of immune cell infiltration in hPDAC. Recently, Liudahl and colleagues conducted a comprehensive multiplex immunohistochemistry-based study on hPDAC to characterize immune infiltration across different histopathological tumor regions. While lymphoid and myeloid infiltrates demonstrated substantial intra- and intertumoral heterogeneity, the density of leukocytes in the tumor-adjacent stroma was found to correlate with the abundance of tumor-infiltrating leukocytes (Liudahl et al., 2021). These findings support the hypothesis that

the low stromal content of mesenchymal tumors represents one reason for the poor overall adaptive immune cell infiltration in this PDAC subtype, indicating that the tumor stroma can also adopt a tumor-restraining role by harboring immune cell populations which potentially mediate anti-tumor immunity.

The balance between different T cell subpopulations is a major determinant of tumor-related immune responses. Mesenchymal tumors from our endogenous *Kras^{G12D}*-driven mPDAC cohort were characterized by a relative predominance of CD4$^+$ T cells which frequently displayed a regulatory phenotype. The ratio of CD8$^+$ to CD4$^+$ T cells also showed substantial intratumoral heterogeneity, with differing CD8:CD4 ratios of classical and mesenchymal tumors particularly in regions of high tumor cellularity, highlighting the lack of tumor infiltrating CD8$^+$ cytotoxic T cells in mesenchymal PDAC. However, when comparing absolute lymphocyte counts, mesenchymal tumors demonstrated poor infiltration of both CD8$^+$ and CD4$^+$ T cells. While cytotoxic effector functions of CD8$^+$ T cells are well-described (Raskov et al., 2021), the significance of CD4$^+$ T cells in anti-tumor immune responses has not been recognized for a long time (Tay et al., 2021). However, besides providing help for CD8$^+$ cytotoxic T cells and B cells, thereby inducing both cellular and humoral immune responses (Tay et al., 2021; Borst et al., 2018), CD4$^+$ T cells themselves can adopt a cytotoxic effector phenotype with tumor-specific cytolytic activity as studies on other cancer entities have shown (Cachot et al., 2021; Oh et al., 2020; Matsuzaki et al., 2015). The lack of CD4$^+$ T cells might thus impede in multiple ways the generation of an effective anti-tumor immunity in mesenchymal PDAC.

Our multiplex immunofluorescence-based immunophenotyping approach offers a detailed insight into the interplay between immune cells, tumor cells and the tumor vasculature across different morphological subtypes of PDAC. However, additional tumors of *Kras^{G12D}* and other oncogenic backgrounds which are relevant in the genesis of PDAC must be analyzed to fully decipher and validate subtype-specific TME signatures. Furthermore, Kalimuthu and colleagues showed that a classification based morphological patterns correlates with molecular PDAC subtypes and clinical outcomes (Kalimuthu et al., 2020), supporting the rationale to classify endogenous *Kras^{G12D}*-driven mPDAC based on histopathological evaluation. However, co-existence of glandular and non-glandular components could be observed in some tumors, necessitating stratification based on the predominant morphological pattern and additional evaluation of tumor cell differentiation according to the classical grading system. This variable intratumoral heterogeneity could have contributed to the intertumoral variation of immune cell infiltration especially observed in the classical subtype. Combination with a gene expression-based subtyping approach might provide a more accurate classification, but the dichotomous system remains a problem considering the multifaceted

heterogeneity of PDAC. Grünwald and colleagues have recently proposed the concept of spatially confined sub-TMEs based on stromal and CAF morphology (Grünwald et al., 2021) which could also represent an approach to account for other features of histopathological heterogeneity such as tumor cell morphology and differentiation.

4.2 A combinatorial treatment that "warms up" the TME

Findings from our endogenous *Kras*^{G12D}-driven mPDAC cohort paint a clear picture of the "immune-desert" phenotype of mesenchymal PDAC, characterized by scarcity of CD8$^+$ cytotoxic T cells within the TME, while classical PDAC had more similarities to an "immune-excluded" phenotype, with TIL being mostly retained in the tumor stroma (Chen & Mellman, 2017). As the combination therapy of trametinib and nintedanib had been found to significantly prolong survival and reduce tumor growth in PDAC-bearing mice, with a superior response in the mesenchymal subtype (Falcomatà et al., 2022), we set out to investigate subtype-specific alterations of the TME in response to the combinatorial treatment, revealing an increased overall T cell infiltration in tumors of both subtypes. However, classical tumors still displayed an "immune-excluded" phenotype upon combinatorial treatment, with T cells being restricted to the invasive margins, matching the predominant spatial distribution of TIL in surgically resected treatment-naïve hPDAC as found in a recent multiplex immunohistochemistry-based study (Masugi et al., 2019). In contrast, the T/N combination therapy considerably increased the abundance of CD8$^+$ cytotoxic T cells infiltrating the tumor core of mesenchymal PDAC, indicating generation of anti-tumor adaptive immune responses which could significantly contribute to treatment efficacy in this PDAC subtype. In fact, a high CD8$^+$ T cell density in proximity to tumor cells respectively in the tumor core has been found to correlate with an increased survival of PDAC patients (Carstens et al., 2017; Masugi et al., 2019), highlighting the prognostic value of the infiltration pattern we observed in mesenchymal mPDAC upon combinatorial treatment. As our multiplex immunofluorescence-based immunophenotyping approach did not allow us to determine mechanisms leading to these changes in T cell infiltration, additional analyses of the tumor cell secretomes were conducted, revealing upregulation of specific chemokines upon combinatorial treatment, including CXCL16 which has been associated with enhanced TIL recruitment in various cancer entities (Falcomatà et al., 2022; Matsumura et al., 2008; Hojo et al., 2007). Previous studies have found that VEGF-directed anti-angiogenic drugs could enhance expression of CAMs (discussed below) and chemoattractants involved in T cell recruitment (Georganaki et al., 2018), suggesting that nintedanib might play a particularly important role in reprogramming of the TME into a T cell-enriched anti-tumorigenic niche.

We also noticed subtype-specific changes of tumor-infiltrating T cell subpopulations, including a trend towards an increased proportion of $CD8^+$ cytotoxic T cells among all T cells only in mesenchymal tumors. The relative abundance of this subpopulation compared to $CD4^+$ helper and regulatory T cells suggests that the combinatorial treatment specifically promotes anti-tumor immunity and limits differentiation of adaptive immune cells into immunosuppressive phenotypes. However, our multiplex immunofluorescence staining panel was not suitable to differentiate $CD4^+$ helper T cell subpopulations, notably Th1 and Th2 phenotypes with opposite tumor-related effector functions in hPDAC (Huber et al., 2020). Additional studies are thus required to determine whether the intratumoral Th1:Th2 ratio differs between classical and mesenchymal PDAC subtypes and whether the combinatorial treatment is able to shift the balance towards Th1, further boosting anti-tumor immune responses.

While the therapy response observed *in vivo* suggests that the T cells recruited upon combinatorial treatment could mediate an effective anti-tumor immunity and were not entirely "exhausted", our multiplex immunofluorescence-based immunophenotyping approach was not suitable to distinguish these functional phenotypes. To this end, single cell RNA sequencing and differential gene expression analysis were employed, revealing an increased abundance of functional cytotoxic, effector and memory T cells, upregulation of related signaling pathways as well as a reduced fraction of naïve T cell subpopulations specifically in the mesenchymal subtype (Falcomatà et al., 2022). To complement these studies, additional immuno-phenotyping via flow cytometry and multiplex immunofluorescence staining for immune checkpoint receptors, such as PD-1, CTLA-4 and TIGIT, and functional *in vitro* assays for cytolytic activity could be employed to assess the degree of T cell exhaustion that cytotoxic and effector T cells recruited upon combinatorial treatment display.

Furthermore, we observed an increased abundance of B cells upon combinatorial treatment in both PDAC subtypes, but only mesenchymal tumors displayed a higher density of mixed lymphocyte aggregates, likely reflecting improved inter-immune cell communication necessary for the generation of effective adaptive immune responses. However, we did not find any organized TLS-like clusters in orthotopically transplanted tumors. Delvecchio and colleagues have recently described a similar absence of fully formed TLS in tumors derived from orthotopic transplantation of a $Kras^{G12D};Trp53^{R172H}$-driven mPDAC cell line. They suspected that the critical mass of B cells required for initiation of intratumoral lymphoneogenesis is not reached in orthotopically transplanted tumors (Delvecchio et al., 2021). Indeed, despite the combinatorial treatment-induced increase, B cell counts were still relatively low, especially in the classical subtype. Further differentiation of functional B cell phenotypes and additional orthotopic transplantation experiments using mice which are genetically deficient or

iatrogenically depleted of B cells would be necessary to decipher the role of combinatorial treatment-induced B cell-mediated immune responses in therapy response.

Results from transplantation experiments using T cell-deficient *CD3ε-KO* mice suggest that combinatorial treatment-induced T cell recruitment is a key feature of therapy response in mesenchymal PDAC. While further studies are required to investigate underlying molecular mechanisms, recent evidence suggests that nintedanib might significantly contribute to this reprogramming of the TME. In a subcutaneous transplantation mouse model of melanoma, nintedanib was found to reduce tumor growth and to prolong survival without exerting direct cytotoxicity by increasing intratumoral $CD8^+$ cytotoxic T cell infiltration, which further sensitized the tumors to PD-1 blockade (Kato et al., 2021). However, we observed that T cell deficiency did not completely abolish *in vivo* response to the T/N combination therapy as survival times were still significantly longer and tumor volumes significantly decreased compared to the vehicle-treated cohort, suggesting that, besides direct inhibition of tumor cell proliferation via blockade of RAS signaling and T cell-mediated anti-tumor immunity, other TME-related factors might be involved. One distinctive feature was the increased abundance of B cells upon combinatorial treatment in mesenchymal tumors from both immunocompetent and T cell-deficient mice, with however significantly higher proportions of B cells in the latter. A higher baseline level of B cells in *CD3ε-KO* mice was excluded, in line with previously described findings (Ceredig, 2002). Instead, the spatial distribution of B cells within the tumor appeared to be altered upon T cell deficiency as evidenced by the accumulation within blood vessels and a complete lack of intratumoral B cell clusters, probably reflecting a dysfunctional B cell-mediated immunity. This would come as no surprise as the multifaceted crosstalk between T and B cells occurring in secondary lymphoid organs or TLS is essential for the generation of effective adaptive immune responses. However, anti-tumor immunity can also be achieved via T cell-independent activation of B cells inducing humoral immune responses (Largeot et al., 2019). Besides differentiation of functional B cell phenotypes, evaluation of total intratumoral immunoglobin concentrations and identification of tumor antigen-specific B cell receptors could thus be helpful to determine whether B cells in mesenchymal PDAC from both vehicle- and T/N-treated *CD3ε-KO* mice are functional after all.

The immunosuppressive TME is considered a key contributor to immunotherapy failure in PDAC as these therapeutic approaches rely on pre-existing tumor-infiltrating immune cells (Morrison et al., 2018; Tumeh et al., 2014; Herbst et al., 2014). It has been proposed before that the generation of strong adaptive immune responses in PDAC might represent a potent therapeutic strategy to overcome resistance to checkpoint inhibitors (Kabacaoglu et al., 2018), raising the question whether the substantially increased cytotoxic T cell infiltration we observed upon T/N treatment could sensitize mesenchymal PDAC towards immune checkpoint

blockade. Indeed, consequent studies revealed significantly improved outcomes in mesenchymal PDAC-bearing mice receiving a triple therapy of trametinib, nintedanib and anti-PD-L1 antibody (Falcomatà et al., 2022). Winograd and colleagues have demonstrated that the induction of a T cell-mediated anti-tumor immunity conferring sensitivity to immune checkpoint blockade can also be achieved by combining agonistic CD40 monoclonal antibodies and gemcitabine/nab-paclitaxel chemotherapy (Winograd et al., 2015). However, this experimental approach failed to account for subtype-specific responses. In contrast, our combinatorial treatment specifically targets the highly aggressive mesenchymal PDAC subtype characterized by profound resistance to hitherto available treatment options.

4.3 A combinatorial treatment that induces vascular remodeling

In a preclinical study on renal cell carcinoma, the combination of trametinib and the multikinase inhibitor sunitinib was found to reduce both tumor growth and tumor angiogenesis. While both agents demonstrated anti-angiogenic activity, the most effective inhibition of ERK phosphorylation in tumor endothelial cells was observed upon combinatorial treatment (Bridgeman et al., 2016). However, the results from our study suggest that the therapeutic effects of a similar combinatorial treatment strategy in mesenchymal PDAC go well beyond anti-angiogenesis. Besides the subtype-specific alterations of the immune microenvironment described above, the combinatorial treatment induced multiple levels of vascular remodeling specifically in mesenchymal PDAC. By increasing the proportion of blood vessels with open lumina, improving pericyte coverage of the microvasculature and enhancing P-selectin expression on endothelial cells, the combinatorial treatment significantly contributes to the normalization of a dysfunctional tumor vasculature, a process which might be an essential prerequisite for efficient intratumoral recruitment of cytotoxic T cells. The prognostic value of a functional and mature tumor vasculature in PDAC has recently been highlighted by Katsuta and colleagues who observed significantly longer overall survival times in PDAC patients with highly vascularized tumors which were further characterized by an increased expression of CAMs and vascular stability related genes, such as sphingosine 1-phosphate receptor-1 (S1PR1) and vascular endothelial cadherin, and by the upregulation of specific immune response related pathways, resulting in higher proportions of anti-tumorigenic adaptive immune cell populations and lower fractions of regulatory T cells (Katsuta et al., 2019). We observed that mesenchymal tumors displayed a similar correlation of a high density of vessels with open lumina and an increased T cell infiltration upon combinatorial treatment, while baseline vascularization and T cell infiltration of this PDAC subtype were predominantly low, matching substantially differing outcomes *in vivo*. Unfortunately, our multiplex immunofluorescence-based analysis does not allow the identification of potential mechanisms

by which an increased vessel opening could affect anti-tumor immune responses in PDAC. However, the relation between the microvasculature and anti-tumor immunity has been investigated before in multiple tumor models, leading to the current understanding that mechanical stress, such as excessive stromal proliferation or tumor growth, results in a compression of blood vessels, thus limiting perfusion and delivery of immune cells (Munn & Jain, 2019). Supposing that the increased proportion of blood vessels with visible lumina upon combinatorial treatment reflects an improved intratumoral perfusion pressure, it appears possible that the drug combination also acts by relieving mechanical stress on the tumor vasculature, most likely via restriction of tumor growth given the low stromal content of mesenchymal PDAC. This hypothetical mechanism of action could be synergistic with the ability of the combinatorial treatment to directly act on the tumor vasculature by increasing microvascular stability as evidenced by an increased proportion of pericyte-covered blood vessels. Further functional investigations including assessment of microvascular perfusion and immune cell extravasation are required to verify these hypotheses and might confer predictive value as an increased perfusion of the tumor vasculature has been predicted to improve response to checkpoint blockade immunotherapy (Mpekris et al., 2020), matching our observations that the combinatorial treatment increased sensitivity to PD-L1 blockade in mesenchymal PDAC *in vivo* (Falcomatà et al., 2022). Furthermore, selective cell surface proteomics of tumor endothelial cells could be employed to uncover additional pharmacodynamic mechanisms of the combinatorial treatment beyond inhibition of RTK related signaling. Among multiple potential targets, it would be particularly interesting to explore the effects of the combinatorial treatment on VCAM and S1PR1 expression in PDAC, as the upregulation of these receptors on tumor endothelial cells has been linked to an increased $CD8^+$ cytotoxic T cell infiltration (Ruscetti et al., 2020; Mlecnik et al., 2010) and to reduced branching and tortuosity of the tumor vasculature, enhanced pericyte coverage and increased sensitivity to PD-1 blockade (Gaengel et al., 2012; Cartier et al., 2020), respectively. Additionally, other elements of the tumor vascular architecture and functionality, such as branching patterns and endothelial barrier integrity, need to be characterized in order to determine whether our combinatorial treatment is able to fully induce vascular normalization in mesenchymal PDAC. To this end, our multiplex immunofluorescence staining panels could be applied in combination with three-dimensional confocal imaging. Cribaro and colleagues have recently demonstrated the potential of such techniques by creating fully characterized “vascular maps” of human glioblastomas, visualizing vascular density, blood vessel calibers, branching patterns, vessel wall integrity and immune cell extravasation, all in relation to the tumor mass (Cribaro et al., 2021).

4.4 Limitations of syngeneic orthotopic transplantation models of PDAC

The syngeneic orthotopic transplantation models of *Kras*^{G12D}-driven mPDAC we employed here are ideally suited for large-scale *in vivo* treatment studies as they can be established quickly without the need for resource-intensive breeding and are characterized by a short tumor latency and uniform disease progression as opposed to the protracted and variable clinical course of autochthonous mPDAC from GEMMs (Tseng et al., 2010). They are also considered to closely recapitulate biological aggressiveness, histopathological features and the immunosuppressive TME of hPDAC (Pham et al., 2021). However, we observed some morphological and TME-related differences between orthotopically transplanted and endogenous *Kras*^{G12D}-driven pancreatic tumors. Notably, classical tumors derived from orthotopic transplantation displayed much lower T and B cell infiltration, fewer lymphocyte clusters and less blood vessels with visible lumina than endogenous mPDAC of this subtype. Furthermore, we observed a significant correlation of T and B cell infiltration in endogenous, but not in orthotopically transplanted mPDAC. Spear and colleagues have recently described similar discrepancies in B cell infiltration of spontaneous and orthotopic *Kras*^{G12D}*;Trp53*^{R172H}-driven mPDAC models, further characterized by a lack of B cell activation, germinal center reaction and immunoglobulin production in orthotopically transplanted tumors (Spear et al., 2019). Besides the short tumor latency of only few days or weeks probably being not sufficient time for the generation of an adequate adaptive immune response (Spear et al., 2019), unique histopathological features of orthotopically transplanted tumors might also account for the relative paucity of TIL in the classical subtype. While classical tumors from our endogenous *Kras*^{G12D}-driven mPDAC cohort mostly displayed a conventional gland-forming morphology with surrounding desmoplastic stroma, orthotopically transplanted tumors of this subtype demonstrated a papillary gland-forming morphology with relatively high tumor cellularity and low stromal content, in line with previously described findings in orthotopic transplantation models of *Kras*^{G12D}*;Trp53*^{R172H}-driven mPDAC (Tseng et al., 2010; Majumder et al., 2016). Analysis of our endogenous mPDAC cohort had shown particularly poor adaptive immune cell infiltration and sparsity of blood vessels with open lumina in similar areas of high tumor cell density, matching stromal content, TIL abundance and microvasculature morphology in classical tumors derived from orthotopic transplantation. Consequently, considering the substantial discrepancies in stromal content and baseline lymphocytic infiltration, orthotopic transplantation models might also not sufficiently reflect combinatorial treatment-induced adaptive immune responses in classical PDAC. In contrast, mesenchymal tumors characterized by a particularly high tumor cellularity demonstrated very low baseline adaptive immune cell infiltration and equal proportions of blood vessels with visible lumina in both endogenous and orthotopic transplantation models, suggesting that the latter are able to

accurately recapitulate tumor cell-intrinsic and TME-specific features of this PDAC subtype. However, additional studies based on *Kras*^{G12D}-driven GEMMs of PDAC are necessary to validate *in vivo* therapy responses and to further investigate the impact of the combinatorial treatment on abundance and spatial distribution of adaptive immune cell infiltration, especially in classical PDAC.

4.5 Outlook

Together, our findings suggest that the combinatorial drug treatment fundamentally reshapes the immunologically “cold” TME of mesenchymal PDAC by promoting T cell-mediated anti-tumor immunity and vascular normalization. Additional studies in our group have demonstrated that this subtype-specific remodeling of the TME sets the basis for a substantially improved response to immune checkpoint blockade (Falcomatà et al., 2022), indicating a potential benefit of combining targeted therapy and immunotherapy in selected PDAC patients. The next step will be to validate subtype-specific immunophenotypes in a large cohort of molecularly annotated murine and human PDAC, with the ultimate objective to identify biomarkers predicting TME-related immune profiles which could be used for non-invasive stratification of PDAC patients. To further test the potency of our novel combinatorial treatment approach, mPDAC cell lines and GEMMs of different oncogenic backgrounds reflecting the molecular and biological heterogeneity of hPDAC will be employed for additional *in vivo* studies, paving the way for clinical investigations.

References

Ackermann, M., Kim, Y. O., Wagner, W. L., Schuppan, D., Valenzuela, C. D., Mentzer, S. J., Kreuz, S., Stiller, D., Wollin, L., & Konerding, M. A. (2017, Aug). Effects of nintedanib on the microvascular architecture in a lung fibrosis model. *Angiogenesis, 20*(3), 359-372. https://doi.org/10.1007/s10456-017-9543-z

Annese, T., Tamma, R., Ruggieri, S., & Ribatti, D. (2019, Mar 18). Angiogenesis in Pancreatic Cancer: Pre-Clinical and Clinical Studies. *Cancers (Basel), 11*(3). https://doi.org/10.3390/cancers11030381

Aung, K. L., Fischer, S. E., Denroche, R. E., Jang, G. H., Dodd, A., Creighton, S., Southwood, B., Liang, S. B., Chadwick, D., Zhang, A.*, et al.* (2018, Mar 15). Genomics-Driven Precision Medicine for Advanced Pancreatic Cancer: Early Results from the COMPASS Trial. *Clin Cancer Res, 24*(6), 1344-1354. https://doi.org/10.1158/1078-0432.Ccr-17-2994

Awasthi, N., Hinz, S., Brekken, R. A., Schwarz, M. A., & Schwarz, R. E. (2015, 2015/03/01/). Nintedanib, a triple angiokinase inhibitor, enhances cytotoxic therapy response in pancreatic cancer. *Cancer Letters, 358*(1), 59-66. https://doi.org/https://doi.org/10.1016/j.canlet.2014.12.027

Bailey, P., Chang, D. K., Forget, M. A., Lucas, F. A., Alvarez, H. A., Haymaker, C., Chattopadhyay, C., Kim, S. H., Ekmekcioglu, S., Grimm, E. A.*, et al.* (2016a, Oct 20). Exploiting the neoantigen landscape for immunotherapy of pancreatic ductal adenocarcinoma. *Sci Rep, 6*, 35848. https://doi.org/10.1038/srep35848

Bailey, P., Chang, D. K., Nones, K., Johns, A. L., Patch, A. M., Gingras, M. C., Miller, D. K., Christ, A. N., Bruxner, T. J., Quinn, M. C.*, et al.* (2016b, Mar 3). Genomic analyses identify molecular subtypes of pancreatic cancer. *Nature, 531*(7592), 47-52. https://doi.org/10.1038/nature16965

Baker, C. H., Solorzano, C. C., & Fidler, I. J. (2002, Apr 1). Blockade of vascular endothelial growth factor receptor and epidermal growth factor receptor signaling for therapy of metastatic human pancreatic cancer. *Cancer Res, 62*(7), 1996-2003.

Balli, D., Rech, A. J., Stanger, B. Z., & Vonderheide, R. H. (2017, Jun 15). Immune Cytolytic Activity Stratifies Molecular Subsets of Human Pancreatic Cancer. *Clin Cancer Res, 23*(12), 3129-3138. https://doi.org/10.1158/1078-0432.Ccr-16-2128

Balmanno, K., Chell, S. D., Gillings, A. S., Hayat, S., & Cook, S. J. (2009, Nov 15). Intrinsic resistance to the MEK1/2 inhibitor AZD6244 (ARRY-142886) is associated with weak ERK1/2 signalling and/or strong PI3K signalling in colorectal cancer cell lines. *Int J Cancer, 125*(10), 2332-2341. https://doi.org/10.1002/ijc.24604

Barău, A., Ruiz-Sauri, A., Valencia, G., Gómez-Mateo Mdel, C., Sabater, L., Ferrandez, A., & Llombart-Bosch, A. (2013, May). High microvessel density in pancreatic ductal adenocarcinoma is associated with high grade. *Virchows Arch, 462*(5), 541-546. https://doi.org/10.1007/s00428-013-1409-1

Bardeesy, N., & DePinho, R. A. (2002, Dec). Pancreatic cancer biology and genetics. *Nat Rev Cancer, 2*(12), 897-909. https://doi.org/10.1038/nrc949

Bergers, G., & Song, S. (2005, Oct). The role of pericytes in blood-vessel formation and maintenance. *Neuro-oncology, 7*(4), 452-464. https://doi.org/10.1215/s1152851705000232

Biankin, A. V., & Maitra, A. (2015, Oct 12). Subtyping Pancreatic Cancer. *Cancer Cell, 28*(4), 411-413. https://doi.org/10.1016/j.ccell.2015.09.020

Biankin, A. V., Waddell, N., Kassahn, K. S., Gingras, M. C., Muthuswamy, L. B., Johns, A. L., Miller, D. K., Wilson, P. J., Patch, A. M., Wu, J.*, et al.* (2012, Nov 15). Pancreatic cancer genomes reveal aberrations in axon guidance pathway genes. *Nature, 491*(7424), 399-405. https://doi.org/10.1038/nature11547

Blumenschein, G. R., Jr., Smit, E. F., Planchard, D., Kim, D. W., Cadranel, J., De Pas, T., Dunphy, F., Udud, K., Ahn, M. J., Hanna, N. H.*, et al.* (2015, May). A randomized phase II study of the MEK1/MEK2 inhibitor trametinib (GSK1120212) compared with docetaxel in KRAS-mutant advanced non-small-cell lung cancer (NSCLC)†. *Ann Oncol, 26*(5), 894-901. https://doi.org/10.1093/annonc/mdv072

Bodoky, G., Timcheva, C., Spigel, D. R., La Stella, P. J., Ciuleanu, T. E., Pover, G., & Tebbutt, N. C. (2012, 2012/06/01). A phase II open-label randomized study to assess the efficacy and safety of selumetinib (AZD6244 [ARRY-142886]) versus capecitabine in patients with advanced or metastatic pancreatic cancer who have failed first-line gemcitabine therapy. *Investigational New Drugs, 30*(3), 1216-1223. https://doi.org/10.1007/s10637-011-9687-4

Borst, J., Ahrends, T., Bąbała, N., Melief, C. J. M., & Kastenmüller, W. (2018, 2018/10/01). CD4+ T cell help in cancer immunology and immunotherapy. *Nature Reviews Immunology, 18*(10), 635-647. https://doi.org/10.1038/s41577-018-0044-0

Bosetti, C., Lucenteforte, E., Silverman, D. T., Petersen, G., Bracci, P. M., Ji, B. T., Negri, E., Li, D., Risch, H. A., Olson, S. H.*, et al.* (2012, Jul). Cigarette smoking and pancreatic cancer: an analysis from the International Pancreatic Cancer Case-Control Consortium (Panc4). *Ann Oncol, 23*(7), 1880-1888. https://doi.org/10.1093/annonc/mdr541

Bourne, H. R., Sanders, D. A., & McCormick, F. (1990, 1990/11/01). The GTPase superfamily: a conserved switch for diverse cell functions. *Nature, 348*(6297), 125-132. https://doi.org/10.1038/348125a0

Brahmer, J. R., Tykodi, S. S., Chow, L. Q., Hwu, W. J., Topalian, S. L., Hwu, P., Drake, C. G., Camacho, L. H., Kauh, J., Odunsi, K.*, et al.* (2012, Jun 28). Safety and activity of anti-PD-L1 antibody in patients with advanced cancer. *N Engl J Med, 366*(26), 2455-2465. https://doi.org/10.1056/NEJMoa1200694

Bridgeman, V. L., Wan, E., Foo, S., Nathan, M. R., Welti, J. C., Frentzas, S., Vermeulen, P. B., Preece, N., Springer, C. J., Powles, T.*, et al.* (2016, Jan). Preclinical Evidence That Trametinib Enhances the Response to Antiangiogenic Tyrosine Kinase Inhibitors in Renal Cell Carcinoma. *Mol Cancer Ther, 15*(1), 172-183. https://doi.org/10.1158/1535-7163.Mct-15-0170

Brunner, M., Maier, K., Rümmele, P., Jacobsen, A., Merkel, S., Benard, A., Krautz, C., Kersting, S., Grützmann, R., & Weber, G. F. (2020, Mar 5). Upregulation of CD20 Positive B-Cells and B-Cell Aggregates in the Tumor Infiltration Zone is Associated with Better Survival of Patients with Pancreatic Ductal Adenocarcinoma. *Int J Mol Sci, 21*(5). https://doi.org/10.3390/ijms21051779

Bruns, C. J., Shrader, M., Harbison, M. T., Portera, C., Solorzano, C. C., Jauch, K. W., Hicklin, D. J., Radinsky, R., & Ellis, L. M. (2002, Nov 10). Effect of the vascular endothelial growth factor receptor-2 antibody DC101 plus gemcitabine on growth, metastasis and angiogenesis of human pancreatic cancer growing orthotopically in nude mice. *Int J Cancer, 102*(2), 101-108. https://doi.org/10.1002/ijc.10681

Burris, H. A., 3rd, Moore, M. J., Andersen, J., Green, M. R., Rothenberg, M. L., Modiano, M. R., Cripps, M. C., Portenoy, R. K., Storniolo, A. M., Tarassoff, P.*, et al.* (1997, Jun). Improvements in survival and clinical benefit with gemcitabine as first-line therapy for patients with advanced pancreas cancer: a randomized trial. *J Clin Oncol, 15*(6), 2403-2413. https://doi.org/10.1200/jco.1997.15.6.2403

Cachot, A., Bilous, M., Liu, Y.-C., Li, X., Saillard, M., Cenerenti, M., Rockinger, G. A., Wyss, T., Guillaume, P., Schmidt, J.*, et al.* (2021). Tumor-specific cytolytic CD4 T cells mediate immunity against human cancer. *Science Advances, 7*(9), eabe3348. https://doi.org/doi:10.1126/sciadv.abe3348

Calle, E. E., Rodriguez, C., Walker-Thurmond, K., & Thun, M. J. (2003, Apr 24). Overweight, obesity, and mortality from cancer in a prospectively studied cohort of U.S. adults. *N Engl J Med, 348*(17), 1625-1638. https://doi.org/10.1056/NEJMoa021423

Cancer Genome Atlas Research Network. (2017, Aug 14). Integrated Genomic Characterization of Pancreatic Ductal Adenocarcinoma. *Cancer Cell, 32*(2), 185-203.e113. https://doi.org/10.1016/j.ccell.2017.07.007

Canon, J., Rex, K., Saiki, A. Y., Mohr, C., Cooke, K., Bagal, D., Gaida, K., Holt, T., Knutson, C. G., Koppada, N.*, et al.* (2019, Nov). The clinical KRAS(G12C) inhibitor AMG 510 drives anti-tumour immunity. *Nature, 575*(7781), 217-223. https://doi.org/10.1038/s41586-019-1694-1

Cargnello, M., & Roux, P. P. (2011, Mar). Activation and function of the MAPKs and their substrates, the MAPK-activated protein kinases. *Microbiol Mol Biol Rev, 75*(1), 50-83. https://doi.org/10.1128/mmbr.00031-10

Carmeliet, P., & Jain, R. K. (2011, May 19). Molecular mechanisms and clinical applications of angiogenesis. *Nature, 473*(7347), 298-307. https://doi.org/10.1038/nature10144

Carstens, J. L., Correa de Sampaio, P., Yang, D., Barua, S., Wang, H., Rao, A., Allison, J. P., LeBleu, V. S., & Kalluri, R. (2017, 2017/04/27). Spatial computation of intratumoral T cells correlates with survival of patients with pancreatic cancer. *Nature Communications, 8*(1), 15095. https://doi.org/10.1038/ncomms15095

Cartier, A., Leigh, T., Liu, C. H., & Hla, T. (2020). Endothelial sphingosine 1-phosphate receptors promote vascular normalization and antitumor therapy. *Proceedings of the National Academy of Sciences, 117*(6), 3157-3166. https://doi.org/10.1073/pnas.1906246117

Carvalho, T. M. A., Di Molfetta, D., Greco, M. R., Koltai, T., Alfarouk, K. O., Reshkin, S. J., & Cardone, R. A. (2021, Dec 6). Tumor Microenvironment Features and Chemoresistance in Pancreatic Ductal Adenocarcinoma: Insights into Targeting Physicochemical Barriers and Metabolism as Therapeutic Approaches. *Cancers (Basel), 13*(23). https://doi.org/10.3390/cancers13236135

Castino, G. F., Cortese, N., Capretti, G., Serio, S., Di Caro, G., Mineri, R., Magrini, E., Grizzi, F., Cappello, P., Novelli, F.*, et al.* (2016, Apr). Spatial distribution of B cells predicts prognosis in human pancreatic adenocarcinoma. *OncoImmunology, 5*(4), e1085147. https://doi.org/10.1080/2162402x.2015.1085147

Caunt, C. J., Sale, M. J., Smith, P. D., & Cook, S. J. (2015, Oct). MEK1 and MEK2 inhibitors and cancer therapy: the long and winding road. *Nat Rev Cancer, 15*(10), 577-592. https://doi.org/10.1038/nrc4000

Ceredig, R. (2002). The ontogeny of B cells in the thymus of normal, CD3ε knockout (KO), RAG-2 KO and IL-7 transgenic mice. *International Immunology, 14*(1), 87-99. https://doi.org/10.1093/intimm/14.1.87

Chan-Seng-Yue, M., Kim, J. C., Wilson, G. W., Ng, K., Figueroa, E. F., O'Kane, G. M., Connor, A. A., Denroche, R. E., Grant, R. C., McLeod, J.*, et al.* (2020, Feb). Transcription phenotypes of pancreatic cancer are driven by genomic events during tumor evolution. *Nat Genet, 52*(2), 231-240. https://doi.org/10.1038/s41588-019-0566-9

Chellappa, S., Hugenschmidt, H., Hagness, M., Line, P. D., Labori, K. J., Wiedswang, G., Taskén, K., & Aandahl, E. M. (2016, Apr). Regulatory T cells that co-express RORγt and FOXP3 are pro-inflammatory and immunosuppressive and expand in human pancreatic cancer. *OncoImmunology, 5*(4), e1102828. https://doi.org/10.1080/2162402x.2015.1102828

Chen, D. S., & Mellman, I. (2017, Jan 18). Elements of cancer immunity and the cancer-immune set point. *Nature, 541*(7637), 321-330. https://doi.org/10.1038/nature21349

Chen, S., Crabill, G. A., Pritchard, T. S., McMiller, T. L., Wei, P., Pardoll, D. M., Pan, F., & Topalian, S. L. (2019, Nov 15). Mechanisms regulating PD-L1 expression on tumor and immune cells. *J Immunother Cancer, 7*(1), 305. https://doi.org/10.1186/s40425-019-0770-2

Chen, Y., Chen, D., Wang, Q., Xu, Y., Huang, X., Haglund, F., & Su, H. (2022, 2022-January-17). Immunological Classification of Pancreatic Carcinomas to Identify Immune Index and Provide a Strategy for Patient Stratification [Original Research]. *Frontiers in Immunology, 12*. https://doi.org/10.3389/fimmu.2021.719105

Collisson, E. A., Sadanandam, A., Olson, P., Gibb, W. J., Truitt, M., Gu, S., Cooc, J., Weinkle, J., Kim, G. E., Jakkula, L.*, et al.* (2011, Apr). Subtypes of pancreatic ductal adenocarcinoma and their differing responses to therapy. *Nat Med, 17*(4), 500-503. https://doi.org/10.1038/nm.2344

Collisson, E. A., Trejo, C. L., Silva, J. M., Gu, S., Korkola, J. E., Heiser, L. M., Charles, R. P., Rabinovich, B. A., Hann, B., Dankort, D.*, et al.* (2012, Aug). A central role for RAF→MEK→ERK signaling in the genesis of pancreatic ductal adenocarcinoma. *Cancer Discov, 2*(8), 685-693. https://doi.org/10.1158/2159-8290.Cd-11-0347

Conroy, T., Desseigne, F., Ychou, M., Bouché, O., Guimbaud, R., Bécouarn, Y., Adenis, A., Raoul, J. L., Gourgou-Bourgade, S., de la Fouchardière, C.*, et al.* (2011, May 12). FOLFIRINOX versus gemcitabine for metastatic pancreatic cancer. *N Engl J Med, 364*(19), 1817-1825. https://doi.org/10.1056/NEJMoa1011923

Cribaro, G. P., Saavedra-López, E., Romarate, L., Mitxitorena, I., Díaz, L. R., Casanova, P. V., Roig-Martínez, M., Gallego, J. M., Perez-Vallés, A., & Barcia, C. (2021,

2021/02/12). Three-dimensional vascular microenvironment landscape in human glioblastoma. *Acta Neuropathologica Communications, 9*(1), 24. https://doi.org/10.1186/s40478-020-01115-0

Daemen, A., Peterson, D., Sahu, N., McCord, R., Du, X., Liu, B., Kowanetz, K., Hong, R., Moffat, J., Gao, M.*, et al.* (2015, Aug 11). Metabolite profiling stratifies pancreatic ductal adenocarcinomas into subtypes with distinct sensitivities to metabolic inhibitors. *Proc Natl Acad Sci U S A, 112*(32), E4410-4417. https://doi.org/10.1073/pnas.1501605112

Davies, H., Bignell, G. R., Cox, C., Stephens, P., Edkins, S., Clegg, S., Teague, J., Woffendin, H., Garnett, M. J., Bottomley, W.*, et al.* (2002, 2002/06/01). Mutations of the BRAF gene in human cancer. *Nature, 417*(6892), 949-954. https://doi.org/10.1038/nature00766

De La Cruz, M. S., Young, A. P., & Ruffin, M. T. (2014, Apr 15). Diagnosis and management of pancreatic cancer. *Am Fam Physician, 89*(8), 626-632.

De Monte, L., Reni, M., Tassi, E., Clavenna, D., Papa, I., Recalde, H., Braga, M., Di Carlo, V., Doglioni, C., & Protti, M. P. (2011, Mar 14). Intratumor T helper type 2 cell infiltrate correlates with cancer-associated fibroblast thymic stromal lymphopoietin production and reduced survival in pancreatic cancer. *J Exp Med, 208*(3), 469-478. https://doi.org/10.1084/jem.20101876

DeJarnette, J. B., Sommers, C. L., Huang, K., Woodside, K. J., Emmons, R., Katz, K., Shores, E. W., & Love, P. E. (1998, Dec 8). Specific requirement for CD3epsilon in T cell development. *Proc Natl Acad Sci U S A, 95*(25), 14909-14914. https://doi.org/10.1073/pnas.95.25.14909

Delvecchio, F. R., Fincham, R. E. A., Spear, S., Clear, A., Roy-Luzarraga, M., Balkwill, F. R., Gribben, J. G., Bombardieri, M., Hodivala-Dilke, K., Capasso, M.*, et al.* (2021). Pancreatic Cancer Chemotherapy Is Potentiated by Induction of Tertiary Lymphoid Structures in Mice. *Cellular and molecular gastroenterology and hepatology, 12*(5), 1543-1565. https://doi.org/10.1016/j.jcmgh.2021.06.023

Di Caro, G., Cortese, N., Castino, G. F., Grizzi, F., Gavazzi, F., Ridolfi, C., Capretti, G., Mineri, R., Todoric, J., Zerbi, A.*, et al.* (2016, Oct). Dual prognostic significance of tumour-associated macrophages in human pancreatic adenocarcinoma treated or untreated with chemotherapy. *Gut, 65*(10), 1710-1720. https://doi.org/10.1136/gutjnl-2015-309193

Dieu-Nosjean, M. C., Goc, J., Giraldo, N. A., Sautès-Fridman, C., & Fridman, W. H. (2014, Nov). Tertiary lymphoid structures in cancer and beyond. *Trends Immunol, 35*(11), 571-580. https://doi.org/10.1016/j.it.2014.09.006

Dijk, F., Veenstra, V. L., Soer, E. C., Dings, M. P. G., Zhao, L., Halfwerk, J. B., Hooijer, G. K., Damhofer, H., Marzano, M., Steins, A.*, et al.* (2020, Jan 15). Unsupervised class discovery in pancreatic ductal adenocarcinoma reveals cell-intrinsic mesenchymal features and high concordance between existing classification systems. *Sci Rep, 10*(1), 337. https://doi.org/10.1038/s41598-019-56826-9

Dougan, S. K. (2017, Nov/Dec). The Pancreatic Cancer Microenvironment. *Cancer J, 23*(6), 321-325. https://doi.org/10.1097/ppo.0000000000000288

Eser, S., Schnieke, A., Schneider, G., & Saur, D. (2014, Aug 26). Oncogenic KRAS signalling in pancreatic cancer. *Br J Cancer, 111*(5), 817-822. https://doi.org/10.1038/bjc.2014.215

Falcomatà, C., Bärthel, S., Widholz, S. A., Schneeweis, C., Montero, J. J., Toska, A., Mir, J., Kaltenbacher, T., Heetmeyer, J., Swietlik, J. J.*, et al.* (2022, 2022/01/31). Selective multi-kinase inhibition sensitizes mesenchymal pancreatic cancer to immune checkpoint blockade by remodeling the tumor microenvironment. *Nature Cancer*. https://doi.org/10.1038/s43018-021-00326-1

Ferlay, J., Partensky, C., & Bray, F. (2016, Sep-Oct). More deaths from pancreatic cancer than breast cancer in the EU by 2017. *Acta Oncol, 55*(9-10), 1158-1160. https://doi.org/10.1080/0284186x.2016.1197419

Foucher, E. D., Ghigo, C., Chouaib, S., Galon, J., Iovanna, J., & Olive, D. (2018). Pancreatic Ductal Adenocarcinoma: A Strong Imbalance of Good and Bad Immunological Cops in the Tumor Microenvironment. *Front Immunol, 9*, 1044. https://doi.org/10.3389/fimmu.2018.01044

Fujimoto, K., Hosotani, R., Wada, M., Lee, J. U., Koshiba, T., Miyamoto, Y., Tsuji, S., Nakajima, S., Doi, R., & Imamura, M. (1998, Aug). Expression of two angiogenic factors, vascular endothelial growth factor and platelet-derived endothelial cell growth factor in human pancreatic cancer, and its relationship to angiogenesis. *Eur J Cancer, 34*(9), 1439-1447. https://doi.org/10.1016/s0959-8049(98)00069-0

Fukunaga, A., Miyamoto, M., Cho, Y., Murakami, S., Kawarada, Y., Oshikiri, T., Kato, K., Kurokawa, T., Suzuoki, M., Nakakubo, Y.*, et al.* (2004). CD8+ Tumor-Infiltrating Lymphocytes Together with CD4+ Tumor-Infiltrating Lymphocytes and Dendritic Cells Improve the Prognosis of Patients with Pancreatic Adenocarcinoma. *Pancreas, 28*(1), e26-e31. https://journals.lww.com/pancreasjournal/Fulltext/2004/01000/CD8__Tumor_Infiltrating_Lymphocytes_Together_with.23.aspx

Gaengel, K., Niaudet, C., Hagikura, K., Laviña, B., Muhl, L., Hofmann, J. J., Ebarasi, L., Nyström, S., Rymo, S., Chen, L. L.*, et al.* (2012, Sep 11). The sphingosine-1-phosphate receptor S1PR1 restricts sprouting angiogenesis by regulating the interplay between VE-cadherin and VEGFR2. *Dev Cell, 23*(3), 587-599. https://doi.org/10.1016/j.devcel.2012.08.005

Georganaki, M., van Hooren, L., & Dimberg, A. (2018). Vascular Targeting to Increase the Efficiency of Immune Checkpoint Blockade in Cancer. *Front Immunol, 9*, 3081. https://doi.org/10.3389/fimmu.2018.03081

Gilmartin, A. G., Bleam, M. R., Groy, A., Moss, K. G., Minthorn, E. A., Kulkarni, S. G., Rominger, C. M., Erskine, S., Fisher, K. E., Yang, J.*, et al.* (2011, Mar 1). GSK1120212 (JTP-74057) is an inhibitor of MEK activity and activation with favorable pharmacokinetic properties for sustained in vivo pathway inhibition. *Clin Cancer Res, 17*(5), 989-1000. https://doi.org/10.1158/1078-0432.Ccr-10-2200

Group Young Researchers In Inflammatory Carcinogenesis, Wandmacher, A. M., Mehdorn, A. S., & Sebens, S. (2021, Sep 30). The Heterogeneity of the Tumor Microenvironment as Essential Determinant of Development, Progression and Therapy Response of Pancreatic Cancer. *Cancers (Basel), 13*(19). https://doi.org/10.3390/cancers13194932

Grünwald, B. T., Devisme, A., Andrieux, G., Vyas, F., Aliar, K., McCloskey, C. W., Macklin, A., Jang, G. H., Denroche, R., Romero, J. M.*, et al.* (2021, 2021/10/28/). Spatially confined sub-tumor microenvironments in pancreatic cancer. *Cell, 184*(22), 5577-5592.e5518. https://doi.org/https://doi.org/10.1016/j.cell.2021.09.022

Gunderson, A. J., Kaneda, M. M., Tsujikawa, T., Nguyen, A. V., Affara, N. I., Ruffell, B., Gorjestani, S., Liudahl, S. M., Truitt, M., Olson, P.*, et al.* (2016). Bruton Tyrosine Kinase–Dependent Immune Cell Cross-talk Drives Pancreas Cancer. *Cancer Discovery, 6*(3), 270-285. https://doi.org/10.1158/2159-8290.Cd-15-0827

Gunderson, A. J., Rajamanickam, V., Bui, C., Bernard, B., Pucilowska, J., Ballesteros-Merino, C., Schmidt, M., McCarty, K., Philips, M., Piening, B.*, et al.* (2021, Mar 17). Germinal center reactions in tertiary lymphoid structures associate with neoantigen burden, humoral immunity and long-term survivorship in pancreatic cancer. *OncoImmunology, 10*(1), 1900635. https://doi.org/10.1080/2162402x.2021.1900635

Hanahan, D., & Weinberg, R. A. (2011, Mar 4). Hallmarks of cancer: the next generation. *Cell, 144*(5), 646-674. https://doi.org/10.1016/j.cell.2011.02.013

Hanna, N. H., Kaiser, R., Sullivan, R. N., Aren, O. R., Ahn, M. J., Tiangco, B., Voccia, I., Pawel, J. V., Kovcin, V., Agulnik, J.*, et al.* (2016, Dec). Nintedanib plus pemetrexed versus placebo plus pemetrexed in patients with relapsed or refractory, advanced non-small cell lung cancer (LUME-Lung 2): A randomized, double-blind, phase III trial. *Lung Cancer, 102*, 65-73. https://doi.org/10.1016/j.lungcan.2016.10.011

Harjunpää, H., Llort Asens, M., Guenther, C., & Fagerholm, S. C. (2019). Cell Adhesion Molecules and Their Roles and Regulation in the Immune and Tumor Microenvironment. *Front Immunol, 10*, 1078. https://doi.org/10.3389/fimmu.2019.01078

Herbst, R. S., Soria, J. C., Kowanetz, M., Fine, G. D., Hamid, O., Gordon, M. S., Sosman, J. A., McDermott, D. F., Powderly, J. D., Gettinger, S. N.*, et al.* (2014, Nov 27). Predictive correlates of response to the anti-PD-L1 antibody MPDL3280A in cancer patients. *Nature, 515*(7528), 563-567. https://doi.org/10.1038/nature14011

Hida, K., Maishi, N., Annan, D. A., & Hida, Y. (2018, Apr 24). Contribution of Tumor Endothelial Cells in Cancer Progression. *Int J Mol Sci, 19*(5). https://doi.org/10.3390/ijms19051272

Hilberg, F., Roth, G. J., Krssak, M., Kautschitsch, S., Sommergruber, W., Tontsch-Grunt, U., Garin-Chesa, P., Bader, G., Zoephel, A., Quant, J.*, et al.* (2008, Jun 15). BIBF 1120: triple angiokinase inhibitor with sustained receptor blockade and good antitumor efficacy. *Cancer Res, 68*(12), 4774-4782. https://doi.org/10.1158/0008-5472.Can-07-6307

Hingorani, S. R., Petricoin, E. F., Maitra, A., Rajapakse, V., King, C., Jacobetz, M. A., Ross, S., Conrads, T. P., Veenstra, T. D., Hitt, B. A.*, et al.* (2003, Dec). Preinvasive and invasive ductal pancreatic cancer and its early detection in the mouse. *Cancer Cell, 4*(6), 437-450. https://doi.org/10.1016/s1535-6108(03)00309-x

Hingorani, S. R., Wang, L., Multani, A. S., Combs, C., Deramaudt, T. B., Hruban, R. H., Rustgi, A. K., Chang, S., & Tuveson, D. A. (2005, May). Trp53R172H and KrasG12D cooperate to promote chromosomal instability and widely metastatic pancreatic ductal adenocarcinoma in mice. *Cancer Cell, 7*(5), 469-483. https://doi.org/10.1016/j.ccr.2005.04.023

Hiraoka, N., Ino, Y., Yamazaki-Itoh, R., Kanai, Y., Kosuge, T., & Shimada, K. (2015, May 26). Intratumoral tertiary lymphoid organ is a favourable prognosticator in patients with pancreatic cancer. *Br J Cancer, 112*(11), 1782-1790. https://doi.org/10.1038/bjc.2015.145

Hiraoka, N., Onozato, K., Kosuge, T., & Hirohashi, S. (2006, Sep 15). Prevalence of FOXP3+ regulatory T cells increases during the progression of pancreatic ductal adenocarcinoma and its premalignant lesions. *Clin Cancer Res, 12*(18), 5423-5434. https://doi.org/10.1158/1078-0432.Ccr-06-0369

Ho, W. J., Jaffee, E. M., & Zheng, L. (2020, Sep). The tumour microenvironment in pancreatic cancer - clinical challenges and opportunities. *Nat Rev Clin Oncol, 17*(9), 527-540. https://doi.org/10.1038/s41571-020-0363-5

Hojo, S., Koizumi, K., Tsuneyama, K., Arita, Y., Cui, Z., Shinohara, K., Minami, T., Hashimoto, I., Nakayama, T., Sakurai, H.*, et al.* (2007, May 15). High-level expression of chemokine CXCL16 by tumor cells correlates with a good prognosis and increased tumor-infiltrating lymphocytes in colorectal cancer. *Cancer Res, 67*(10), 4725-4731. https://doi.org/10.1158/0008-5472.Can-06-3424

Hosein, A. N., Brekken, R. A., & Maitra, A. (2020, Aug). Pancreatic cancer stroma: an update on therapeutic targeting strategies. *Nat Rev Gastroenterol Hepatol, 17*(8), 487-505. https://doi.org/10.1038/s41575-020-0300-1

Hruban, R. H., Goggins, M., Parsons, J., & Kern, S. E. (2000). Progression Model for Pancreatic Cancer. *Clinical Cancer Research, 6*(8), 2969-2972. https://clincancerres.aacrjournals.org/content/clincanres/6/8/2969.full.pdf

Hu, H., Hang, J. J., Han, T., Zhuo, M., Jiao, F., & Wang, L. W. (2016, Jul). The M2 phenotype of tumor-associated macrophages in the stroma confers a poor prognosis in pancreatic cancer. *Tumour Biol, 37*(7), 8657-8664. https://doi.org/10.1007/s13277-015-4741-z

Huang, Y., Goel, S., Duda, D. G., Fukumura, D., & Jain, R. K. (2013). Vascular Normalization as an Emerging Strategy to Enhance Cancer Immunotherapy. *Cancer Research, 73*(10), 2943-2948. https://doi.org/10.1158/0008-5472.Can-12-4354

Huang, Y., Yuan, J., Righi, E., Kamoun, W. S., Ancukiewicz, M., Nezivar, J., Santosuosso, M., Martin, J. D., Martin, M. R., Vianello, F.*, et al.* (2012, Oct 23). Vascular normalizing doses of antiangiogenic treatment reprogram the immunosuppressive tumor microenvironment and enhance immunotherapy. *Proc Natl Acad Sci U S A, 109*(43), 17561-17566. https://doi.org/10.1073/pnas.1215397109

Huber, M., Brehm, C. U., Gress, T. M., Buchholz, M., Alashkar Alhamwe, B., von Strandmann, E. P., Slater, E. P., Bartsch, J. W., Bauer, C., & Lauth, M. (2020, Oct 3). The Immune Microenvironment in Pancreatic Cancer. *Int J Mol Sci, 21*(19). https://doi.org/10.3390/ijms21197307

Humphrey, E. S., Su, S. P., Nagrial, A. M., Hochgräfe, F., Pajic, M., Lehrbach, G. M., Parton, R. G., Yap, A. S., Horvath, L. G., Chang, D. K.*, et al.* (2016, Aug). Resolution of Novel Pancreatic Ductal Adenocarcinoma Subtypes by Global Phosphotyrosine Profiling. *Mol Cell Proteomics, 15*(8), 2671-2685. https://doi.org/10.1074/mcp.M116.058313

Hunt, B. J., & Jurd, K. M. (1998, May 2). Endothelial cell activation. A central pathophysiological process. *Bmj, 316*(7141), 1328-1329. https://doi.org/10.1136/bmj.316.7141.1328

Hunter, J. C., Manandhar, A., Carrasco, M. A., Gurbani, D., Gondi, S., & Westover, K. D. (2015). Biochemical and Structural Analysis of Common Cancer-Associated KRAS Mutations. *Molecular Cancer Research, 13*(9), 1325-1335. https://doi.org/10.1158/1541-7786.Mcr-15-0203

Huxley, R., Ansary-Moghaddam, A., Berrington de González, A., Barzi, F., & Woodward, M. (2005, Jun 6). Type-II diabetes and pancreatic cancer: a meta-analysis of 36 studies. *Br J Cancer, 92*(11), 2076-2083. https://doi.org/10.1038/sj.bjc.6602619

Iacobuzio-Donahue, C. A., Fu, B., Yachida, S., Luo, M., Abe, H., Henderson, C. M., Vilardell, F., Wang, Z., Keller, J. W., Banerjee, P.*, et al.* (2009, Apr 10). DPC4 gene status of the primary carcinoma correlates with patterns of failure in patients with pancreatic cancer. *J Clin Oncol, 27*(11), 1806-1813. https://doi.org/10.1200/jco.2008.17.7188

Ikemoto, T., Yamaguchi, T., Morine, Y., Imura, S., Soejima, Y., Fujii, M., Maekawa, Y., Yasutomo, K., & Shimada, M. (2006, Nov). Clinical roles of increased populations of Foxp3+CD4+ T cells in peripheral blood from advanced pancreatic cancer patients. *Pancreas, 33*(4), 386-390. https://doi.org/10.1097/01.mpa.0000240275.68279.13

Infante, J. R., Somer, B. G., Park, J. O., Li, C. P., Scheulen, M. E., Kasubhai, S. M., Oh, D. Y., Liu, Y., Redhu, S., Steplewski, K.*, et al.* (2014, Aug). A randomised, double-blind, placebo-controlled trial of trametinib, an oral MEK inhibitor, in combination with gemcitabine for patients with untreated metastatic adenocarcinoma of the pancreas. *Eur J Cancer, 50*(12), 2072-2081. https://doi.org/10.1016/j.ejca.2014.04.024

Ino, Y., Yamazaki-Itoh, R., Shimada, K., Iwasaki, M., Kosuge, T., Kanai, Y., & Hiraoka, N. (2013, Mar 5). Immune cell infiltration as an indicator of the immune microenvironment of pancreatic cancer. *Br J Cancer, 108*(4), 914-923. https://doi.org/10.1038/bjc.2013.32

Issa, Y., Nummer, D., Seibel, T., Müerköster, S. S., Koch, M., Schmitz-Winnenthal, F. H., Galindo, L., Weitz, J., Beckhove, P., & Altevogt, P. (2009, Jan). Enhanced L1CAM expression on pancreatic tumor endothelium mediates selective tumor cell transmigration. *J Mol Med (Berl), 87*(1), 99-112. https://doi.org/10.1007/s00109-008-0410-7

Itakura, J., Ishiwata, T., Friess, H., Fujii, H., Matsumoto, Y., Büchler, M. W., & Korc, M. (1997, Aug). Enhanced expression of vascular endothelial growth factor in human pancreatic cancer correlates with local disease progression. *Clin Cancer Res, 3*(8), 1309-1316.

Jackson, E. L., Willis, N., Mercer, K., Bronson, R. T., Crowley, D., Montoya, R., Jacks, T., & Tuveson, D. A. (2001, Dec 15). Analysis of lung tumor initiation and progression using conditional expression of oncogenic K-ras. *Genes Dev, 15*(24), 3243-3248. https://doi.org/10.1101/gad.943001

Jänne, P. A., Shaw, A. T., Pereira, J. R., Jeannin, G., Vansteenkiste, J., Barrios, C., Franke, F. A., Grinsted, L., Zazulina, V., Smith, P.*, et al.* (2013, Jan). Selumetinib plus docetaxel for KRAS-mutant advanced non-small-cell lung cancer: a randomised, multicentre, placebo-controlled, phase 2 study. *Lancet Oncol, 14*(1), 38-47. https://doi.org/10.1016/s1470-2045(12)70489-8

Jiang, B., Zhou, L., Lu, J., Wang, Y., Liu, C., You, L., & Guo, J. (2020, 2020-October-15). Stroma-Targeting Therapy in Pancreatic Cancer: One Coin With Two Sides? [Review]. *Frontiers in Oncology, 10*. https://doi.org/10.3389/fonc.2020.576399

Jones, S., Zhang, X., Parsons, D. W., Lin, J. C., Leary, R. J., Angenendt, P., Mankoo, P., Carter, H., Kamiyama, H., Jimeno, A.*, et al.* (2008, Sep 26). Core signaling pathways in human pancreatic cancers revealed by global genomic analyses. *Science, 321*(5897), 1801-1806. https://doi.org/10.1126/science.1164368

Kabacaoglu, D., Ciecielski, K. J., Ruess, D. A., & Algül, H. (2018, 2018-August-15). Immune Checkpoint Inhibition for Pancreatic Ductal Adenocarcinoma: Current Limitations and Future Options [Review]. *Frontiers in Immunology, 9*(1878). https://doi.org/10.3389/fimmu.2018.01878

Kalimuthu, S. N., Wilson, G. W., Grant, R. C., Seto, M., O'Kane, G., Vajpeyi, R., Notta, F., Gallinger, S., & Chetty, R. (2020, Feb). Morphological classification of pancreatic ductal adenocarcinoma that predicts molecular subtypes and correlates with clinical outcome. *Gut, 69*(2), 317-328. https://doi.org/10.1136/gutjnl-2019-318217

Karamitopoulou, E., Zlobec, I., Born, D., Kondi-Pafiti, A., Lykoudis, P., Mellou, A., Gennatas, K., Gloor, B., & Lugli, A. (2013, 2013/03/01/). Tumour budding is a strong and independent prognostic factor in pancreatic cancer. *European Journal of Cancer, 49*(5), 1032-1039. https://doi.org/https://doi.org/10.1016/j.ejca.2012.10.022

Kato, R., Haratani, K., Hayashi, H., Sakai, K., Sakai, H., Kawakami, H., Tanaka, K., Takeda, M., Yonesaka, K., Nishio, K.*, et al.* (2021, 2021/03/01). Nintedanib promotes antitumour immunity and shows antitumour activity in combination with PD-1 blockade in mice: potential role of cancer-associated fibroblasts. *British Journal of Cancer, 124*(5), 914-924. https://doi.org/10.1038/s41416-020-01201-z

Katsuta, E., Qi, Q., Peng, X., Hochwald, S. N., Yan, L., & Takabe, K. (2019, Feb 4). Pancreatic adenocarcinomas with mature blood vessels have better overall survival. *Sci Rep, 9*(1), 1310. https://doi.org/10.1038/s41598-018-37909-5

Kindler, H. L., Ioka, T., Richel, D. J., Bennouna, J., Létourneau, R., Okusaka, T., Funakoshi, A., Furuse, J., Park, Y. S., Ohkawa, S.*, et al.* (2011, Mar). Axitinib plus gemcitabine versus placebo plus gemcitabine in patients with advanced pancreatic adenocarcinoma: a double-blind randomised phase 3 study. *Lancet Oncol, 12*(3), 256-262. https://doi.org/10.1016/s1470-2045(11)70004-3

Kleeff, J., Korc, M., Apte, M., La Vecchia, C., Johnson, C. D., Biankin, A. V., Neale, R. E., Tempero, M., Tuveson, D. A., Hruban, R. H.*, et al.* (2016, Apr 21). Pancreatic cancer. *Nat Rev Dis Primers, 2*, 16022. https://doi.org/10.1038/nrdp.2016.22

Koyama, S., Ebihara, T., & Fukao, K. (1992, 1992/08/01). Expression of intercellular adhesion molecule 1 (ICAM-1) during the development of invasion and/or metastasis of gastric carcinoma. *Journal of Cancer Research and Clinical Oncology, 118*(8), 609-614. https://doi.org/10.1007/BF01211806

Krebs in Deutschland für 2017/2018. 13. Ausgabe. Robert Koch (Hrsg) und die Gesellschaft der epidemiologischen Krebsregister in Deutschland e.V. (Hrsg). (2021).

Largeot, A., Pagano, G., Gonder, S., Moussay, E., & Paggetti, J. (2019, May 13). The B-side of Cancer Immunity: The Underrated Tune. *Cells, 8*(5). https://doi.org/10.3390/cells8050449

Li, R., He, Y., Zhang, H., Wang, J., Liu, X., Liu, H., Wu, H., & Liang, Z. (2021, 2021-July-15). Identification and Validation of Immune Molecular Subtypes in Pancreatic Ductal Adenocarcinoma: Implications for Prognosis and Immunotherapy [Original Research]. *Frontiers in Immunology, 12*. https://doi.org/10.3389/fimmu.2021.690056

Liao, W., Lin, J. X., & Leonard, W. J. (2013, Jan 24). Interleukin-2 at the crossroads of effector responses, tolerance, and immunotherapy. *Immunity, 38*(1), 13-25. https://doi.org/10.1016/j.immuni.2013.01.004

Liu, X., Xu, J., Zhang, B., Liu, J., Liang, C., Meng, Q., Hua, J., Yu, X., & Shi, S. (2019, Dec 13). The reciprocal regulation between host tissue and immune cells in pancreatic ductal adenocarcinoma: new insights and therapeutic implications. *Mol Cancer, 18*(1), 184. https://doi.org/10.1186/s12943-019-1117-9

Liudahl, S. M., Betts, C. B., Sivagnanam, S., Morales-Oyarvide, V., da Silva, A., Yuan, C., Hwang, S., Grossblatt-Wait, A., Leis, K. R., Larson, W.*, et al.* (2021, Aug). Leukocyte Heterogeneity in Pancreatic Ductal Adenocarcinoma: Phenotypic and Spatial Features Associated with Clinical Outcome. *Cancer Discov, 11*(8), 2014-2031. https://doi.org/10.1158/2159-8290.Cd-20-0841

Llach, J., Carballal, S., & Moreira, L. (2020). Familial Pancreatic Cancer: Current Perspectives. *Cancer Manag Res, 12*, 743-758. https://doi.org/10.2147/cmar.S172421

Lorenzon, P., Vecile, E., Nardon, E., Ferrero, E., Harlan, J. M., Tedesco, F., & Dobrina, A. (1998, Sep 7). Endothelial cell E- and P-selectin and vascular cell adhesion molecule-1 function as signaling receptors. *J Cell Biol, 142*(5), 1381-1391. https://doi.org/10.1083/jcb.142.5.1381

Lowy, D. R., & Willumsen, B. M. (1993). Function and regulation of ras. *Annu Rev Biochem, 62*, 851-891. https://doi.org/10.1146/annurev.bi.62.070193.004223

Lugano, R., Ramachandran, M., & Dimberg, A. (2020, May). Tumor angiogenesis: causes, consequences, challenges and opportunities. *Cell Mol Life Sci, 77*(9), 1745-1770. https://doi.org/10.1007/s00018-019-03351-7

Lynch, S. M., Vrieling, A., Lubin, J. H., Kraft, P., Mendelsohn, J. B., Hartge, P., Canzian, F., Steplowski, E., Arslan, A. A., Gross, M.*, et al.* (2009, Aug 15). Cigarette smoking and pancreatic cancer: a pooled analysis from the pancreatic cancer cohort consortium. *Am J Epidemiol, 170*(4), 403-413. https://doi.org/10.1093/aje/kwp134

Mainardi, S., Mulero-Sánchez, A., Prahallad, A., Germano, G., Bosma, A., Krimpenfort, P., Lieftink, C., Steinberg, J. D., de Wit, N., Gonçalves-Ribeiro, S.*, et al.* (2018, Jul). SHP2 is required for growth of KRAS-mutant non-small-cell lung cancer in vivo. *Nat Med, 24*(7), 961-967. https://doi.org/10.1038/s41591-018-0023-9

Majumder, K., Arora, N., Modi, S., Chugh, R., Nomura, A., Giri, B., Dawra, R., Ramakrishnan, S., Banerjee, S., Saluja, A.*, et al.* (2016, Jan). A Novel Immunocompetent Mouse Model of Pancreatic Cancer with Robust Stroma: a Valuable Tool for Preclinical Evaluation of New Therapies. *J Gastrointest Surg, 20*(1), 53-65; discussion 65. https://doi.org/10.1007/s11605-015-2985-y

Mandal, R., Becker, S., & Strebhardt, K. (2016, 2016/05/01). Stamping out RAF and MEK1/2 to inhibit the ERK1/2 pathway: an emerging threat to anticancer therapy. *Oncogene, 35*(20), 2547-2561. https://doi.org/10.1038/onc.2015.329

Manji, G. A., Olive, K. P., Saenger, Y. M., & Oberstein, P. (2017, Apr 1). Current and Emerging Therapies in Metastatic Pancreatic Cancer. *Clin Cancer Res, 23*(7), 1670-1678. https://doi.org/10.1158/1078-0432.Ccr-16-2319

Manzo, A., Carillio, G., Montanino, A., Costanzo, R., Sandomenico, C., Rocco, G., & Morabito, A. (2016). Focus on Nintedanib in NSCLC and Other Tumors. *Front Med (Lausanne), 3*, 68. https://doi.org/10.3389/fmed.2016.00068

Masugi, Y., Abe, T., Ueno, A., Fujii-Nishimura, Y., Ojima, H., Endo, Y., Fujita, Y., Kitago, M., Shinoda, M., Kitagawa, Y.*, et al.* (2019, Oct). Characterization of spatial distribution of tumor-infiltrating CD8(+) T cells refines their prognostic utility for pancreatic cancer survival. *Mod Pathol, 32*(10), 1495-1507. https://doi.org/10.1038/s41379-019-0291-z

Matsumura, S., Wang, B., Kawashima, N., Braunstein, S., Badura, M., Cameron, T. O., Babb, J. S., Schneider, R. J., Formenti, S. C., Dustin, M. L.*, et al.* (2008, Sep 1). Radiation-induced CXCL16 release by breast cancer cells attracts effector T cells. *J Immunol, 181*(5), 3099-3107. https://doi.org/10.4049/jimmunol.181.5.3099

Matsuzaki, J., Tsuji, T., Luescher, I. F., Shiku, H., Mineno, J., Okamoto, S., Old, L. J., Shrikant, P., Gnjatic, S., & Odunsi, K. (2015, 2015/10/08). Direct tumor recognition by a human CD4+ T-cell subset potently mediates tumor growth inhibition and orchestrates anti-tumor immune responses. *Scientific Reports, 5*(1), 14896. https://doi.org/10.1038/srep14896

McLane, L. M., Abdel-Hakeem, M. S., & Wherry, E. J. (2019). CD8 T Cell Exhaustion During Chronic Viral Infection and Cancer. *Annual Review of Immunology, 37*(1), 457-495. https://doi.org/10.1146/annurev-immunol-041015-055318

Mirzoeva, O. K., Collisson, E. A., Schaefer, P. M., Hann, B., Hom, Y. K., Ko, A. H., & Korn, W. M. (2013, Oct). Subtype-specific MEK-PI3 kinase feedback as a therapeutic target in pancreatic adenocarcinoma. *Mol Cancer Ther, 12*(10), 2213-2225. https://doi.org/10.1158/1535-7163.Mct-13-0104

Mittrücker, H. W., Visekruna, A., & Huber, M. (2014, Dec). Heterogeneity in the differentiation and function of $CD8^+$ T cells. *Arch Immunol Ther Exp (Warsz), 62*(6), 449-458. https://doi.org/10.1007/s00005-014-0293-y

Mizrahi, J. D., Surana, R., Valle, J. W., & Shroff, R. T. (2020, Jun 27). Pancreatic cancer. *Lancet, 395*(10242), 2008-2020. https://doi.org/10.1016/s0140-6736(20)30974-0

Mlecnik, B., Tosolini, M., Charoentong, P., Kirilovsky, A., Bindea, G., Berger, A., Camus, M., Gillard, M., Bruneval, P., Fridman, W. H.*, et al.* (2010, Apr). Biomolecular network reconstruction identifies T-cell homing factors associated with survival in colorectal cancer. *Gastroenterology, 138*(4), 1429-1440. https://doi.org/10.1053/j.gastro.2009.10.057

Moffitt, R. A., Marayati, R., Flate, E. L., Volmar, K. E., Loeza, S. G. H., Hoadley, K. A., Rashid, N. U., Williams, L. A., Eaton, S. C., Chung, A. H.*, et al.* (2015, 2015/10/01). Virtual microdissection identifies distinct tumor- and stroma-specific subtypes of pancreatic

ductal adenocarcinoma. *Nature Genetics, 47*(10), 1168-1178. https://doi.org/10.1038/ng.3398

Moore, A. R., Rosenberg, S. C., McCormick, F., & Malek, S. (2020, Aug). RAS-targeted therapies: is the undruggable drugged? *Nat Rev Drug Discov, 19*(8), 533-552. https://doi.org/10.1038/s41573-020-0068-6

Morohoshi, T., Held, G., & Klöppel, G. (1983, Sep). Exocrine pancreatic tumours and their histological classification. A study based on 167 autopsy and 97 surgical cases. *Histopathology, 7*(5), 645-661. https://doi.org/10.1111/j.1365-2559.1983.tb02277.x

Morrison, A. H., Byrne, K. T., & Vonderheide, R. H. (2018, Jun). Immunotherapy and Prevention of Pancreatic Cancer. *Trends Cancer, 4*(6), 418-428. https://doi.org/10.1016/j.trecan.2018.04.001

Mpekris, F., Voutouri, C., Baish, J. W., Duda, D. G., Munn, L. L., Stylianopoulos, T., & Jain, R. K. (2020). Combining microenvironment normalization strategies to improve cancer immunotherapy. *Proceedings of the National Academy of Sciences, 117*(7), 3728-3737. https://doi.org/10.1073/pnas.1919764117

Mueller, S., Engleitner, T., Maresch, R., Zukowska, M., Lange, S., Kaltenbacher, T., Konukiewitz, B., Öllinger, R., Zwiebel, M., Strong, A.*, et al.* (2018, Feb 1). Evolutionary routes and KRAS dosage define pancreatic cancer phenotypes. *Nature, 554*(7690), 62-68. https://doi.org/10.1038/nature25459

Munn, L. L., & Jain, R. K. (2019). Vascular regulation of antitumor immunity. *Science, 365*(6453), 544-545.

Nagy, J. A., Dvorak, A. M., & Dvorak, H. F. (2012, Feb). Vascular hyperpermeability, angiogenesis, and stroma generation. *Cold Spring Harb Perspect Med, 2*(2), a006544. https://doi.org/10.1101/cshperspect.a006544

Nakhai, H., Sel, S., Favor, J., Mendoza-Torres, L., Paulsen, F., Duncker, G. I., & Schmid, R. M. (2007, Mar). Ptf1a is essential for the differentiation of GABAergic and glycinergic amacrine cells and horizontal cells in the mouse retina. *Development, 134*(6), 1151-1160. https://doi.org/10.1242/dev.02781

Neesse, A., Bauer, C. A., Öhlund, D., Lauth, M., Buchholz, M., Michl, P., Tuveson, D. A., & Gress, T. M. (2019, Jan). Stromal biology and therapy in pancreatic cancer: ready for clinical translation? *Gut, 68*(1), 159-171. https://doi.org/10.1136/gutjnl-2018-316451

Neoptolemos, J. P., Stocken, D. D., Friess, H., Bassi, C., Dunn, J. A., Hickey, H., Beger, H., Fernandez-Cruz, L., Dervenis, C., Lacaine, F.*, et al.* (2004). A Randomized Trial of Chemoradiotherapy and Chemotherapy after Resection of Pancreatic Cancer. *New England Journal of Medicine, 350*(12), 1200-1210. https://doi.org/10.1056/NEJMoa032295

Nishida, N., Yano, H., Nishida, T., Kamura, T., & Kojiro, M. (2006). Angiogenesis in cancer. *Vasc Health Risk Manag, 2*(3), 213-219. https://doi.org/10.2147/vhrm.2006.2.3.213

Noman, M. Z., Hasmim, M., Messai, Y., Terry, S., Kieda, C., Janji, B., & Chouaib, S. (2015, Nov 1). Hypoxia: a key player in antitumor immune response. A Review in the Theme: Cellular Responses to Hypoxia. *Am J Physiol Cell Physiol, 309*(9), C569-579. https://doi.org/10.1152/ajpcell.00207.2015

Notta, F., Zandi, S., Takayama, N., Dobson, S., Gan, O. I., Wilson, G., Kaufmann, K. B., McLeod, J., Laurenti, E., Dunant, C. F.*, et al.* (2016, Jan 8). Distinct routes of lineage development reshape the human blood hierarchy across ontogeny. *Science, 351*(6269), aab2116. https://doi.org/10.1126/science.aab2116

Nummer, D., Suri-Payer, E., Schmitz-Winnenthal, H., Bonertz, A., Galindo, L., Antolovich, D., Koch, M., Büchler, M., Weitz, J., Schirrmacher, V.*, et al.* (2007, Aug 1). Role of tumor endothelium in CD4+ CD25+ regulatory T cell infiltration of human pancreatic carcinoma. *J Natl Cancer Inst, 99*(15), 1188-1199. https://doi.org/10.1093/jnci/djm064

O'Reilly, E. M., Niedzwiecki, D., Hall, M., Hollis, D., Bekaii-Saab, T., Pluard, T., Douglas, K., Abou-Alfa, G. K., Kindler, H. L., Schilsky, R. L.*, et al.* (2010). A Cancer and Leukemia Group B Phase II Study of Sunitinib Malate in Patients with Previously Treated Metastatic Pancreatic Adenocarcinoma (CALGB 80603). *The Oncologist, 15*(12), 1310-1319. https://doi.org/10.1634/theoncologist.2010-0152

O'Reilly, E. M., Oh, D. Y., Dhani, N., Renouf, D. J., Lee, M. A., Sun, W., Fisher, G., Hezel, A., Chang, S. C., Vlahovic, G.*, et al.* (2019, Oct 1). Durvalumab With or Without Tremelimumab for Patients With Metastatic Pancreatic Ductal Adenocarcinoma: A Phase 2 Randomized Clinical Trial. *JAMA oncology, 5*(10), 1431-1438. https://doi.org/10.1001/jamaoncol.2019.1588

Oettle, H., Neuhaus, P., Hochhaus, A., Hartmann, J. T., Gellert, K., Ridwelski, K., Niedergethmann, M., Zülke, C., Fahlke, J., Arning, M. B.*, et al.* (2013). Adjuvant Chemotherapy With Gemcitabine and Long-term Outcomes Among Patients With Resected Pancreatic Cancer: The CONKO-001 Randomized Trial. *JAMA, 310*(14), 1473-1481. https://doi.org/10.1001/jama.2013.279201

Ogawa, Y., Hirakawa, K., Nakata, B., Fujihara, T., Sawada, T., Kato, Y., Yoshikawa, K., & Sowa, M. (1998, Jan). Expression of intercellular adhesion molecule-1 in invasive breast cancer reflects low growth potential, negative lymph node involvement, and good prognosis. *Clin Cancer Res, 4*(1), 31-36.

Oh, D. Y., Kwek, S. S., Raju, S. S., Li, T., McCarthy, E., Chow, E., Aran, D., Ilano, A., Pai, C.-C. S., Rancan, C.*, et al.* (2020). Intratumoral CD4+ T Cells Mediate Anti-tumor Cytotoxicity in Human Bladder Cancer. *Cell, 181*(7), 1612-1625.e1613. https://doi.org/10.1016/j.cell.2020.05.017

Olive, K. P., Jacobetz, M. A., Davidson, C. J., Gopinathan, A., McIntyre, D., Honess, D., Madhu, B., Goldgraben, M. A., Caldwell, M. E., Allard, D.*, et al.* (2009, Jun 12). Inhibition of Hedgehog signaling enhances delivery of chemotherapy in a mouse model of pancreatic cancer. *Science, 324*(5933), 1457-1461. https://doi.org/10.1126/science.1171362

Olive, K. P., Tuveson, D. A., Ruhe, Z. C., Yin, B., Willis, N. A., Bronson, R. T., Crowley, D., & Jacks, T. (2004). Mutant p53 Gain of Function in Two Mouse Models of Li-Fraumeni Syndrome. *Cell, 119*(6), 847-860. https://doi.org/10.1016/j.cell.2004.11.004

Orth, M., Metzger, P., Gerum, S., Mayerle, J., Schneider, G., Belka, C., Schnurr, M., & Lauber, K. (2019, Aug 8). Pancreatic ductal adenocarcinoma: biological hallmarks, current status, and future perspectives of combined modality treatment approaches. *Radiat Oncol, 14*(1), 141. https://doi.org/10.1186/s13014-019-1345-6

Ostrem, J. M., Peters, U., Sos, M. L., Wells, J. A., & Shokat, K. M. (2013, Nov 28). K-Ras(G12C) inhibitors allosterically control GTP affinity and effector interactions. *Nature, 503*(7477), 548-551. https://doi.org/10.1038/nature12796

Özdemir, Berna C., Pentcheva-Hoang, T., Carstens, Julienne L., Zheng, X., Wu, C.-C., Simpson, Tyler R., Laklai, H., Sugimoto, H., Kahlert, C., Novitskiy, Sergey V.*, et al.* (2014). Depletion of Carcinoma-Associated Fibroblasts and Fibrosis Induces Immunosuppression and Accelerates Pancreas Cancer with Reduced Survival. *Cancer Cell, 25*(6), 719-734. https://doi.org/10.1016/j.ccr.2014.04.005

Papetti, M., & Herman, I. M. (2002). Mechanisms of normal and tumor-derived angiogenesis. *American Journal of Physiology-Cell Physiology, 282*(5), C947-C970. https://doi.org/10.1152/ajpcell.00389.2001

Permuth-Wey, J., & Egan, K. M. (2009). Family history is a significant risk factor for pancreatic cancer: results from a systematic review and meta-analysis. *Fam Cancer, 8*(2), 109-117. https://doi.org/10.1007/s10689-008-9214-8

Pettazzoni, P., Viale, A., Shah, P., Carugo, A., Ying, H., Wang, H., Genovese, G., Seth, S., Minelli, R., Green, T.*, et al.* (2015). Genetic Events That Limit the Efficacy of MEK and RTK Inhibitor Therapies in a Mouse Model of KRAS-Driven Pancreatic Cancer. *Cancer Research, 75*(6), 1091-1101. https://doi.org/10.1158/0008-5472.Can-14-1854

Pham, T. N. D., Shields, M. A., Spaulding, C., Principe, D. R., Li, B., Underwood, P. W., Trevino, J. G., Bentrem, D. J., & Munshi, H. G. (2021, Jan 25). Preclinical Models of Pancreatic Ductal Adenocarcinoma and Their Utility in Immunotherapy Studies. *Cancers (Basel), 13*(3). https://doi.org/10.3390/cancers13030440

Planchard, D., Smit, E. F., Groen, H. J. M., Mazieres, J., Besse, B., Helland, Å., Giannone, V., D'Amelio, A. M., Jr., Zhang, P., Mookerjee, B.*, et al.* (2017, Oct). Dabrafenib plus trametinib in patients with previously untreated BRAF(V600E)-mutant metastatic non-small-cell lung cancer: an open-label, phase 2 trial. *Lancet Oncol, 18*(10), 1307-1316. https://doi.org/10.1016/s1470-2045(17)30679-4

Posch, F., Silina, K., Leibl, S., Mündlein, A., Moch, H., Siebenhüner, A., Samaras, P., Riedl, J., Stotz, M., Szkandera, J.*, et al.* (2018). Maturation of tertiary lymphoid structures and recurrence of stage II and III colorectal cancer. *OncoImmunology, 7*(2), e1378844. https://doi.org/10.1080/2162402x.2017.1378844

Provenzano, P. P., Cuevas, C., Chang, A. E., Goel, V. K., Von Hoff, D. D., & Hingorani, S. R. (2012, Mar 20). Enzymatic targeting of the stroma ablates physical barriers to treatment of pancreatic ductal adenocarcinoma. *Cancer Cell, 21*(3), 418-429. https://doi.org/10.1016/j.ccr.2012.01.007

Pylayeva-Gupta, Y., Das, S., Handler, J. S., Hajdu, C. H., Coffre, M., Koralov, S. B., & Bar-Sagi, D. (2016). IL35-Producing B Cells Promote the Development of Pancreatic Neoplasia. *Cancer Discovery, 6*(3), 247-255. https://doi.org/10.1158/2159-8290.Cd-15-0843

Pylayeva-Gupta, Y., Grabocka, E., & Bar-Sagi, D. (2011, Oct 13). RAS oncogenes: weaving a tumorigenic web. *Nat Rev Cancer, 11*(11), 761-774. https://doi.org/10.1038/nrc3106

Quante, A. S., Ming, C., Rottmann, M., Engel, J., Boeck, S., Heinemann, V., Westphalen, C. B., & Strauch, K. (2016, Sep). Projections of cancer incidence and cancer-related

deaths in Germany by 2020 and 2030. *Cancer Med, 5*(9), 2649-2656. https://doi.org/10.1002/cam4.767

Rahn, S., Zimmermann, V., Viol, F., Knaack, H., Stemmer, K., Peters, L., Lenk, L., Ungefroren, H., Saur, D., Schäfer, H.*, et al.* (2018, Feb 28). Diabetes as risk factor for pancreatic cancer: Hyperglycemia promotes epithelial-mesenchymal-transition and stem cell properties in pancreatic ductal epithelial cells. *Cancer Lett, 415*, 129-150. https://doi.org/10.1016/j.canlet.2017.12.004

Raimondi, S., Lowenfels, A. B., Morselli-Labate, A. M., Maisonneuve, P., & Pezzilli, R. (2010, Jun). Pancreatic cancer in chronic pancreatitis; aetiology, incidence, and early detection. *Best Pract Res Clin Gastroenterol, 24*(3), 349-358. https://doi.org/10.1016/j.bpg.2010.02.007

Raskov, H., Orhan, A., Christensen, J. P., & Gögenur, I. (2021, 2021/01/01). Cytotoxic CD8+ T cells in cancer and cancer immunotherapy. *British Journal of Cancer, 124*(2), 359-367. https://doi.org/10.1038/s41416-020-01048-4

Rawla, P., Sunkara, T., & Gaduputi, V. (2019, Feb). Epidemiology of Pancreatic Cancer: Global Trends, Etiology and Risk Factors. *World J Oncol, 10*(1), 10-27. https://doi.org/10.14740/wjon1166

Ray-Coquard, I., Cibula, D., Mirza, M. R., Reuss, A., Ricci, C., Colombo, N., Koch, H., Goffin, F., González-Martin, A., Ottevanger, P. B.*, et al.* (2020, Jan 15). Final results from GCIG/ENGOT/AGO-OVAR 12, a randomised placebo-controlled phase III trial of nintedanib combined with chemotherapy for newly diagnosed advanced ovarian cancer. *Int J Cancer, 146*(2), 439-448. https://doi.org/10.1002/ijc.32606

Reck, M., Kaiser, R., Mellemgaard, A., Douillard, J.-Y., Orlov, S., Krzakowski, M., von Pawel, J., Gottfried, M., Bondarenko, I., Liao, M.*, et al.* (2014). Docetaxel plus nintedanib versus docetaxel plus placebo in patients with previously treated non-small-cell lung cancer (LUME-Lung 1): a phase 3, double-blind, randomised controlled trial. *The Lancet Oncology, 15*(2), 143-155. https://doi.org/10.1016/S1470-2045(13)70586-2

Rhim, A. D., Oberstein, P. E., Thomas, D. H., Mirek, E. T., Palermo, C. F., Sastra, S. A., Dekleva, E. N., Saunders, T., Becerra, C. P., Tattersall, I. W.*, et al.* (2014, Jun 16). Stromal elements act to restrain, rather than support, pancreatic ductal adenocarcinoma. *Cancer Cell, 25*(6), 735-747. https://doi.org/10.1016/j.ccr.2014.04.021

Ribatti, D., Nico, B., & Crivellato, E. (2011). The role of pericytes in angiogenesis. *Int J Dev Biol, 55*(3), 261-268. https://doi.org/10.1387/ijdb.103167dr

Richeldi, L., du Bois, R. M., Raghu, G., Azuma, A., Brown, K. K., Costabel, U., Cottin, V., Flaherty, K. R., Hansell, D. M., Inoue, Y.*, et al.* (2014, May 29). Efficacy and safety of nintedanib in idiopathic pulmonary fibrosis. *N Engl J Med, 370*(22), 2071-2082. https://doi.org/10.1056/NEJMoa1402584

Roeder, F. (2016, Feb 15). Neoadjuvant radiotherapeutic strategies in pancreatic cancer. *World J Gastrointest Oncol, 8*(2), 186-197. https://doi.org/10.4251/wjgo.v8.i2.186

Royal, R. E., Levy, C., Turner, K., Mathur, A., Hughes, M., Kammula, U. S., Sherry, R. M., Topalian, S. L., Yang, J. C., Lowy, I.*, et al.* (2010). Phase 2 Trial of Single Agent Ipilimumab (Anti-CTLA-4) for Locally Advanced or Metastatic Pancreatic

Adenocarcinoma. *Journal of Immunotherapy, 33*(8). https://journals.lww.com/immunotherapy-journal/Fulltext/2010/10000/Phase_2_Trial_of_Single_Agent_Ipilimumab.9.aspx

Ruess, D. A., Heynen, G. J., Ciecielski, K. J., Ai, J., Berninger, A., Kabacaoglu, D., Görgülü, K., Dantes, Z., Wörmann, S. M., Diakopoulos, K. N.*, et al.* (2018, Jul). Mutant KRAS-driven cancers depend on PTPN11/SHP2 phosphatase. *Nat Med, 24*(7), 954-960. https://doi.org/10.1038/s41591-018-0024-8

Ruscetti, M., Morris, J. P. t., Mezzadra, R., Russell, J., Leibold, J., Romesser, P. B., Simon, J., Kulick, A., Ho, Y. J., Fennell, M.*, et al.* (2020, Apr 16). Senescence-Induced Vascular Remodeling Creates Therapeutic Vulnerabilities in Pancreas Cancer. *Cell, 181*(2), 424-441.e421. https://doi.org/10.1016/j.cell.2020.03.008

Sadozai, H., Acharjee, A., Eppenberger-Castori, S., Gloor, B., Gruber, T., Schenk, M., & Karamitopoulou, E. (2021). Distinct Stromal and Immune Features Collectively Contribute to Long-Term Survival in Pancreatic Cancer. *Front Immunol, 12*, 643529. https://doi.org/10.3389/fimmu.2021.643529

Saka, D., Gökalp, M., Piyade, B., Cevik, N. C., Arik Sever, E., Unutmaz, D., Ceyhan, G. O., Demir, I. E., & Asimgil, H. (2020, Aug 14). Mechanisms of T-Cell Exhaustion in Pancreatic Cancer. *Cancers (Basel), 12*(8). https://doi.org/10.3390/cancers12082274

Sallusto, F., & Lanzavecchia, A. (2009, Aug). Heterogeneity of CD4+ memory T cells: functional modules for tailored immunity. *Eur J Immunol, 39*(8), 2076-2082. https://doi.org/10.1002/eji.200939722

Scagliotti, G. V., Gaafar, R., Nowak, A. K., Nakano, T., van Meerbeeck, J., Popat, S., Vogelzang, N. J., Grosso, F., Aboelhassan, R., Jakopovic, M.*, et al.* (2019). Nintedanib in combination with pemetrexed and cisplatin for chemotherapy-naive patients with advanced malignant pleural mesothelioma (LUME-Meso): a double-blind, randomised, placebo-controlled phase 3 trial. *The Lancet Respiratory Medicine, 7*(7), 569-580. https://doi.org/10.1016/S2213-2600(19)30139-0

Scheffzek, K., Ahmadian, M. R., Kabsch, W., Wiesmüller, L., Lautwein, A., Schmitz, F., & Wittinghofer, A. (1997, Jul 18). The Ras-RasGAP complex: structural basis for GTPase activation and its loss in oncogenic Ras mutants. *Science, 277*(5324), 333-338. https://doi.org/10.1126/science.277.5324.333

Schneider, G., Schmidt-Supprian, M., Rad, R., & Saur, D. (2017, Apr). Tissue-specific tumorigenesis: context matters. *Nat Rev Cancer, 17*(4), 239-253. https://doi.org/10.1038/nrc.2017.5

Schreyer, D., Neoptolemos, J. P., Barry, S. T., & Bailey, P. (2021). Deconstructing Pancreatic Cancer Using Next Generation-Omic Technologies-From Discovery to Knowledge-Guided Platforms for Better Patient Management. *Front Cell Dev Biol, 9*, 795735. https://doi.org/10.3389/fcell.2021.795735

Sica, A., Schioppa, T., Mantovani, A., & Allavena, P. (2006, Apr). Tumour-associated macrophages are a distinct M2 polarised population promoting tumour progression: potential targets of anti-cancer therapy. *Eur J Cancer, 42*(6), 717-727. https://doi.org/10.1016/j.ejca.2006.01.003

Siegel, R., Naishadham, D., & Jemal, A. (2012, Jan-Feb). Cancer statistics, 2012. *CA Cancer J Clin, 62*(1), 10-29. https://doi.org/10.3322/caac.20138

Siegel, R. L., Miller, K. D., Fuchs, H. E., & Jemal, A. (2022, Jan). Cancer statistics, 2022. *CA Cancer J Clin, 72*(1), 7-33. https://doi.org/10.3322/caac.21708

Siliņa, K., Soltermann, A., Attar, F. M., Casanova, R., Uckeley, Z. M., Thut, H., Wandres, M., Isajevs, S., Cheng, P., Curioni-Fontecedro, A.*, et al.* (2018, Mar 1). Germinal Centers Determine the Prognostic Relevance of Tertiary Lymphoid Structures and Are Impaired by Corticosteroids in Lung Squamous Cell Carcinoma. *Cancer Res, 78*(5), 1308-1320. https://doi.org/10.1158/0008-5472.Can-17-1987

Simanshu, D. K., Nissley, D. V., & McCormick, F. (2017). RAS Proteins and Their Regulators in Human Disease. *Cell, 170*(1), 17-33. https://doi.org/10.1016/j.cell.2017.06.009

Spear, S., Candido, J. B., McDermott, J. R., Ghirelli, C., Maniati, E., Beers, S. A., Balkwill, F. R., Kocher, H. M., & Capasso, M. (2019). Discrepancies in the Tumor Microenvironment of Spontaneous and Orthotopic Murine Models of Pancreatic Cancer Uncover a New Immunostimulatory Phenotype for B Cells. *Frontiers in Immunology, 10*, 542-542. https://doi.org/10.3389/fimmu.2019.00542

Stromnes, I. M., Hulbert, A., Pierce, R. H., Greenberg, P. D., & Hingorani, S. R. (2017, Nov). T-cell Localization, Activation, and Clonal Expansion in Human Pancreatic Ductal Adenocarcinoma. *Cancer Immunol Res, 5*(11), 978-991. https://doi.org/10.1158/2326-6066.Cir-16-0322

Surveillance Research Program, National Cancer Institute. SEER Stat Fact Sheets: Pancreatic Cancer. Available from: https://seer.cancer.gov/statfacts/html/pancreas.html. (2021).

Sweeney, M., & Foldes, G. (2018, 2018-October-30). It Takes Two: Endothelial-Perivascular Cell Cross-Talk in Vascular Development and Disease [Review]. *Frontiers in Cardiovascular Medicine, 5*. https://doi.org/10.3389/fcvm.2018.00154

Tang, Y., Xu, X., Guo, S., Zhang, C., Tang, Y., Tian, Y., Ni, B., Lu, B., & Wang, H. (2014). An increased abundance of tumor-infiltrating regulatory T cells is correlated with the progression and prognosis of pancreatic ductal adenocarcinoma. *PLOS ONE, 9*(3), e91551. https://doi.org/10.1371/journal.pone.0091551

Tassi, E., Gavazzi, F., Albarello, L., Senyukov, V., Longhi, R., Dellabona, P., Doglioni, C., Braga, M., Di Carlo, V., & Protti, M. P. (2008, Nov 1). Carcinoembryonic antigen-specific but not antiviral CD4+ T cell immunity is impaired in pancreatic carcinoma patients. *J Immunol, 181*(9), 6595-6603. https://doi.org/10.4049/jimmunol.181.9.6595

Tay, R. E., Richardson, E. K., & Toh, H. C. (2021, 2021/02/01). Revisiting the role of CD4+ T cells in cancer immunotherapy—new insights into old paradigms. *Cancer Gene Therapy, 28*(1), 5-17. https://doi.org/10.1038/s41417-020-0183-x

Thorsson, V., Gibbs, D. L., Brown, S. D., Wolf, D., Bortone, D. S., Ou Yang, T. H., Porta-Pardo, E., Gao, G. F., Plaisier, C. L., Eddy, J. A.*, et al.* (2018, Apr 17). The Immune Landscape of Cancer. *Immunity, 48*(4), 812-830.e814. https://doi.org/10.1016/j.immuni.2018.03.023

Tramacere, I., Scotti, L., Jenab, M., Bagnardi, V., Bellocco, R., Rota, M., Corrao, G., Bravi, F., Boffetta, P., & La Vecchia, C. (2010, Mar 15). Alcohol drinking and pancreatic cancer

risk: a meta-analysis of the dose-risk relation. *Int J Cancer, 126*(6), 1474-1486. https://doi.org/10.1002/ijc.24936

Trüb, M., & Zippelius, A. (2021). Tertiary Lymphoid Structures as a Predictive Biomarker of Response to Cancer Immunotherapies. *Front Immunol, 12*, 674565. https://doi.org/10.3389/fimmu.2021.674565

Tseng, W. W., Winer, D., Kenkel, J. A., Choi, O., Shain, A. H., Pollack, J. R., French, R., Lowy, A. M., & Engleman, E. G. (2010, Jul 15). Development of an orthotopic model of invasive pancreatic cancer in an immunocompetent murine host. *Clin Cancer Res, 16*(14), 3684-3695. https://doi.org/10.1158/1078-0432.Ccr-09-2384

Tsou, P., Katayama, H., Ostrin, E. J., & Hanash, S. M. (2016, Oct 1). The Emerging Role of B Cells in Tumor Immunity. *Cancer Res, 76*(19), 5597-5601. https://doi.org/10.1158/0008-5472.Can-16-0431

Tumeh, P. C., Harview, C. L., Yearley, J. H., Shintaku, I. P., Taylor, E. J., Robert, L., Chmielowski, B., Spasic, M., Henry, G., Ciobanu, V.*, et al.* (2014, Nov 27). PD-1 blockade induces responses by inhibiting adaptive immune resistance. *Nature, 515*(7528), 568-571. https://doi.org/10.1038/nature13954

Upadhrasta, S., & Zheng, L. (2019, Sep 16). Strategies in Developing Immunotherapy for Pancreatic Cancer: Recognizing and Correcting Multiple Immune "Defects" in the Tumor Microenvironment. *J Clin Med, 8*(9). https://doi.org/10.3390/jcm8091472

van der Zee, J. A., van Eijck, C. H., Hop, W. C., van Dekken, H., Dicheva, B. M., Seynhaeve, A. L., Koning, G. A., Eggermont, A. M., & ten Hagen, T. L. (2011, Nov). Angiogenesis: a prognostic determinant in pancreatic cancer? *Eur J Cancer, 47*(17), 2576-2584. https://doi.org/10.1016/j.ejca.2011.08.016

Vetter, I. R., & Wittinghofer, A. (2001, Nov 9). The guanine nucleotide-binding switch in three dimensions. *Science, 294*(5545), 1299-1304. https://doi.org/10.1126/science.1062023

Vignali, D. A. A., Collison, L. W., & Workman, C. J. (2008, 2008/07/01). How regulatory T cells work. *Nature Reviews Immunology, 8*(7), 523-532. https://doi.org/10.1038/nri2343

Von Hoff, D. D., Ervin, T., Arena, F. P., Chiorean, E. G., Infante, J., Moore, M., Seay, T., Tjulandin, S. A., Ma, W. W., Saleh, M. N.*, et al.* (2013). Increased Survival in Pancreatic Cancer with nab-Paclitaxel plus Gemcitabine. *New England Journal of Medicine, 369*(18), 1691-1703. https://doi.org/10.1056/NEJMoa1304369

Vonderheide, R. H., & Bayne, L. J. (2013, 2013/04/01/). Inflammatory networks and immune surveillance of pancreatic carcinoma. *Current Opinion in Immunology, 25*(2), 200-205. https://doi.org/https://doi.org/10.1016/j.coi.2013.01.006

Wagner, M., Lopez, M. E., Cahn, M., & Korc, M. (1998, Apr). Suppression of fibroblast growth factor receptor signaling inhibits pancreatic cancer growth in vitro and in vivo. *Gastroenterology, 114*(4), 798-807. https://doi.org/10.1016/s0016-5085(98)70594-3

Wang, W. Q., Liu, L., Xu, H. X., Luo, G. P., Chen, T., Wu, C. T., Xu, Y. F., Xu, J., Liu, C., Zhang, B.*, et al.* (2013). Intratumoral α-SMA enhances the prognostic potency of CD34 associated with maintenance of microvessel integrity in hepatocellular carcinoma and pancreatic cancer. *PLOS ONE, 8*(8), e71189. https://doi.org/10.1371/journal.pone.0071189

Wang, Y. T., Gou, Y. W., Jin, W. W., Xiao, M., & Fang, H. Y. (2016, Mar 12). Association between alcohol intake and the risk of pancreatic cancer: a dose-response meta-analysis of cohort studies. *BMC Cancer, 16*, 212. https://doi.org/10.1186/s12885-016-2241-1

Wartenberg, M., Cibin, S., Zlobec, I., Vassella, E., Eppenberger-Castori, S., Terracciano, L., Eichmann, M. D., Worni, M., Gloor, B., Perren, A.*, et al.* (2018, Sep 15). Integrated Genomic and Immunophenotypic Classification of Pancreatic Cancer Reveals Three Distinct Subtypes with Prognostic/Predictive Significance. *Clin Cancer Res, 24*(18), 4444-4454. https://doi.org/10.1158/1078-0432.Ccr-17-3401

Winograd, R., Byrne, K. T., Evans, R. A., Odorizzi, P. M., Meyer, A. R., Bajor, D. L., Clendenin, C., Stanger, B. Z., Furth, E. E., Wherry, E. J.*, et al.* (2015, Apr). Induction of T-cell Immunity Overcomes Complete Resistance to PD-1 and CTLA-4 Blockade and Improves Survival in Pancreatic Carcinoma. *Cancer Immunol Res, 3*(4), 399-411. https://doi.org/10.1158/2326-6066.Cir-14-0215

Witkiewicz, A. K., McMillan, E. A., Balaji, U., Baek, G., Lin, W. C., Mansour, J., Mollaee, M., Wagner, K. U., Koduru, P., Yopp, A.*, et al.* (2015, Apr 9). Whole-exome sequencing of pancreatic cancer defines genetic diversity and therapeutic targets. *Nat Commun, 6*, 6744. https://doi.org/10.1038/ncomms7744

Wittinghofer, A., & Pai, E. F. (1991, Oct). The structure of Ras protein: a model for a universal molecular switch. *Trends Biochem Sci, 16*(10), 382-387. https://doi.org/10.1016/0968-0004(91)90156-p

Wynn, T. A. (2004, Aug). Fibrotic disease and the T(H)1/T(H)2 paradigm. *Nat Rev Immunol, 4*(8), 583-594. https://doi.org/10.1038/nri1412

Yamazaki, T., & Mukouyama, Y.-s. (2018, 2018-June-27). Tissue Specific Origin, Development, and Pathological Perspectives of Pericytes [Mini Review]. *Frontiers in Cardiovascular Medicine, 5*. https://doi.org/10.3389/fcvm.2018.00078

Zhao, F., Obermann, S., von Wasielewski, R., Haile, L., Manns, M. P., Korangy, F., & Greten, T. F. (2009, Sep). Increase in frequency of myeloid-derived suppressor cells in mice with spontaneous pancreatic carcinoma. *Immunology, 128*(1), 141-149. https://doi.org/10.1111/j.1365-2567.2009.03105.x

Acknowledgments

First and foremost, I would like to express my deepest gratitude to my supervisor Prof. Dr. Dieter Saur for offering me the opportunity to complete my doctorate in his research group. I would like to thank him for supporting my research and ambition to pursue a career as a clinician scientist.

I would also like to express my sincere gratitude to Chiara Falcomatà for providing me guidance every step of the way. Her scientific curiosity and enthusiasm have motivated and inspired me greatly throughout the years. She has been a constant role model for me, and I am truly grateful to have learned from her.

My thanks also go to all other members of our lab, especially Stefanie Bärthel and Tânia Custodio Santos, for always offering me a helping hand.

Finally, I would like to thank my parents, my brothers and Jonas for their love and unconditional support.